

NO-A187 399

REGIONAL WAVE ATTENUATION AND SEISMIC MOMENT FROM THE
INVERSION OF NORESS (U) SCIENCE APPLICATIONS
INTERNATIONAL CORP SAN DIEGO CA T J SERENO ET AL

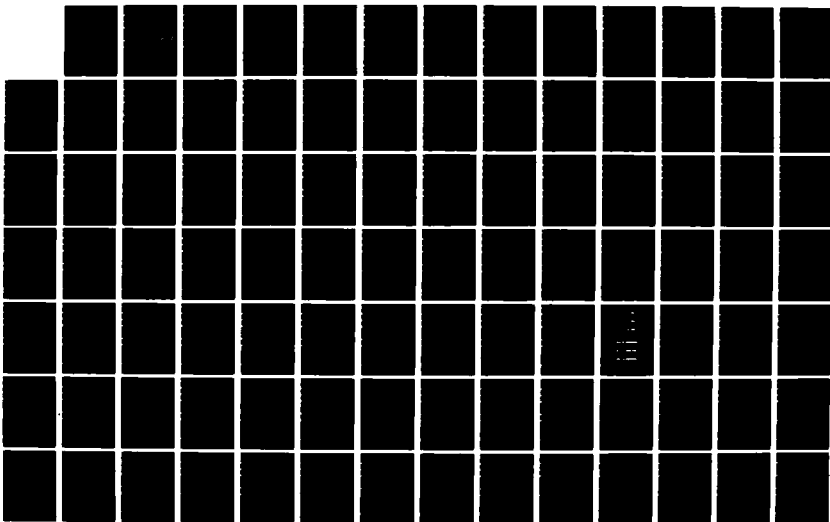
1/2

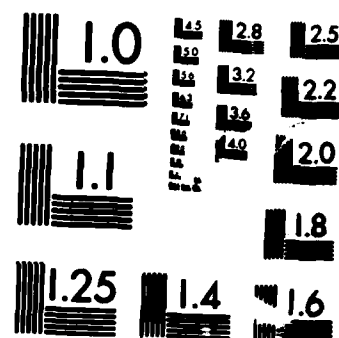
UNCLASSIFIED

31 JUL 87 SAIC-87/1736 AFGL-TR-87-0237

F/G 8/11

NL





MICROCOPY RESOLUTION TEST CHART
NATIONAL BUREAU OF STANDARDS-1963-A

AD-A187 399

AFGL-TR-87-0237

**REGIONAL WAVE ATTENUATION AND SEISMIC MOMENT
FROM THE INVERSION OF NORESS SPECTRA**

Thomas J. Sereno, Jr.
Steven R. Bratt
Thomas C. Bache

Science Applications International Corp.
10210 Campus Point Drive
San Diego, CA 92121

DTIC
ELECTE
NOV 25 1987
S D

31 July 1987

Semiannual Report No. 2

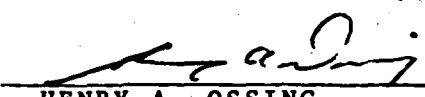
Approved for public release; distribution unlimited

AIR FORCE GEOPHYSICS LABORATORY
AIR FORCE SYSTEMS COMMAND
UNITED STATES AIR FORCE
HANSCOM AIR FORCE BASE, MASSACHUSETTS 01731

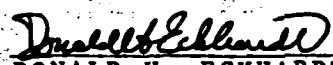
87 11 16 061

"This technical report has been reviewed and is approved for publication"


JAMES F. LEWKOWICZ
Contract Manager


HENRY A. OSSING
Branch Chief

FOR THE COMMANDER


DONALD H. ECKHARDT
Division Director

This report has been reviewed by the ESD Public Affairs Office (PA) and is releasable to the National Technical Information Service (NTIS).

Qualified requestors may obtain additional copies from the Defense Technical Information Center. All others should apply to the National Technical Information Service.

If your address has changed, or if you wish to be removed from the mailing list, or if the addressee is no longer employed by your organization, please notify AFGL/DAA, Hanscom AFB, MA 01731. This will assist us in maintaining a current mailing list.

Do not return copies of this report unless contractual obligations or notices on a specific document requires that it be returned.

AL 1187 399

REPORT DOCUMENTATION PAGE

1a. REPORT SECURITY CLASSIFICATION Unclassified			1b. RESTRICTIVE MARKINGS		
2a. SECURITY CLASSIFICATION AUTHORITY			3. DISTRIBUTION/AVAILABILITY OF REPORT Approved for public release; distribution unlimited		
2b. DECLASSIFICATION/DOWNGRADING SCHEDULE					
4. PERFORMING ORGANIZATION REPORT NUMBER(S) SAIC 87/1736			5. MONITORING ORGANIZATION REPORT NUMBER(S) AFGL-TR-87-0237		
6a. NAME OF PERFORMING ORGANIZATION Science Applications International Corporation		6b. OFFICE SYMBOL (if applicable)	7a. NAME OF MONITORING ORGANIZATION Air Force Geophysics Laboratory (LWH)		
6c. ADDRESS (City, State, and ZIP Code) 10210 Campus Point Drive San Diego, CA 92121			7b. ADDRESS (City, State, and ZIP Code) Hanscom Air Force Base, MA 01731		
8a. NAME OF FUNDING/SPONSORING ORGANIZATION DARPA		8b. OFFICE SYMBOL (if applicable) GSD	9. PROCUREMENT INSTRUMENT IDENTIFICATION NUMBER F19628-86-C-0051		
8c. ADDRESS (City, State, and ZIP Code) 1400 Wilson Blvd. Arlington, VA 22209			10. SOURCE OF FUNDING NUMBERS		
			PROGRAM ELEMENT NO. 62714E	PROJECT NO. 6A10	TASK NO. DA
					WORK UNIT ACCESSION NO. BB
11. TITLE (Include Security Classification) Regional Wave Attenuation and Seismic Moment from the Inversion of NORESS Spectra					
12. PERSONAL AUTHOR(S) Thomas J. Sereno, Jr., Steven R. Bratt and Thomas C. Bache					
13a. TYPE OF REPORT Semi-Annual #2		13b. TIME COVERED FROM 9/1/86 TO 2/28/87		14. DATE OF REPORT (Year, Month, Day) 1987 July 31	
15. PAGE COUNT 124					
16. SUPPLEMENTARY NOTATION					
17. COSATI CODES			18. SUBJECT TERMS (Continue on reverse if necessary and identify by block number)		
FIELD	GROUP	SUB-GROUP	Regional Seismology, Generalized Inversion, Attenuation, Seismic Moment, NORESS Array		
19. ABSTRACT (Continue on reverse if necessary and identify by block number)					
<p>Frequency-dependent regional wave attenuation along continental paths to the NORESS array in Norway is investigated. Regional L_g and P_n spectra from 190 events, at distances between 200 and 1300 km, have been inverted for seismic moment and apparent attenuation. Our method uses both the spectral and spatial decay of observed signal amplitudes to separate source and path contributions. Based on adequate signal/noise, the L_g spectra were inverted between 1 and 7 Hz and the P_n spectra between 1 and 15 Hz. The data are parameterized by an ω^2 source spectrum with cube-root corner frequency scaling and an assumed geometric spreading function. Most events considered have local magnitudes less than 3.0, so the corner</p>					
20. DISTRIBUTION/AVAILABILITY OF ABSTRACT <input type="checkbox"/> UNCLASSIFIED/UNLIMITED <input checked="" type="checkbox"/> SAME AS RPT <input type="checkbox"/> DTIC USERS			21. ABSTRACT SECURITY CLASSIFICATION Unclassified		
22a. NAME OF RESPONSIBLE INDIVIDUAL James F. Lewkowicz			22b. TELEPHONE (Include Area Code) (617) 377-3028		22c. OFFICE SYMBOL AFGL/LWH

frequencies are near or beyond the upper limit of the bandwidth inverted, Our Q results, particularly for Lg , are therefore not very sensitive to the details of our source parameterization. The spectra are inverted for source moment, a constant relating corner frequency and moment, and two parameters describing a power-law frequency dependence of Q . For fixed source and spreading assumptions, the inversion defines clear trade-offs among model parameters. To resolve these trade-offs, we add the constraint that the separately derived source parameters for Lg and Pn be consistent. Our estimates for the apparent attenuation are $Q_{Lg}(f) = 350f^{0.41}$ and $Q_{Pn}(f) = 300f^{0.49}$. The inversion results for seismic moment as a function of local magnitude are generally consistent with near-field studies. In that magnitude does not enter the inversion, this result lends considerable support to the derived Q models. The final result is an accurate parameterization of observed amplitude spectra of regional events recorded at NORESS that can be used to address a number of seismological problems related to wave propagation in the region and to the treaty monitoring capabilities of small regional networks.

Accession For	
NTIS CRA&I	<input checked="" type="checkbox"/>
DTIC TAB	<input type="checkbox"/>
Unannounced	<input type="checkbox"/>
Justification	
By	
Distribution	
Availability Codes	
Dist	Avail and/or Special
A-1	



Table of Contents

1. INTRODUCTION	1
1.1 Objectives	1
1.2 Outline of the report	2
2. REGIONAL Pn AND Lg PHASES	4
3. GENERALIZED INVERSION	8
3.1 Description of the method	8
3.2 Assumptions	14
3.2.1 Source spectra	16
3.2.2 Geometric spreading	16
3.2.3 $Q(f)$ parameterization	17
3.2.4 Radiation pattern	17
3.2.5 Interference phenomena	17
4. DATA BASE	19
4.1 Signal processing	19
4.2 Data	21
5. ATTENUATION AND SEISMIC MOMENT ESTIMATES	33
5.1 Regional Lg spectra	33
5.2 Regional Pn spectra	34
5.3 Pn/Lg consistency	37
5.4 Seismic moments	40
5.5 Corner frequency	42
6. ERROR ANALYSIS	46
6.1 Formal inversion errors	47
6.2 Parameter trade-off	49
6.3 Result dependence on parameterization	54
6.3.1 Source parameterization	54
6.3.2 Geometric spreading	55
6.4 Systematic variations in source moment versus Lg amplitude	57
6.5 Anomalous events	57
7. SIMULATION OF REGIONAL Pn AND Lg SPECTRA	62

TABLE OF CONTENTS

8. CONCLUSIONS	66
ACKNOWLEDGEMENTS	69
REFERENCES	71
APPENDIX A. PROCESSED EVENTS NOT INCLUDED IN THE INVER- SION	75
APPENDIX B. INVERSION RESULTS	81

1. INTRODUCTION

This report presents the results of a detailed analysis of regional wave attenuation along continental paths to the NORESS array in Norway. Our data consist of stable, array-averaged spectra from 190 regional events recorded by the high-quality NORESS digital instruments. The logarithm of the amplitude spectra from events of varying magnitude and epicentral distance are inverted simultaneously for both the source moment and the apparent attenuation. The result is a simple parameterization of the observed amplitude spectra that can be used to address a number of seismological problems related to wave propagation in the region and to the treaty monitoring capabilities of small regional networks.

1.1 Objectives

The overall objective is to systematically characterize the spectra of regional phases recorded at NORESS. The emphasis is on the separation of source and path contributions to observed signal amplitudes. To accomplish this, we have developed a least-squares, generalized inversion that simultaneously estimates source strength and $Q(f)$. The data are parameterized by an ω^2 source spectrum with cube-root corner frequency scaling and an assumed geometric spreading function. The method utilizes both the spectral and spatial decay of observed signal amplitudes to separate source and path contributions. The result is accurate attenuation curves for the regional phases analyzed. Important applications of these curves include:

- *Simulation for hypothetical sources.* Once the path contribution has been isolated, frequency-dependent signal amplitudes resulting from a known, theoretical source can be predicted. These predicted amplitude spectra can be used in the normalization of network capability simulations.
- *Extrapolation of detection capability to other regions.* Since we have an estimate for the attenuation for paths to NORESS, we can extrapolate the empirical NORESS detection capability to other areas where the attenuation has been estimated.
- *Regional event identification.* Identification of regional events requires that we distinguish relatively small differences in source spectra. This requires an accurate, specific knowledge of path effects between source and array locations.

- *Yield estimation.* If regional phases recorded at NORESS are to be used for yield estimation, their attenuation functions must be accurately determined.

While numerous studies of *Lg* attenuation have been conducted, comparatively few analyses for regional *P* waves exist. However, a successful parameterization of regional *P* wave attenuation, particularly at high frequency, has important implications for *Q* in the lithosphere and for many practical issues in treaty monitoring seismology. Analysis of *Pn* is difficult because it samples a much smaller fraction of the focal sphere than *Lg*, so its amplitude is more sensitive to source radiation pattern, focussing and defocussing, and scattering.

Our inversion includes *Pn* and *Lg* spectra from 190 regional events recorded at NORESS at ranges between 200 and 1300 km. The frequency band for the *Lg* inversion is 1 to 7 Hz. This is because the *Lg* signal/noise is less than one above 7 or 8 Hz for most of the events beyond 800 km range. Also, at shorter distances the *Lg* spectra are probably contaminated by *Sn* coda at high frequency. The *Pn* spectra were inverted between 1 and 15 Hz (the upper limit of adequate signal/noise for the events in the data base). We examined the dependence of our *Q* estimation on azimuth, assumptions of source spectral shape, and our geometric spreading assumptions. We find that the data are adequately represented by a simple ω^2 source and a single, frequency-dependent, *Q* model.

1.2 Outline of the report

This report is divided into 8 sections, including this introduction. Section 2 is a brief description of regional *Pn* and *Lg* phases and reviews previous studies of their attenuation. Section 3 describes the generalized inversion method, including all the simplifying assumptions used in the inversion. The dependence of our results on these assumptions is the subject of Section 6.3. Section 4 and Appendix A describe the data base and the signal processing procedures.

The primary results of the study are given in Section 5. *Lg* attenuation is discussed in Section 5.1 and *Pn* attenuation in Section 5.2. Because the *Pn* and *Lg* inversions are done separately, an important check is the consistency of the inverted source parameters from the two phases (Section 5.3). In Section 5.4 we relate the moments from the inversion to local magnitude, which is important for predicting range-dependent spectra for a given magnitude. In Section 5.5 we discuss the relation between corner frequency from the inversion and source size. Most of the events studied have $M_L < 3.0$ and thus have high corner frequencies. Therefore, the data do not clearly resolve source corner frequency, but we note that our results are consistent with

those from similar studies. Appendix B tabulates the inversion parameters for each event studied and includes plots comparing the theoretical spectra and observed spectra.

Error analysis is the subject of Section 6. Both formal inversion errors and estimated parameter accuracy are discussed. Section 6.3 is devoted to analyzing the dependence of the results on our parameterization. In particular, the source spectrum and geometric spreading assumptions are varied, and the resulting change in model parameters is monitored. Section 6.4 discusses observed systematic variations in source moment versus Lg amplitude for different mines. Section 6.5 illustrates some examples of spectra that are not well-modeled by the inversion results. Fortunately, these constitute only a small fraction of the events investigated.

Section 7 demonstrates one of the most important applications of this work, the simulation of the spectra from hypothetical events. In particular, predicted range-dependent Pn and Lg spectra for fixed magnitude are presented. Finally, Section 8 presents our main conclusions and summarizes the results of this study.

2. REGIONAL P_n AND L_g PHASES

Regional seismograms recorded along continental paths are characterized by the appearance of one or more of the phases P_n , P_g , S_n , and L_g . P_n and S_n predominantly sample the uppermost mantle while P_g and L_g are crustal phases. In this study we focus our attention on P_n and L_g . L_g is often the largest amplitude signal for stable continental paths. It has been modeled successfully as a sum of higher mode surface waves with constant group velocity near 3.5 km/s and energy density confined to the crust (Knopoff, et al., 1973; Panza and Calcagnile, 1975; Bache, et al., 1981). Regional P_n phases are the first arrivals beyond about 200 km and propagate in the upper mantle with group velocities typically between 7.5 and 8.0 km/s. However, at distances less than 300 km, P_g arrives within 5s of P_n . The P_n amplitude is generally less than that of L_g (by a factor of 3 or more in the distance range 100-500 km; Mykeltveit and Ringdal, 1979), due partly to geometric spreading differences, and it has a higher dominant frequency than L_g .

Numerous studies of L_g attenuation have been conducted (e.g., Cheng and Mitchell, 1981; Herrmann and Kijko, 1983; Singh and Herrmann, 1983; Peseckis and Pomeroy, 1984; Campillo, et al., 1985; Hasegawa, 1985; Chun, et al., 1987; Gupta and McLaughlin, 1987; Shin and Herrmann, 1987). Table 2.1 and Figure 2.1 summarize reported L_g attenuation estimates for various regions. Entries 1-4 of Table 2.1 are attenuation estimates for paths in the western United States. With the exception of Chavez and Priestley (1986), these studies are band limited to relatively low frequencies. Entries 5-10 are estimates for paths across eastern North America. An obvious conclusion is that the tectonically active western United States is characterized by a lower Q and stronger frequency dependence than the stable eastern North American shield.

Very few regional P wave attenuation studies have been conducted. This is probably because P_n samples a much smaller fraction of the focal sphere than L_g , making its amplitude more sensitive to source radiation pattern, focussing and defocussing, and scattering. Several recent studies of both P and S wave attenuation have uncovered the peculiar observation that Q_β/Q_α reaches values greater than or equal to one at high frequency (Clements, 1982; Taylor, et al., 1986; Butler, et al., 1987; Chavez and Priestley, 1987; Sereno and Orcutt, 1987). In a study of regional crustal phases, Chavez and Priestley (1987) estimated attenuation between 1 and 10 Hz for paths across the Great Basin and found that $P_g Q$ was less than $L_g Q$. We have examined both P_n and L_g attenuation in this study, but note that the two phases sample different depths. Both the scattering and intrinsic absorption contributions to the apparent attenuation

Table 2.1. Reported $Q_{Lg}(f)$ estimates.

	Region	Frequency (Hz)	$Q_{Lg}(f)$		Reference
			Q_0	η	
(1)	Western United States	0.5-3.5	140-200	0.4-0.6	Singh and Herrmann (1983)
(2)	Western United States (NTS Explosions)	1.0-2.0	200-300	0.2-0.4	Pesceckis and Pomeroy (1984)
(3)	Western United States (NTS Explosions)	1.0-2.0	139	0.6	Nuttli (1986)
(4)	Western United States (Great Basin)	0.25-12.5	206	0.68	Chavez and Priestley (1986)
(5)	Eastern United States	0.5-3.5	1000	0.3-0.4	Singh and Herrmann (1983)
(6)	Eastern North America	1.0-15.0	900	0.2	Hasegawa (1985)
(7)	Eastern United States	--	1000	0.35	Gonz and Dean (1986)
(8)	Eastern Canada	0.6-10.0	1100	0.19	Chun, et al. (1987)
(9)	Eastern United States	0.5-7.0	800	0.32	Gupta and McLaughlin (1987)
(10)	Eastern North America	0.5-15.0	500-550	0.65	Shin and Herrmann (1987)
(11)	Central France	0.5-10.0	290	0.52	Campillo, et al. (1985)
(12)	Southern Africa	--	600	0.4	Mitchell, et al. (1987)

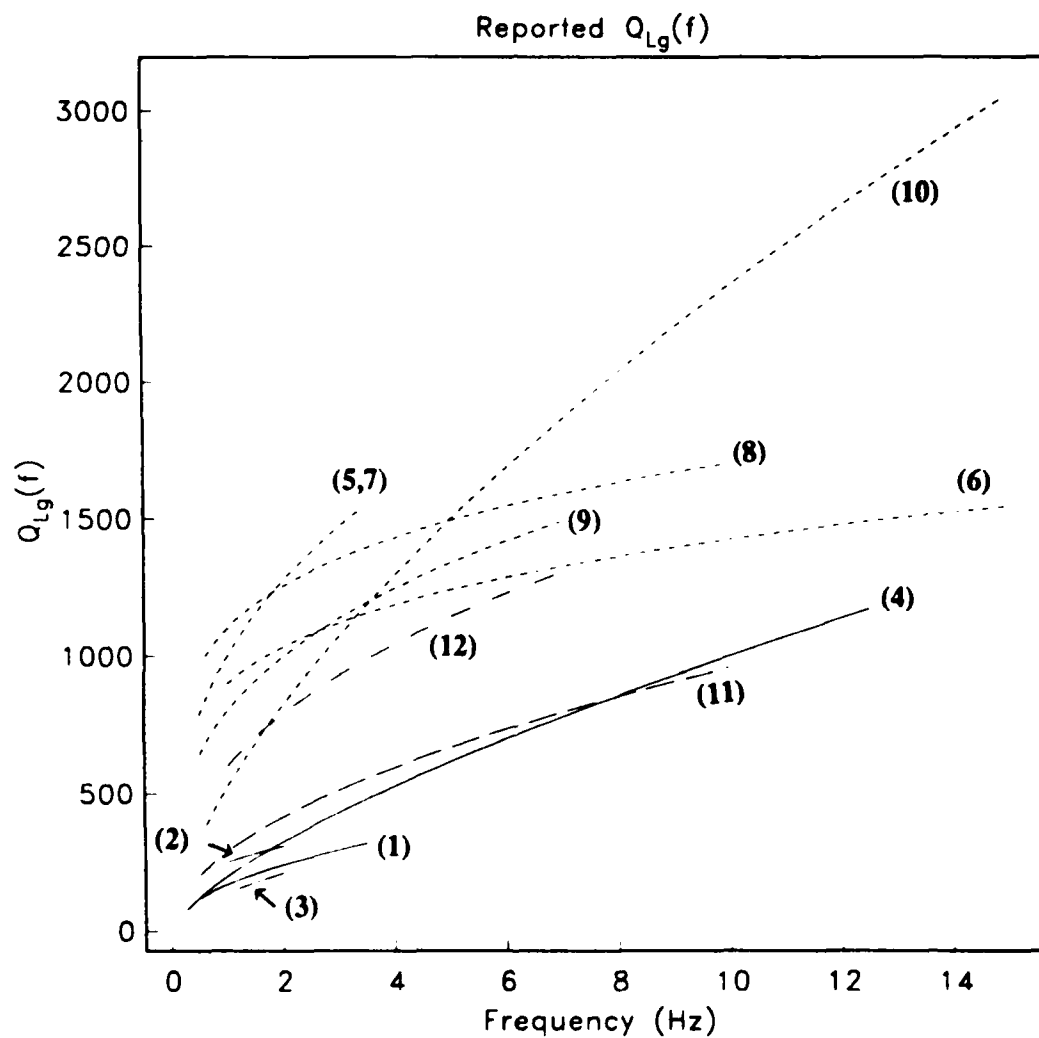


Figure 2.1. Reported $Q_{Lg}(f)$ curves for various geographic regions. The curves are identified by the numbered entries listed in Table 2.1.

are expected to be different for the two phases. Therefore, comparison of the Q obtained does not provide much information about lithosphere rheology. Numerical modeling of Lg suggests that its observed attenuation is an effective measure of the average absorption of shear waves in the crust (Campillo, et al., 1985). Factors other than intrinsic absorption play an important role in the attenuation of Pn . Therefore, it is inappropriate to associate observed Pn attenuation with intrinsic absorption at a particular depth in the upper mantle. Our emphasis is not, however, on the physical mechanisms of attenuation, but rather on the development of empirical functions to be used to predict frequency-dependent amplitudes.

Regional Lg phases have also been used to estimate source parameters including corner frequency and seismic moment (Street, et al., 1975; Dwyer, et al., 1983; Hasegawa, 1983; Shin and Herrmann, 1987). These results are, in general, consistent with near-field source studies, with the possible exception that corner frequencies obtained from Lg tend to be lower than those estimated at short range (Mueller and Cranswick, 1985).

Observed Lg to P amplitude ratios are complicated functions of source depth, near-surface velocity, and lateral structural variations. Nevertheless, moderate success has been attained in using Lg/Pn and Lg/Pg ratios as regional earthquake-explosion discriminants (for review, see Pomeroy, et al., 1982). For example, in a comparison of Lg/Pn ratios for an NTS explosion to a co-located earthquake at a range of 450 km, Willis (1963) found that the earthquake source resulted in an Lg/Pn ratio 5 times that of the explosion. Pomeroy (1977) found a similar result comparing 12 earthquakes to the SALMON nuclear explosion detonated in Mississippi. More recently, Murphy and Bennett (1982) compared NTS explosions to nearby earthquakes and found that observed Lg amplitudes were typically greater for earthquakes than for explosions with comparable P wave amplitudes. However, they found that the simple time domain amplitude ratios did not provide consistent separation between the two populations. Explosions generate Lg energy primarily through P - SV mode conversions and scattering. In addition, earthquakes directly produce shear wave energy that can contribute to Lg . Therefore, for a given focal depth earthquakes are expected to be more efficient in Lg excitation than explosions. Bennett, et al. (1987) compared the relative excitation of synthetic Pg and Lg phases for earthquakes and explosions as a function of source depth. They found that the Lg/Pg ratio was only slightly higher for near-surface earthquakes than for near-surface explosions, but was a factor of 3 higher at a depth of 1 km.

3. GENERALIZED INVERSION

The key to estimating regional wave attenuation is separating source and path effects. For one event recorded at one station, there is a direct trade-off between source and path contributions to the observed signal spectrum. We have many events recorded at one station and study the attenuation as a function of distance and frequency. Our analysis assumes that all observed spectra can be fit by a single frequency-dependent Q model and that all source spectra scale simply with event size. In this way we use the range-independence of the source function to separate the different contributions to the seismic spectrum.

Our generalized inversion procedure simultaneously estimates seismic moment and $Q(f)$. Adopting standard methods for solving non-linear inverse problems, we linearize the system of equations governing the relationship between the data and model parameters. We assume a starting model, compute theoretical data, subtract it from the observed data, and solve iteratively for the model perturbations that minimize the data residual in the least-squares sense. In practice, we have found it necessary to include damping to stabilize the solution. That is, we minimize a weighted sum of the data residuals and the model perturbation norm.

3.1 Description of the method

We parameterize the instrument-corrected amplitude spectrum of a seismic signal as

$$A(f,r) = S(f) G(r,r_0) \exp \left[\frac{-\pi f t}{Q(f)} \right], \quad (3.1.1)$$

where $A(f,r)$ is the observed displacement spectrum at range r and frequency f ; $S(f)$ is the source spectrum; $G(r,r_0)$ is geometric spreading, and the last term is the *effective attenuation* for travel time, t . Note that the *effective attenuation* includes contributions from both anelasticity and scattering.

We assume the geometric spreading function, so the computed attenuation functions and seismic moments are relative to the assumed spreading rate. Following Herrmann and Kijko (1983), we express the spreading function as

$$\begin{aligned} G(r,r_0) &= (1/r), & \text{for } r \leq r_0 \\ &= r_0^{-1} (r_0/r)^m, & \text{for } r \geq r_0 \end{aligned} \quad (3.1.2)$$

where r_0 is a transition distance from spherical spreading to spreading rate m . By comparing the long period amplitude spectrum of Lg to moments calculated from long period surface waves, Street, et al. (1975) empirically determined $r_0 \approx 100$ km, or roughly twice the crustal thickness. Measuring the decay rate of synthetic Lg phases computed for an elastic medium, Herrmann and Kijko (1983) verified that Lg frequency domain spreading was accurately described as cylindrical ($m=1/2$) and substantiated the empirical result of Street, et al. (1975) for r_0 . Less work has been done on the spreading rate of Pn . Because its energy density is more localized about a single ray path, Pn geometric spreading is more sensitive to velocity gradients in the upper mantle. Numerical studies of Pn indicate, for typical upper mantle structures, that its spreading rate lies between r^{-1} and r^{-2} (Langston, 1982; Wallace, personal communication). This approximately corresponds to the range between simple turning ray and canonical headwave Pn ray path interpretations. In this report, we investigate spreading rates between these bounding values as approximations to the true spreading rate of Pn .

The inversion also requires a source spectral shape parameterization. We assume an ω^2 spectrum with corner frequency inversely proportional to the cube-root of the long period source level. That is, we assume the seismic source function can be expressed as

$$S(f) = S_0 s(f) \quad (3.1.3)$$

where S_0 is the long period source level and $s(f)$ is a known function which depends on S_0 and describes the source spectral shape. We have investigated two functional forms for the ω^2 source; a simplified Mueller-Murphy (1971) explosion source model and a Brune (1970, 1971) earthquake source model. The explosion source has the form

$$s(f) = \frac{f_c^2}{(f_c^4 + (1-2\beta)f_c^2 f^2 + \beta^2 f^4)^{1/2}} \quad (3.1.4)$$

where β controls the amount of overshoot and f_c is the corner frequency. The earthquake source model has frequency dependence

$$s(f) = \frac{f_c^2}{(f + f_c)^2} \quad (3.1.5)$$

In both cases we assume that corner frequency scales with the cube-root of the long period level. That is,

$$f_c = c S_0^{-1/3} \quad (3.1.6)$$

and c is a parameter of the inversion. In Figure 3.1 we plot a family of curves for each source model.

The source parameters estimated by the inversion are S_0 for each event and a single value of c relating corner frequency to long period source level. For near-surface explosions, the relationship between S_0 and seismic moment (M_0) for Pn is (Stevens and Day, 1985)

$$S_0^{\text{exp}}(Pn) = \frac{M_0^{\text{exp}}}{4\pi\rho_s\alpha_s^3} \quad (3.1.7)$$

All of the explosions in our data set are near-surface mining explosions, characterized by the near-surface density (ρ_s) and compressional velocity (α_s). For earthquakes the expression is complicated by the depth of the event and the radiation pattern. From Stevens and Day (1985), the expression for S_0 is

$$S_0^{\text{eq}}(Pn) = \frac{M_0^{\text{eq}} R_{\theta\theta}^P}{4\pi(\rho_c\rho_s\alpha_c^5\alpha_s)^{1/2}} \quad (3.1.8)$$

where ρ_c and α_c are crustal density and compressional velocity at the source depth and $R_{\theta\theta}^P$ is the P wave source radiation pattern. Since our observations are from a single station, and the focal mechanisms for the small earthquakes in our data set are unknown, we do not know $R_{\theta\theta}^P$ and are therefore unable to estimate seismic moment from $S_0^{\text{eq}}(Pn)$. However, using the empirical result of Street, et al. (1975), we can estimate the earthquake moments from Lg spectra using

$$S_0^{\text{eq}}(Lg) = \frac{M_0^{\text{eq}}}{4\pi\rho_c\beta_c^3}, \quad (3.1.9)$$

where ρ_c and β_c are the average crustal density and shear wave velocity, respectively.

The amount of Lg energy excited by an explosion is depth dependent and complicated by near-source wave conversions. Also, a cylindrically symmetric surface explosion generates relatively more shear wave energy than one that is buried. Thus, a simple expression relating the seismic moment of an explosion to the long period Lg spectrum does not exist. In general, earthquakes generate more shear wave energy than explosions, so we express the long period

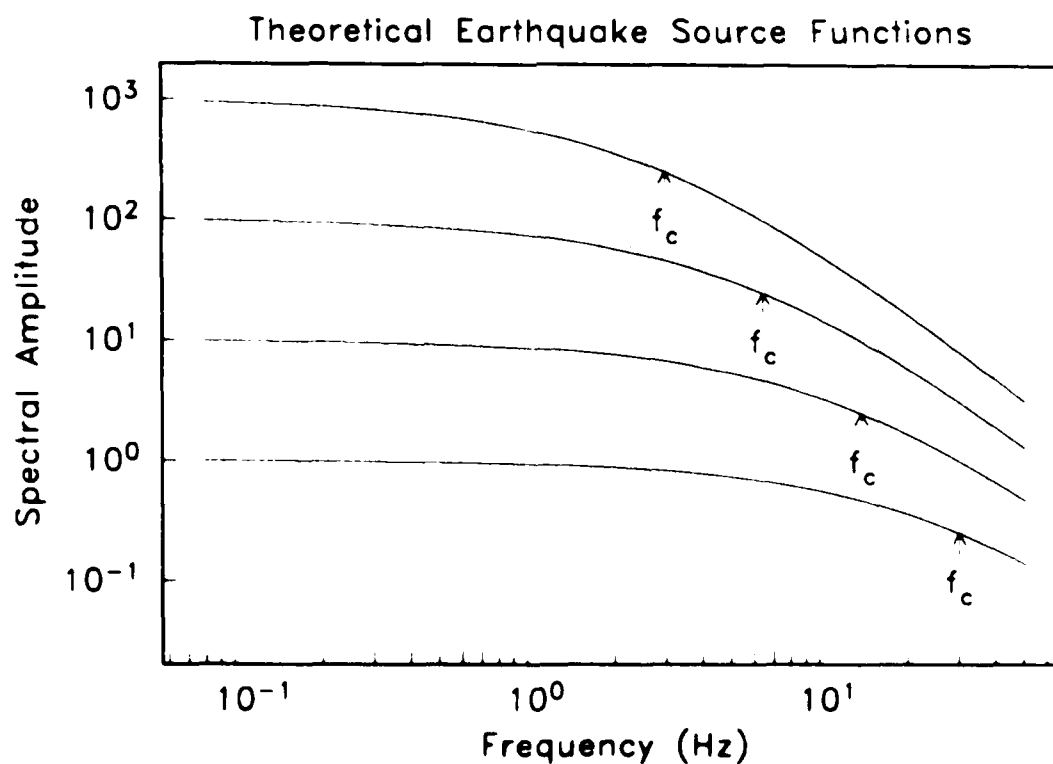
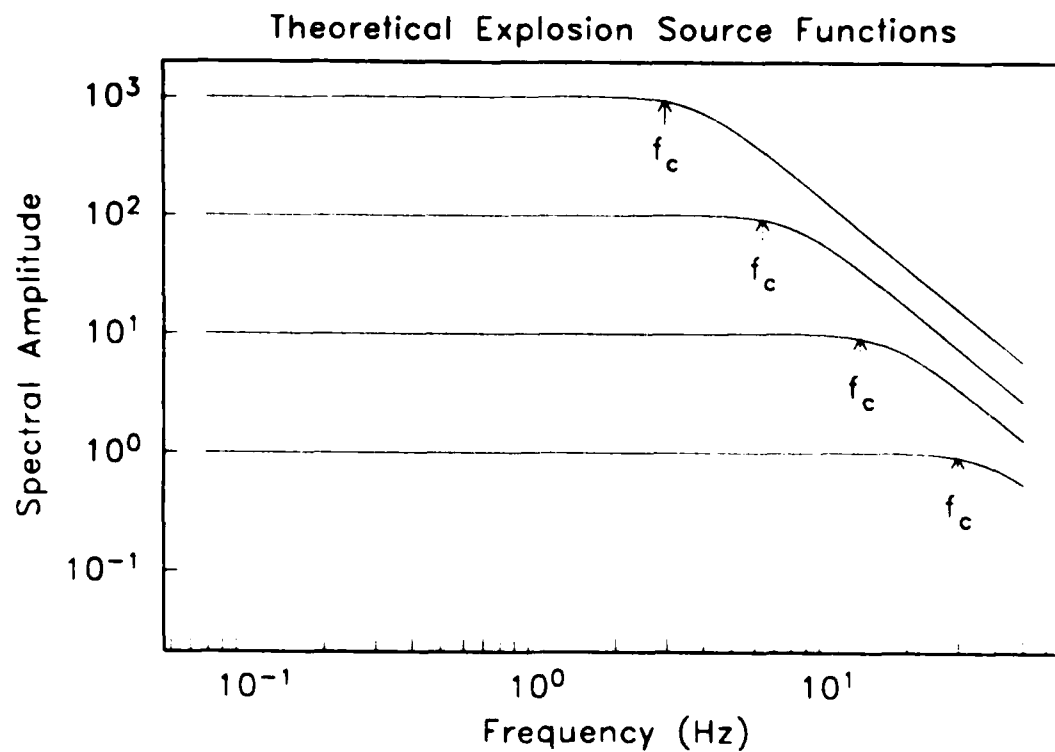


Figure 3.1. Theoretical source functions. (a) Mueller-Murphy (1971) explosion source spectra (3.1.4) with $\beta = 0.6$ and (b) Brune (1970, 1971) earthquake source spectra (3.1.5). The corner frequency, f_c , scales inversely with the cube-root of the long period level (3.1.6).

Lg source level for an explosion as an unknown fraction of the long period level for an earthquake of equal moment and equal depth. That is,

$$S_0^{xp}(Lg) = \kappa S_0^{eq}(Lg) \quad (3.1.10)$$

where κ is an unknown constant, presumably less than one. We will estimate this constant by using the explosion moments obtained from Pn in the above expression for $S_0^{xp}(Lg)$.

The inversion requires a parameterization of apparent attenuation. No attempt is made to separate the effects of scattering from intrinsic absorption. We simply model the spectral decay in terms of a power-law frequency dependence of Q ,

$$Q(f) = Q_0 f^\eta \quad (3.1.11)$$

with Q_0 and η parameters of the inversion. Using (3.1.1) and (3.1.11) we compute the function $d(f,r)$ from

$$d(f,r) = \text{Log } A(f,r) - \text{Log } G(r,r_0) = \text{Log } S(f) - 0.01\alpha_0 f^{(1-\eta)} r \quad (3.1.12)$$

where

$$\alpha_0 = \frac{100 \pi \text{Log } e}{Q_0} \quad (3.1.13)$$

The $d(f,r)$ is the observed data corrected for the assumed geometric spreading function and is the input data for the inversion. The factor of 100 in α_0 was introduced to avoid matrix ill-conditioning. A $d_0(f,r)$ can be computed from an assumed starting model. This is subtracted from the observed data $d(f,r)$, giving a data residual which can be expressed in matrix form as

$$\Delta d = A \Delta m \quad (3.1.14)$$

In (3.1.14), Δd is the data residual vector, A is the matrix of partial derivatives of the data with respect to the model parameters, and Δm is the model perturbation vector. Explicitly

$$\Delta d^T = [\Delta d(f_1, r_1), \Delta d(f_2, r_1), \dots, \Delta d(f_{nf}, r_1), \Delta d(f_1, r_2), \Delta d(f_2, r_2), \dots, \Delta d(f_{nf}, r_{nev})] \quad (3.1.15)$$

where nf is the number of frequencies and nev is the number of events. The total number of data is $nd = nf \times nev$ and the number of parameters is $np = nev + 3$. The $(np \times 1)$ model perturbation vector is

$$\Delta \mathbf{m}^T = [\Delta(\text{Log} S_0^1), \Delta(\text{Log} S_0^2), \dots, \Delta(\text{Log} S_0^{nev}), \Delta c, \Delta \alpha_0, \Delta \eta] \quad (3.1.16)$$

where S_0^i is the long period source level of the i^{th} event. The first nev columns of the $(nd \times np)$ matrix \mathbf{A} are the partial derivatives of the data with respect to $\text{Log} S_0$ for each event. The last 3 columns of \mathbf{A} are the partials with respect to the parameters c , α_0 , and η . That is,

$$\mathbf{A} = \begin{bmatrix} \frac{\partial d_1}{\partial \text{Log} S_0^1} & \frac{\partial d_1}{\partial \text{Log} S_0^2} & \dots & \frac{\partial d_1}{\partial \text{Log} S_0^{nev}} & \frac{\partial d_1}{\partial c} & \frac{\partial d_1}{\partial \alpha_0} & \frac{\partial d_1}{\partial \eta} \\ \vdots & \vdots & \ddots & \vdots & \vdots & \vdots & \vdots \\ \frac{\partial d_{nd}}{\partial \text{Log} S_0^1} & \frac{\partial d_{nd}}{\partial \text{Log} S_0^2} & \dots & \frac{\partial d_{nd}}{\partial \text{Log} S_0^{nev}} & \frac{\partial d_{nd}}{\partial c} & \frac{\partial d_{nd}}{\partial \alpha_0} & \frac{\partial d_{nd}}{\partial \eta} \end{bmatrix} \quad (3.1.17)$$

Each of the first nev columns of \mathbf{A} has only nf non-zero elements. That is, spectra from the i^{th} event have no dependence on the long period level of the j^{th} source, unless $i = j$. That part of the matrix \mathbf{A} is block diagonal.

The partials with respect to path parameters are

$$\frac{\partial d}{\partial \alpha_0} = -0.01 f^{(1-\eta)} t, \quad (3.1.18)$$

$$\frac{\partial d}{\partial \eta} = -0.01 \alpha_0 t (\ln f) f^{(1-\eta)}. \quad (3.1.19)$$

The absolute value of $\partial d / \partial \alpha_0$ typically ranges between 0.6 and 8 for Lg and between 0.3 and 5 for Pn . The partial, $\partial d / \partial \eta$, varies between 0 and 7 for Lg and 0 and 6 for Pn .

For the Mueller-Murphy (1971) source model, the partials with respect to source terms are

$$\frac{\partial d}{\partial \text{Log} S_0} = 1 - \frac{S_0}{3} \left[\frac{2\beta^2 f^4 S_0^{1/3} + (1-2\beta)c^2 f^2 S_0^{-1/3}}{c^4 + (1-2\beta)c^2 f^2 S_0^{2/3} + \beta^2 f^4 S_0^{4/3}} \right], \quad (3.1.20)$$

$$\frac{\partial d}{\partial c} = \frac{2 \text{Log } e}{c} \left[1 - \frac{c}{2} \left\{ \frac{2c^3 + (1-2\beta)cf^2S_0^{2/3}}{c^4 + (1-2\beta)c^2f^2S_0^{2/3} + \beta^2f^4S_0^{4/3}} \right\} \right] \quad (3.1.21)$$

Similarly, for the Brune (1970, 1971) source model

$$\frac{\partial d}{\partial \text{Log } S_0} = 1 - \frac{2 S_0^{1/3} f}{3(S_0^{1/3} f + c)}, \quad (3.1.22)$$

$$\frac{\partial d}{\partial c} = \frac{2 \text{Log } e}{c} \left[1 - \frac{c}{S_0^{1/3} + c} \right]. \quad (3.1.23)$$

The partials with respect to $\text{Log } S_0$ are equal to one for $f \ll f_c$ and $1/3$ for $f \gg f_c$. The partials with respect to c are zero at zero frequency and increase to a maximum value of $\frac{2 \text{Log } e}{c}$ for $f \gg f_c$. Examples of partials with respect to the two source parameters are displayed in Figure 3.2.

The system of equations defined by (3.1.14) is over-determined, and an exact solution is not available. The solution that minimizes the data residual in the least-squares sense is given by the normal equations

$$\Delta m = (A^T A)^{-1} A^T \Delta d \quad (3.1.24)$$

The damped least-squares solution, for damping factor λ , is

$$\Delta m = (A^T A + \lambda J)^{-1} A^T \Delta d \quad (3.1.25)$$

The actual matrix inversion was done using the *bordering method* (Press, et al. 1986). Singular value decomposition was also used to solve the generalized inversion, but was found to give the same result as bordering, which can be done much faster.

3.2 Assumptions

In this section we discuss the simplifying assumptions used in the inversion. The dependence of the results on these assumptions is investigated later in Section 6.3.

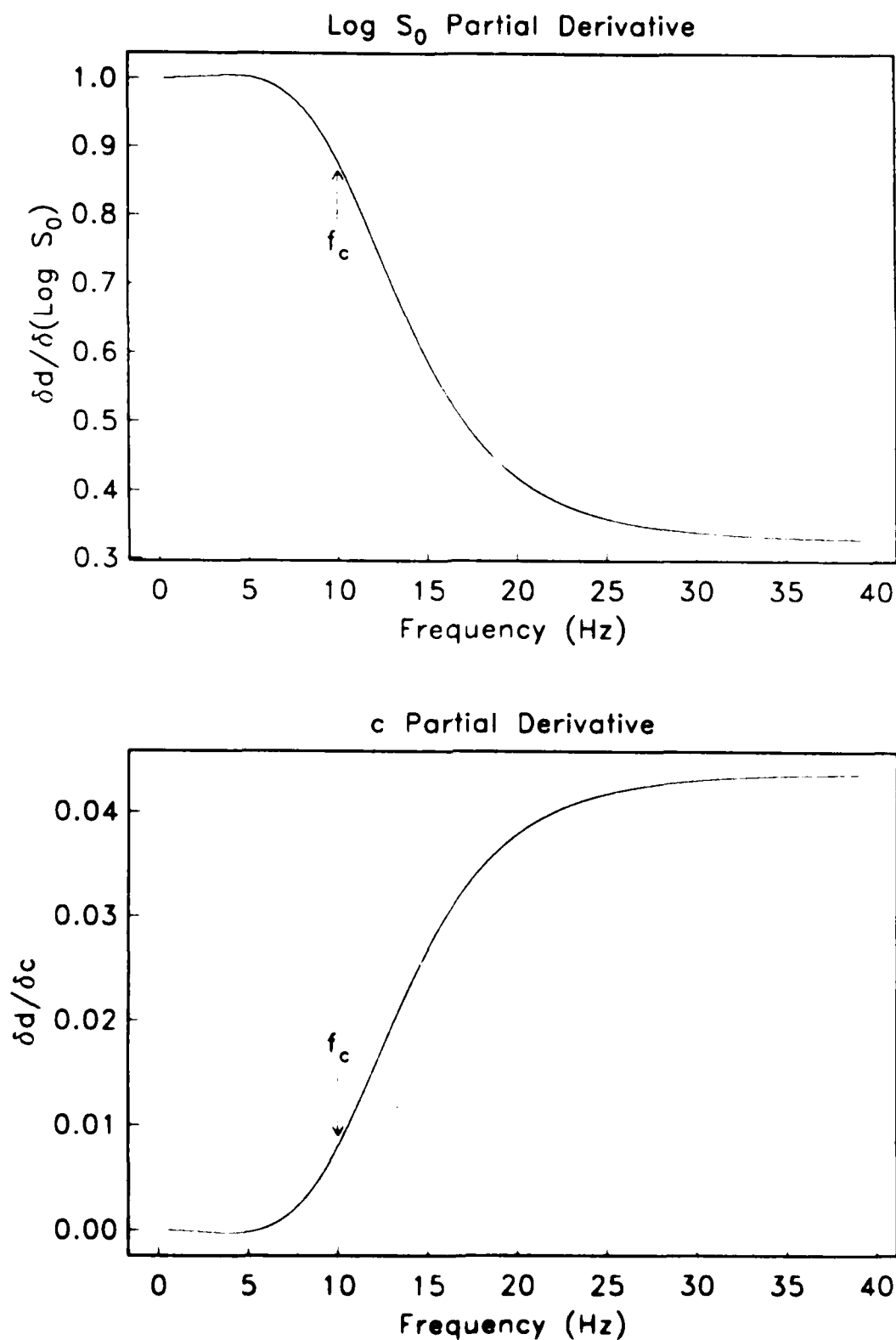


Figure 3.2. Examples of partial derivatives of the data (log amplitude spectra) with respect to long period source level, $\text{Log } S_0$ (3.1.20), and corner frequency parameter, c (3.1.21), for an explosion with $M_0 \approx 10^{20}$ dyne-cm and corner frequency, $f_c = 10$ Hz.

3.2.1 Source spectra

We assume that the source spectrum is uniquely defined by its long period level. This is a common assumption which has a controlling influence in some studies of Q . However, it is not crucial for our analysis because most of the events studied have $M_L < 3.0$, so their corner frequencies are near or beyond the upper limit of bandwidth inverted. For example, the bandwidth for Lg is 1-7 Hz, and we found that inversion with a flat source spectrum gives nearly the same Q as one with the more realistic source functions.

For the characteristics of the source beyond the corner frequency, we follow the practice of the vast majority of the seismological literature and assume the source spectrum follows an ω^2 decay. The theoretical basis for this assumption is not very strong, but careful empirical studies generally support its validity. For example, Chael (1987) studied 12 aftershocks ($3.3 \leq m_{bLg} \leq 5.8$) of the 1982 Miramichi earthquake and found that the data strongly favor ω^2 over ω^3 source models. He used spectral ratios of large to small co-located events to eliminate the shared path contribution and to measure the spectral decay between the two corner frequencies. Another issue is the scaling of corner frequency with event size, which is a subject of numerous studies in the literature. The most straightforward assumption is cube-root scaling, though it is recognized that the scaling can also be by a smaller exponent due to changes in source depth (explosions) or stress drop (earthquakes) that correlate with event size.

Specifically, we have incorporated the Brune (1970, 1971) earthquake source model (3.1.5) and the Mueller-Murphy (1971) explosion model (3.1.4) into the inversion. Most of the events in our data base are small, near-surface mining explosions that appear to have corner frequencies higher than 7 Hz. In Section 5, results for the Mueller-Murphy model are presented and in Section 6.3 we study the effect of altering our source assumptions.

3.2.2 Geometric spreading

The geometric spreading of regional Lg phases is well-constrained, both empirically and theoretically. The onset consists of higher mode surface waves which are accurately described at long ranges by cylindrical spreading. The choice of r_0 in (3.1.2), the transition distance between spherical and cylindrical spreading, was estimated empirically by Street, et al. (1975). It was later substantiated theoretically by Herrmann and Kijko (1983) as approximately twice the crustal thickness. We adopt their value of $r_0 = 100$ km for the results presented in Section 5. Because all of the events used in this study were at ranges greater than r_0 , its value has no

effect on the Q estimate, but it trades off directly with the seismic moment estimate for each event.

The spreading rate of regional Pn phases is not well-constrained. Pn samples a small fraction of the focal sphere, and its geometric spreading rate is dependent upon velocity gradients in the upper mantle. An important constraint on Pn spreading is that the ratio between Lg and Pn long period source levels be range-independent. This criterion supports a choice of $r^{-1.3}$ for the Pn spreading rate, and this is used for the results of Section 5. Results for other spreading rates between r^{-1} and r^{-2} are investigated in Section 6.3.

3.2.3 $Q(f)$ parameterization

We choose a simple parameterization of the range-dependent decay of the seismic spectrum in terms of a power-law frequency dependence of Q . We do not attempt to distinguish intrinsic absorption from scattering. That is, we explicitly acknowledge that our $Q(f)$ is an empirical parameterization of the data and do not address the interpretation in terms of rheology. The justification of this parameterization is its compatibility with other studies (for comparison) and the fact that it does allow us to obtain satisfactory agreement between observed and theoretical spectra.

3.2.4 Radiation pattern

In assuming that corner frequency is inversely proportional to the cube-root of the long period source level, we have assumed isotropic radiation. While this is reasonable for explosions, it could result in significant error for earthquakes. A large event near a P -wave nodal plane will have a small $S_0(Pn)$ and a low corner frequency, which cannot be modeled with our parameterization. Focal mechanisms are not available for the small events in our data set. We have run the inversion on a subset of known explosions, and on the full data set, with most of the added events probably being earthquakes. We note that the variance of the inversion increases for the full data set, presumably due to unmodeled radiation pattern effects. However, the results do not change significantly, which indicates that the radiation pattern is not biasing the estimated parameters. Because Lg samples a larger fraction of the focal sphere, the radiation pattern is of less concern for Lg than for Pn .

3.2.5 Interference phenomena

The constructive and destructive interference of multiple arrivals can modulate the observed seismic spectrum. Examples include spectral scalloping resulting from interfering depth phases,

local site resonances, and multiple sources. Time lags greater than approximately 0.5s are of little concern, since frequency smoothing suppresses that effect. Multiples with lags less than 150 ms can, however, degrade the accuracy of the Q estimate. As an example, Baumgardt and Ziegler (1987) attributed a broad spectral peak centered near 7 Hz to ripple-firing of mine blasts with delays of the order of 150 ms. In this case, destructive interference could increase the observed spectral decay rate between approximately 7 and 14 Hz. However, for this to have a significant impact on our results, ripple-firing with very consistent time lags at many different mine locations would have to occur. For time lags greater than 150 ms, the inversion finds a smooth curve that fits through the modulated spectra. Many examples are pictured in Appendix B .

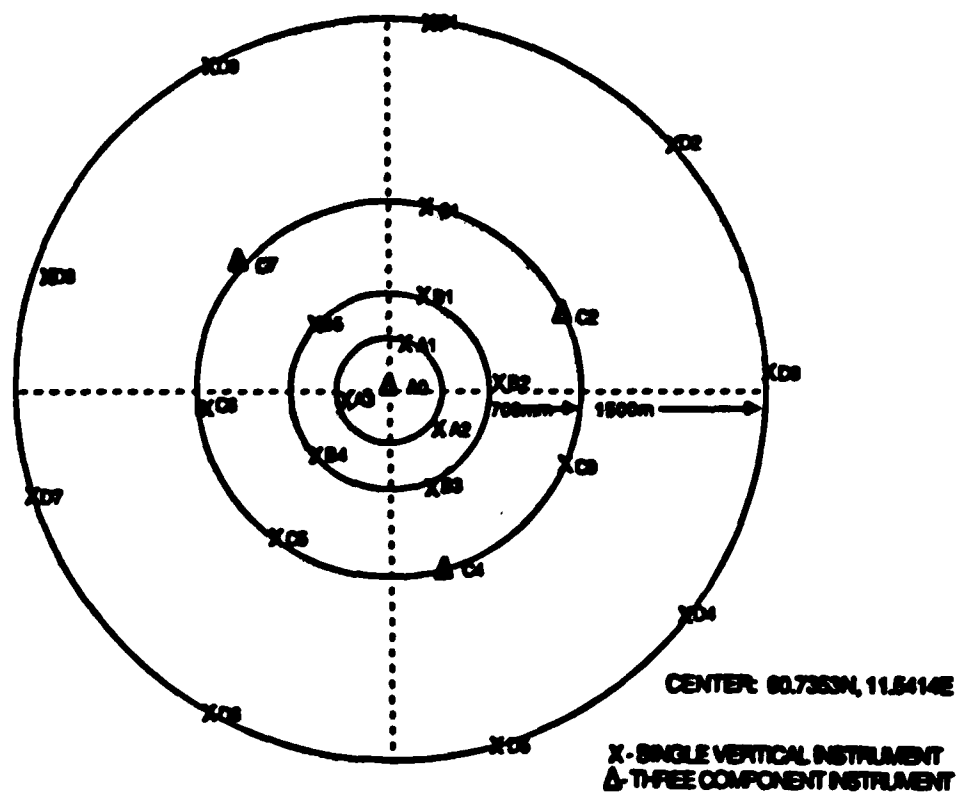
4. DATA BASE

The data used in this study consist of stable, array-averaged spectra for 190 regional events recorded by the small aperture NORESS seismic array in Norway. The NORESS array configuration and sampling rate were designed to enhance the detection of signals from small regional events (Mykkeltveit, et al., 1983). The array includes 25 short period instruments in concentric rings with maximum diameter of 3 km. The data are digitally recorded at 40 samples/s. Figure 4.1 shows the NORESS array configuration and the short period instrument response to the Nyquist frequency.

4.1 Signal processing

The calculation of seismic spectra is incorporated into an automated seismic array processing program (SA/AP) developed at SAIC as an extension of the *RONAPP* program used at NOR-SAR (Mykkeltveit and Bungum, 1984). The program computes spectra for each automatically detected signal. The spectral estimation technique is that proposed by Bache, et al. (1985). A 10% cosine-squared taper is applied to a 5s window starting 0.3s before the onset time of the arrival on the vertical component. The time series is padded with zeros to 1024 samples and fast Fourier transformed. The same procedure is applied to a noise sample taken prior to the first *P* detection. The squared noise amplitude spectrum (power) is subtracted from the squared signal spectrum (energy density). The resulting noise-corrected signal spectra are averaged across the array and corrected for the instrument response. Bache, et al. (1985) demonstrated that if the noise is random, stationary, and uncorrelated with the signal, the signal spectrum estimate obtained with this method converges to the true signal spectrum as the number of elements increases. Array-averaging has the desirable effect of suppressing uncorrelated near-receiver local site effects.

Since the seismic spectra are computed with fixed time window lengths, they encompass different group velocity windows at different ranges. We note that the spectra computed this way may be different from those computed with fixed group velocity windows, particularly for *Lg*, where short range spectra contain contributions from more modes than long range spectra which are confined to a smaller group velocity window. For example, Chun, et al. (1987) estimated vertical component *Lg* attenuation using both fixed window lengths and fixed group velocity windows on the same data set. Using ECTN (Eastern Canada Telemetered Network) *Lg* data, they found $Q(f) = 800f^{0.26}$ for a fixed time window of 17.07s. For a fixed group velocity window of 3.61 to 2.6 km/s, they found $Q(f) = 1100f^{0.19}$. Their data spanned distances of 90 to 867 km, so the time windows varied from 9.7s to 93s. It is not clear whether



NORESS Short Period Instrument Response

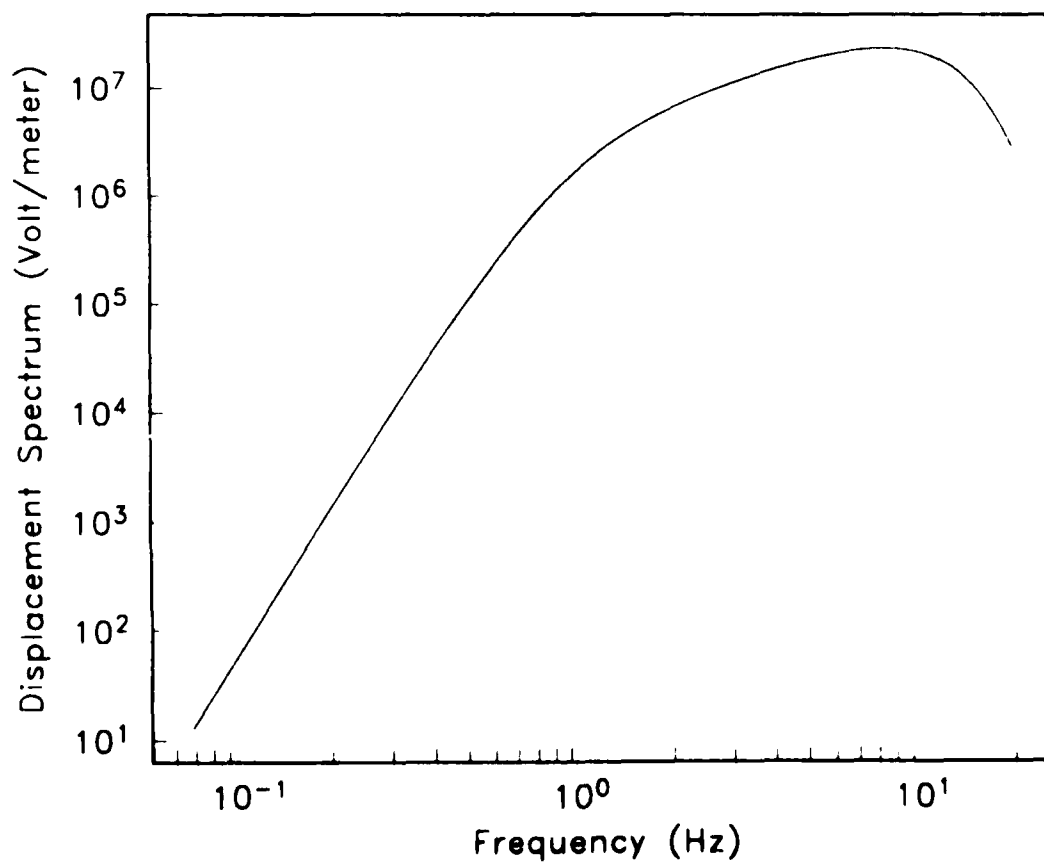


Figure 4.1. NORESS array configuration and short period instrument response.

the fixed time window gives higher attenuation because the lower order, low group velocity modes are not included at large distance (the explanation preferred by Chun, et al., 1987) or because increased scattered energy and/or greater noise contamination is included in the long time segments. The situation is further complicated by the increased possibility that spurious arrivals are included in the long window. In any case, we have chosen fixed time windows because they are most convenient for automatic processing, and our results correctly represent the spectral character of *Lg* windowed in this way.

As a final step in the signal processing, the log amplitude spectra are smoothed over a 2 Hz frequency band. As an example, Figure 4.2 compares the smoothed *Pn* spectrum to the array-averaged spectrum obtained by the automatic processing. The dashed curve is the average noise spectrum estimated from samples taken prior to *Pn* for many events (Henson and Bache, 1986).

4.2 Data

Table 4.1 is a list of all events and phases (*Pn* and/or *Lg*) used in the inversion. In some cases only one phase was included because the other was not detected or because it had a low signal/noise ratio over the frequency band used in the inversion. Reported mining explosions are identified by an "EX" under the column heading, *TYPE*. The label following "EX" identifies the mine. Three are in southwest Norway; BLA (Blasjo), TIT (Titania), and NYG (Nygardstaugen). Other mine codes are those used in the bulletin published by the University of Helsinki based on the Finish Seismic Array. The mine locations are listed in Table 4.2, along with distance and azimuth from NORESS, and are displayed in Figure 4.3. An "EQ" designator identifies presumed earthquakes, although some may be unreported explosions. Events that are not reported explosions, but have locations within 50 km of known mines are considered of unknown source type. The only exception is event 10 of Table 4.1, which was labeled by a NORSAR analyst as a probable dam explosion.

The location and origin times are from a local bulletin published by the University of Bergen or the University of Helsinki, when available, or from the Preliminary Determination of Epicenters (PDE) bulletin. Events for which an independent network solution is not available are assigned either *RONAPP* (single asterisk) or *SAIAP* (double asterisk) locations. The *RONAPP* locations are published in the NORESS bulletin, along with the detection times of the *P* and *Lg* phases used in the location solutions. In some cases *RONAPP* did not associate phases correctly, and we were able to use the *SAIAP* solution with the appropriate phase association.

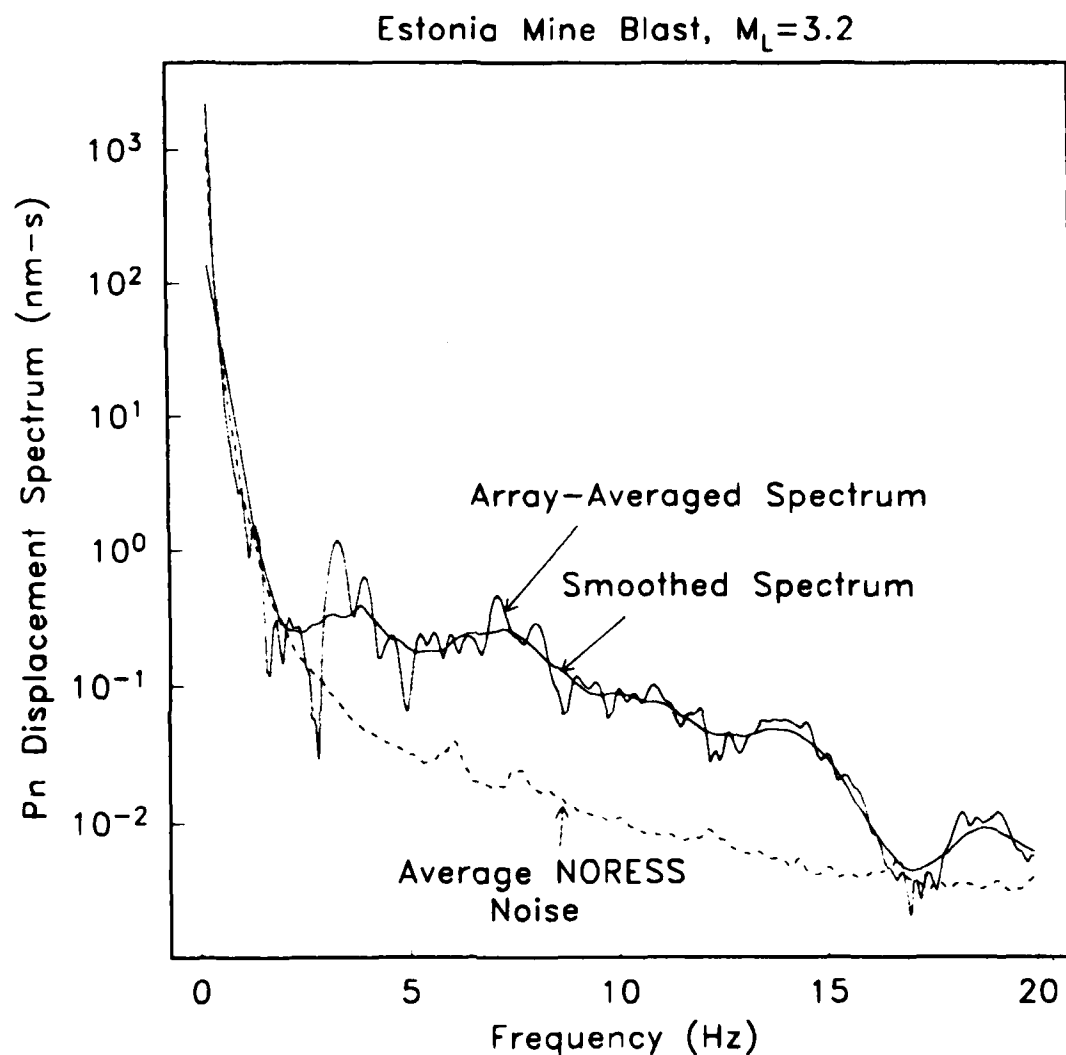


Figure 4.2. Array-averaged P_n displacement spectrum of a $M_L = 3.2$ Estonia mine blast at a range of 930 km. Superimposed is the same spectrum smoothed over a 2 Hz bandwidth. The dashed curve represents average NORESS noise estimated from samples taken prior to P_n for many events (Henson and Bache, 1986).

Table 4.1. Events used in the generalized inversion.

Event	Date	Time	Location	Type	Phases		M_L	
1	10-25-85	12:04	59.30N 28.10E	EX-E7	<i>Pn</i>	<i>Lg</i>	3.0	
2	10-27-85	4:36	61.30N 4.30E	EQ	<i>Pn</i>	<i>Lg</i>	2.8	(B)
3	10-27-85	4:41	66.40N 11.60E*	EQ	<i>Pn</i>	<i>Lg</i>	2.3	
4	10-27-85	4:52	66.00N 14.10E**	EQ	<i>Pn</i>	<i>Lg</i>	2.2	
5	10-29-85	10:23	59.31N 6.95E	EX-BLA	<i>Pn</i>	<i>Lg</i>	1.9	(R)
6	10-31-85	2:56	62.78N 18.03E	EQ	<i>Pn</i>	<i>Lg</i>	2.8	
7	10-31-85	14:11	60.70N 29.00E	EX-V5	<i>Pn</i>	<i>Lg</i>	2.8	
8	11- 6-85	14:51	59.31N 6.95E	EX-BLA	<i>Pn</i>	<i>Lg</i>	2.4	
9	11- 9-85	14:43	58.34N 6.43E	EX-TIT	<i>Pn</i>	<i>Lg</i>	2.1	
10	11- 9-85	18:21	62.60N 6.70E**	--	<i>Pn</i>	<i>Lg</i>	2.0	(R)
11	11-12-85	12:22	59.50N 25.00E	EX-E3		<i>Lg</i>	2.6	
12	11-13-85	12:08	59.30N 28.10E	EX-E7	<i>Pn</i>	<i>Lg</i>	2.7	
13	11-13-85	14:11	58.34N 6.43E	EX-TIT	<i>Pn</i>	<i>Lg</i>	1.9	
14	11-14-85	12:52	60.70N 28.70E	EX-V12	<i>Pn</i>	<i>Lg</i>	2.9	
15	11-15-85	13:54	61.10N 29.90E	EX-V8	<i>Pn</i>		2.9	
16	11-21-85	11:50	59.30N 27.20E	EX-E4		<i>Lg</i>	2.4	(H)
17	11-21-85	13:17	59.29N 7.04E	--	<i>Pn</i>	<i>Lg</i>	1.9	
18	11-23-85	13:06	59.50N 25.00E	EX-E3		<i>Lg</i>	2.5	
19	11-25-85	13:06	59.40N 28.50E	EX-E8		<i>Lg</i>	3.0	
20	11-27-85	4:54	59.73N 5.71E	EQ	<i>Pn</i>	<i>Lg</i>	3.0	
21	11-27-85	12:18	61.40N 31.60E	EX-V4	<i>Pn</i>		2.8	
22	11-28-85	9:30	57.90N 11.50E**	EQ	<i>Pn</i>	<i>Lg</i>	2.1	(R)
23	11-30-85	19:05	61.55N 4.65E	EQ	<i>Pn</i>	<i>Lg</i>	3.0	
24	12- 1-85	7:21	67.70N 33.70E	EX-K1		<i>Lg</i>	2.8	
25	12- 5-85	12:25	61.10N 30.20E	EX-V2	<i>Pn</i>		<2.0	(H)
26	12- 7-85	13:18	59.30N 27.20E	EX-E4		<i>Lg</i>	3.1	
27	12- 7-85	14:16	60.19N 5.25E	--	<i>Pn</i>	<i>Lg</i>	2.2	
28	12- 7-85	14:39	58.90N 5.98E	EQ	<i>Pn</i>	<i>Lg</i>	1.9	
29	12-10-85	12:06	59.40N 28.50E	EX-E8		<i>Lg</i>	3.2	
30	12-10-85	12:18	60.60N 29.20E	EX-V11	<i>Pn</i>	<i>Lg</i>	2.0	(R)
31	12-10-85	13:43	59.72N 22.56E	EQ	<i>Pn</i>	<i>Lg</i>	2.0	
32	12-11-85	12:14	59.40N 28.50E	EX-E8	<i>Pn</i>	<i>Lg</i>	3.3	
33	12-11-85	12:51	59.30N 27.60E	EX-E6		<i>Lg</i>	2.8	
34	12-13-85	12:09	59.40N 28.50E	EX-E8	<i>Pn</i>	<i>Lg</i>	2.8	
35	12-14-85	14:35	61.10N 30.20E	EX-V2	<i>Pn</i>		2.4	(H)
36	12-17-85	13:08	61.10N 30.20E	EX-V2	<i>Pn</i>		2.5	(H)
37	12-23-85	4:27	50.18N 12.35E	EQ	<i>Pn</i>		3.2	(R)
38	12-24-85	0:04	50.17N 12.44E	EQ	<i>Pn</i>		2.6	(R)
39	12-24-85	13:13	59.50N 25.00E	EX-E3		<i>Lg</i>	2.6	
40	12-25-85	12:04	60.90N 29.30E	EX-V1C	<i>Pn</i>	<i>Lg</i>	2.9	
41	12-25-85	13:19	59.30N 27.60E	EX-E6		<i>Lg</i>	2.6	
42	12-25-85	14:18	60.00N 28.50E**	EQ	<i>Pn</i>	<i>Lg</i>	2.7	
43	12-27-85	11:06	61.40N 31.60E	EX-V4	<i>Pn</i>		2.2	(H)
44	12-27-85	12:16	59.40N 28.50E	EX-E8	<i>Pn</i>	<i>Lg</i>	3.3	
45	12-27-85	12:42	61.10N 30.20E	EX-V2	<i>Pn</i>		2.4	(H)

Event	Date	Time	Location	Type	Phases		M_L	
46	12-28-85	11:47	57.69N 26.54E	EQ	<i>Pn</i>	<i>Lg</i>	2.8	
47	12-29-85	21:38	73.29N 6.86E	EQ	<i>Pn</i>		4.7	(P)
48	12-30-85	12:03	59.50N 26.50E	EX-E9		<i>Lg</i>	2.7	
49	12-30-85	12:19	59.31N 27.34E	--		<i>Lg</i>	2.7	
50	12-31-85	6:57	73.36N 6.77E	EQ	<i>Pn</i>		4.8	(P)
51	12-31-85	7:10	73.29N 6.70E	EQ	<i>Pn</i>		4.6	(P)
52	12-31-85	12:08	63.20N 27.80E	EX-M7	<i>Pn</i>		2.3	(H)
53	12-31-85	13:37	58.34N 6.43E	EX-TIT	<i>Pn</i>	<i>Lg</i>	2.1	
54	1- 3-86	14:59	61.90N 30.60E	EX-V7	<i>Pn</i>	<i>Lg</i>	2.9	
55	1- 7-86	11:20	60.92N 29.05E	--	<i>Pn</i>	<i>Lg</i>	2.8	
56	1- 7-86	14:14	58.34N 6.43E	EX-TIT	<i>Pn</i>	<i>Lg</i>	1.8	
57	1- 9-86	1:59	66.80N 21.80E*	EQ		<i>Lg</i>	2.6	
58	1- 9-86	12:08	59.30N 28.10E	EX-E7	<i>Pn</i>	<i>Lg</i>	2.5	
59	1-13-86	12:06	59.64N 24.07E	--	<i>Pn</i>	<i>Lg</i>	2.7	
60	1-15-86	12:06	59.40N 28.50E	EX-E8	<i>Pn</i>	<i>Lg</i>	3.4	
61	1-16-86	12:08	59.40N 28.50E	EX-E8	<i>Pn</i>	<i>Lg</i>	2.7	
62	1-17-86	12:12	59.30N 28.10E	EX-E7	<i>Pn</i>	<i>Lg</i>	3.3	
63	1-17-86	14:11	58.34N 6.43E	EX-TIT	<i>Pn</i>	<i>Lg</i>	2.3	
64	1-20-86	23:38	50.18N 12.31E	EQ	<i>Pn</i>	<i>Lg</i>	3.3	
65	1-21-86	8:56	55.30N 13.60E*	EQ	<i>Pn</i>	<i>Lg</i>	2.5	
66	1-25-86	22:58	57.10N 7.00E**	EQ	<i>Pn</i>	<i>Lg</i>	1.7	
67	1-25-86	23:13	61.48N 16.94E	EQ	<i>Pn</i>	<i>Lg</i>	2.9	
68	1-31-86	6:00	65.39N 10.65E	EQ	<i>Pn</i>	<i>Lg</i>	2.5	
69	1-31-86	10:49	61.10N 29.90E	EX-V8	<i>Pn</i>	<i>Lg</i>	3.3	
70	1-31-86	12:10	59.30N 28.10E	EX-E7	<i>Pn</i>	<i>Lg</i>	3.3	
71	1-31-86	14:18	58.34N 6.43E	EX-TIT	<i>Pn</i>	<i>Lg</i>	1.9	
72	2- 2-86	4:57	67.60N 34.00E	EX-K2		<i>Lg</i>	2.9	
73	2- 3-86	1:30	59.60N 1.43E	EQ		<i>Lg</i>	1.9	
74	2- 5-86	15:23	62.60N 6.80E*	EQ		<i>Lg</i>	1.6	
75	2- 5-86	23:36	62.74N 4.50E	EQ	<i>Pn</i>	<i>Lg</i>	2.3	
76	2- 6-86	6:20	62.90N 4.86E	EQ	<i>Pn</i>	<i>Lg</i>	1.9	
77	2- 6-86	12:22	59.30N 28.10E	EX-E7	<i>Pn</i>	<i>Lg</i>	2.6	
78	2- 6-86	16:30	67.10N 20.60E	EX-R1		<i>Lg</i>	2.6	
79	2 -7-86	11:00	64.70N 30.70E	EX-V10	<i>Pn</i>	<i>Lg</i>	3.1	
80	2 -7-86	12:09	59.40N 28.40E	EX-E12		<i>Lg</i>	2.5	
81	2- 7-86	12:17	59.20N 31.00E**	EQ		<i>Lg</i>	1.9	(R)
82	2- 7-86	14:05	67.60N 34.20E	EX-K5	<i>Pn</i>	<i>Lg</i>	2.8	(H)
83	2 -7-86	21:03	66.45N 14.89E	EQ	<i>Pn</i>	<i>Lg</i>	2.2	(H)
84	2-10-86	12:42	59.40N 28.50E	EX-E8	<i>Pn</i>	<i>Lg</i>	2.7	
85	2-13-86	19:04	62.61N 5.07E	EQ		<i>Lg</i>	2.2	
86	2-14-86	14:13	58.34N 6.43E	EX-TIT	<i>Pn</i>	<i>Lg</i>	2.4	
87	2-14-86	17:54	58.34N 6.43E	EX-TIT	<i>Pn</i>		2.3	(B)
88	2-15-86	18:32	59.86N 5.73E	EQ		<i>Lg</i>	1.8	
89	2-16-86	4:33	67.10N 20.60E	EX-R1		<i>Lg</i>	2.5	
90	2-16-86	18:20	61.69N 4.90E	EQ	<i>Pn</i>	<i>Lg</i>	1.7	
91	2-17-86	12:37	59.30N 27.20E	EX-E4		<i>Lg</i>	2.5	(H)
92	2-18-86	10:46	59.30N 27.20E	EX-E4		<i>Lg</i>	3.1	
93	2-18-86	12:46	64.70N 30.70E	EX-V10	<i>Pn</i>	<i>Lg</i>	2.6	

Event	Date	Time	Location	Type	Phases		M_L	
94	2-23-86	6:14	67.60N 34.00E	EX-K2	<i>Pn</i>	<i>Lg</i>	3.1	
95	2-26-86	2:12	62.76N 5.29E	EQ	<i>Pn</i>	<i>Lg</i>	1.9	
96	3- 5-86	12:13	59.50N 26.50E	EX-E9		<i>Lg</i>	3.2	
97	3- 5-86	13:02	57.20N 7.00E**	EQ	<i>Pn</i>	<i>Lg</i>	1.8	
98	3- 7-86	13:08	59.30N 28.10E	EX-E7	<i>Pn</i>	<i>Lg</i>	3.3	
99	3- 8-86	16:21	61.67N 2.58E	EQ	<i>Pn</i>	<i>Lg</i>	1.9	
100	3-10-86	4:20	62.81N 4.91E	EQ	<i>Pn</i>	<i>Lg</i>	2.1	
101	3-10-86	12:02	59.30N 28.10E	EX-E7	<i>Pn</i>	<i>Lg</i>	3.2	
102	3-11-86	12:02	59.30N 28.10E	EX-E7	<i>Pn</i>	<i>Lg</i>	3.2	
103	3-13-86	10:27	61.10N 29.90E	EX-V8	<i>Pn</i>		2.8	
104	3-13-86	11:39	60.70N 29.00E	EX-V5	<i>Pn</i>	<i>Lg</i>	2.9	
105	3-14-86	8:33	67.60N 34.20E	EX-K5		<i>Lg</i>	2.8	
106	3-21-86	13:02	59.50N 25.00E	EX-E3		<i>Lg</i>	2.6	
107	3-24-86	11:18	59.30N 27.20E	EX-E4	<i>Pn</i>	<i>Lg</i>	2.5	
108	3-25-86	9:05	62.76N 4.76E	EQ	<i>Pn</i>	<i>Lg</i>	2.0	
109	3-27-86	12:24	59.40N 28.50E	EX-E8	<i>Pn</i>	<i>Lg</i>	3.5	
110	3-30-86	3:23	61.66N 4.53E	EQ	<i>Pn</i>	<i>Lg</i>	1.6	
111	4- 4-86	13:13	58.34N 6.43E	EX-TIT	<i>Pn</i>	<i>Lg</i>	1.9	
112	4- 4-86	22:43	70.86N 8.91E	EQ	<i>Pn</i>		4.4	(H)
113	4- 7-86	0:35	61.84N 4.88E	EQ	<i>Pn</i>	<i>Lg</i>	2.0	
114	4-14-86	14:55	59.49N 24.11E	--	<i>Pn</i>	<i>Lg</i>	2.8	
115	4-15-86	10:53	60.90N 29.30E	EX-V1C	<i>Pn</i>	<i>Lg</i>	3.0	
116	4-16-86	11:51	60.39N 5.34E	EX-NYG		<i>Lg</i>	1.8	(B)
117	4-16-86	13:15	58.15N 5.97E	--	<i>Pn</i>	<i>Lg</i>	2.1	
118	4-18-86	8:33	67.60N 34.00E	EX-K2		<i>Lg</i>	2.7	
119	4-19-86	10:59	61.10N 30.20E	EX-V2	<i>Pn</i>	<i>Lg</i>	2.5	
120	4-28-86	15:53	60.18N 4.88E	--	<i>Pn</i>	<i>Lg</i>	2.4	
121	4-29-86	17:48	59.82N 24.06E	EQ		<i>Lg</i>	2.6	
122	4-30-86	10:19	59.31N 6.95E	EX-BLA	<i>Pn</i>	<i>Lg</i>	2.2	
123	5- 8-86	17:14	58.70N 17.99E	EQ		<i>Lg</i>	2.3	
124	5-16-86	15:02	61.90N 30.60E	EX-V7		<i>Lg</i>	3.1	
125	5-17-86	16:01	62.94N 4.94E	EQ	<i>Pn</i>	<i>Lg</i>	2.4	
126	5-21-86	8:57	61.65N 31.38E	--		<i>Lg</i>	2.6	
127	5-27-86	18:36	59.31N 6.95E	EX-BLA	<i>Pn</i>	<i>Lg</i>	2.3	
128	5-28-86	17:52	59.31N 6.95E	EX-BLA	<i>Pn</i>	<i>Lg</i>	2.4	
129	6- 3-86	11:04	59.17N 5.66E	EQ	<i>Pn</i>	<i>Lg</i>	2.0	
130	6- 3-86	14:30	61.46N 4.08E	EQ	<i>Pn</i>	<i>Lg</i>	2.7	
131	6- 4-86	9:07	61.50N 30.40E	EX-V3	<i>Pn</i>	<i>Lg</i>	3.9	
132	6- 6-86	13:14	58.34N 6.43E	EX-TIT	<i>Pn</i>	<i>Lg</i>	1.7	
133	6- 7-86	12:13	59.20N 27.60E	EX-E5		<i>Lg</i>	3.0	
134	6-12-86	9:31	61.50N 30.40E	EX-V3	<i>Pn</i>		3.7	
135	6-12-86	13:04	60.90N 29.30E	EX-V1C	<i>Pn</i>	<i>Lg</i>	2.6	
136	6-13-86	14:41	59.66N 24.28E	--	<i>Pn</i>	<i>Lg</i>	3.1	
137	6-15-86	15:01	61.67N 3.85E	EQ	<i>Pn</i>	<i>Lg</i>	3.2	
138	6-16-86	15:59	60.04N 7.24E	EQ		<i>Lg</i>	1.1	
139	6-19-86	3:55	59.31N 6.95E	EX-BLA	<i>Pn</i>	<i>Lg</i>	2.5	
140	6-20-86	22:08	61.47N 3.92E	EQ	<i>Pn</i>	<i>Lg</i>	1.6	
141	6-23-86	13:14	58.34N 6.43E	EX-TIT	<i>Pn</i>	<i>Lg</i>	1.8	

Event	Date	Time	Location	Type	Phases		M_L
142	6-25-86	12:33	61.40N 31.60E	EX-V4	<i>Pn</i>	<i>Lg</i>	2.9
143	6-26-86	4:06	61.88N 5.10E	EQ	<i>Pn</i>	<i>Lg</i>	2.1
144	6-27-86	3:50	59.28N 6.76E	--	<i>Pn</i>	<i>Lg</i>	2.4
145	6-27-86	9:00	64.70N 30.70E	EX-V10		<i>Lg</i>	2.6
146	6-30-86	17:11	57.46N 27.22E	EQ	<i>Pn</i>	<i>Lg</i>	2.8
147	7- 1-86	15:28	60.70N 28.70E	EX-V12	<i>Pn</i>	<i>Lg</i>	2.7
148	7- 8-86	12:06	60.04N 29.36E	--	<i>Pn</i>	<i>Lg</i>	3.2
149	7- 8-86	13:09	59.30N 27.20E	EX-E4	<i>Pn</i>	<i>Lg</i>	2.7
150	7-10-86	20:10	59.31N 6.95E	EX-BLA	<i>Pn</i>	<i>Lg</i>	2.3
151	7-12-86	13:38	62.98N 6.47E	EQ	<i>Pn</i>	<i>Lg</i>	2.0
152	7-14-86	13:51	58.33N 13.89E	EQ	<i>Pn</i>		4.3
153	7-14-86	14:30	61.10N 29.90E	EX-V8	<i>Pn</i>	<i>Lg</i>	3.2
154	7-14-86	14:45	58.42N 13.90E	EQ	<i>Pn</i>	<i>Lg</i>	3.4
155	7-14-86	15:02	69.30N 34.40E	EX-K9	<i>Pn</i>	<i>Lg</i>	3.1
156	7-15-86	18:46	66.97N 13.02E	EQ	<i>Pn</i>	<i>Lg</i>	3.5
157	7-16-86	11:27	59.30N 27.20E	EX-E4	<i>Pn</i>	<i>Lg</i>	3.0
158	7-16-86	17:49	59.31N 6.95E	EX-BLA	<i>Pn</i>	<i>Lg</i>	2.3
159	7-18-86	11:03	59.40N 28.50E	EX-E8	<i>Pn</i>	<i>Lg</i>	3.1
160	7-18-86	13:42	59.30N 27.60E	EX-E6	<i>Pn</i>	<i>Lg</i>	3.0
161	7-23-86	13:10	60.80N 29.30E	EX-V1B	<i>Pn</i>	<i>Lg</i>	2.8
162	7-23-86	20:47	59.31N 6.95E	EX-BLA	<i>Pn</i>	<i>Lg</i>	2.2
163	7-24-86	10:56	68.10N 33.20E	EX-K4	<i>Pn</i>		2.6 (H)
164	7-29-86	13:14	59.31N 6.95E	EX-BLA	<i>Pn</i>	<i>Lg</i>	2.3
165	7-30-86	11:03	59.30N 28.10E	EX-E7	<i>Pn</i>	<i>Lg</i>	3.2
166	7-30-86	13:39	59.30N 27.20E	EX-E4		<i>Lg</i>	2.6
167	7-30-86	13:50	59.34N 27.55E	--	<i>Pn</i>	<i>Lg</i>	2.8
168	7-30-86	18:00	59.31N 6.95E	EX-BLA	<i>Pn</i>	<i>Lg</i>	2.4
169	7-31-86	14:23	59.63N 24.48E	--	<i>Pn</i>		3.1
170	7-31-86	15:06	59.40N 24.60E	EX-E2	<i>Pn</i>	<i>Lg</i>	3.0
171	8-13-86	15:32	67.10N 20.60E	EX-R1	<i>Pn</i>	<i>Lg</i>	2.6
172	8-14-86	13:15	58.34N 6.43E	EX-TIT	<i>Pn</i>	<i>Lg</i>	1.9
173	8-14-86	14:40	59.31N 6.95E	EX-BLA	<i>Pn</i>	<i>Lg</i>	2.4
174	8-16-86	4:25	62.82N 4.98E	EQ	<i>Pn</i>	<i>Lg</i>	2.3
175	9- 1-86	22:11	60.82N 2.93E	EQ	<i>Pn</i>	<i>Lg</i>	3.9
176	9- 2-86	12:54	59.31N 6.95E	EX-BLA	<i>Pn</i>	<i>Lg</i>	2.1
177	9- 4-86	11:23	60.96N 28.99E	--		<i>Lg</i>	3.0
178	9- 9-86	17:56	59.31N 6.95E	EX-BLA	<i>Pn</i>	<i>Lg</i>	2.4
179	9-18-86	15:54	60.77N 20.68E	EQ	<i>Pn</i>	<i>Lg</i>	2.5
180	9-20-86	22:15	60.03N 16.29E	EQ	<i>Pn</i>	<i>Lg</i>	3.3
181	9-30-86	20:03	60.79N 4.23E	EQ	<i>Pn</i>	<i>Lg</i>	1.9
182	10- 1-86	14:15	58.34N 6.43E	EX-TIT	<i>Pn</i>	<i>Lg</i>	1.9
183	10- 9-86	14:14	58.34N 6.43E	EX-TIT	<i>Pn</i>	<i>Lg</i>	2.0
184	10-10-86	19:57	61.97N 2.33E	EQ	<i>Pn</i>	<i>Lg</i>	2.1
185	10-26-86	11:45	61.46N 3.29E	EQ	<i>Pn</i>	<i>Lg</i>	2.4
186	10-26-86	11:57	61.72N 3.27E	EQ	<i>Pn</i>	<i>Lg</i>	2.6 (B)
187	10-29-86	21:05	60.81N 3.04E	EQ	<i>Pn</i>	<i>Lg</i>	2.3
188	11- 1-86	14:55	62.47N 6.19E	EQ	<i>Pn</i>	<i>Lg</i>	2.4
189	11- 2-86	7:48	58.58N 13.44E	EQ	<i>Pn</i>	<i>Lg</i>	3.4 (B)

Event	Date	Time	Location	Type	Phases	M_L
190	11-13-86	8:01	58.17N 8.10E	EQ	P_n L_g	1.8

* *RONAPP* Location

** *SAIAP* Location

(B) Bergen network magnitude

(H) Helsinki network magnitude

(P) PDE magnitude (M_b)

(R) *RONAPP* uncorrected magnitude

Table 4.2. Mine locations

Mine	Location		Distance	Azimuth
M1	60.20N	23.10E	5.71	90.31
M2	61.40N	22.80E	5.48	78.13
M3	60.40N	22.40E	5.34	88.85
M4	61.90N	21.50E	4.91	71.96
M5	61.60N	21.70E	4.97	75.56
M6	62.10N	27.40E	7.69	72.89
M7	63.20N	27.80E	8.00	65.05
M8	64.20N	28.00E	8.33	58.35
M9	64.10N	24.70E	6.94	55.36
M10	64.10N	27.10E	7.92	58.19
M11	64.40N	25.20E	7.26	53.83
M12	62.80N	29.30E	8.62	68.46
M13	63.70N	26.00E	7.34	59.96
M14	62.80N	22.90E	5.75	64.03
M15	62.50N	30.10E	8.96	70.60
M16	63.40N	27.30E	7.82	63.29
M17	63.20N	28.10E	8.14	65.22
M18	63.00N	26.80E	7.52	65.88
M19	62.90N	28.70E	8.36	67.57
M20	62.70N	23.20E	5.85	65.34
M21	62.60N	23.60E	6.01	66.70
M22	65.80N	24.70E	7.76	43.69
M23	63.50N	29.60E	8.85	64.02
M24	63.80N	25.10E	7.00	58.19
M25	65.80N	28.10E	8.96	48.57
M26	61.60N	24.20E	6.16	76.42
E1	59.30N	24.40E	6.57	96.96
E2	59.40N	24.60E	6.64	95.87
E3	59.50N	25.00E	6.81	94.55
E4	59.30N	27.20E	7.94	93.54
E5	59.20N	27.60E	8.16	93.78
E6	59.30N	27.60E	8.13	93.11
E7	59.30N	28.10E	8.37	92.59
E8	59.40N	28.50E	8.54	91.54
E9	59.50N	26.50E	7.54	92.86
E10	60.00N	29.90E	9.08	86.59
E11	59.60N	30.00E	9.22	88.96
E12	59.40N	28.40E	8.49	91.64
V1A	60.90N	29.40E	8.68	81.11
V1B	60.80N	29.30E	8.65	81.81
V1C	60.90N	29.30E	8.63	81.15
V2	61.10N	30.20E	9.05	79.55
V3	61.50N	30.40E	9.11	76.97
V4	61.40N	31.60E	9.69	77.32
V5	60.70N	29.00E	8.51	82.61

Mine	Location		Distance	Azimuth
V6	61.40N	34.30E	10.97	76.60
V7	61.90N	30.60E	9.19	74.43
V8	61.10N	29.90E	8.90	79.64
V9	62.20N	34.30E	10.91	72.40
V10	64.70N	30.70E	9.59	57.37
V11	60.60N	29.20E	8.63	83.18
V12	60.70N	28.70E	8.37	82.74
V13	60.80N	29.50E	8.74	81.73
K1	67.70N	33.70E	11.78	44.49
K2	67.60N	34.00E	11.85	45.16
K3	69.40N	30.80E	11.77	34.66
K4	68.10N	33.20E	11.80	42.32
K5	67.60N	34.20E	11.92	45.32
K6	69.60N	32.30E	12.31	35.40
K7	67.70N	31.40E	11.01	42.44
K8	67.60N	30.50E	10.67	41.99
K9	69.30N	34.40E	12.76	38.43
K10	69.20N	34.70E	12.81	39.05
K11	68.80N	33.00E	12.08	39.21
K12	69.20N	33.30E	12.38	37.87
R1	67.10N	20.60E	7.49	28.02
R2	67.70N	21.00E	8.07	26.37
N1	69.60N	29.90E	11.65	32.92
TIT	58.34N	6.43E	3.57	229.21
BLA	59.31N	6.95E	2.70	240.06
NYG	60.39N	5.34E	3.07	266.06

Mine Locations

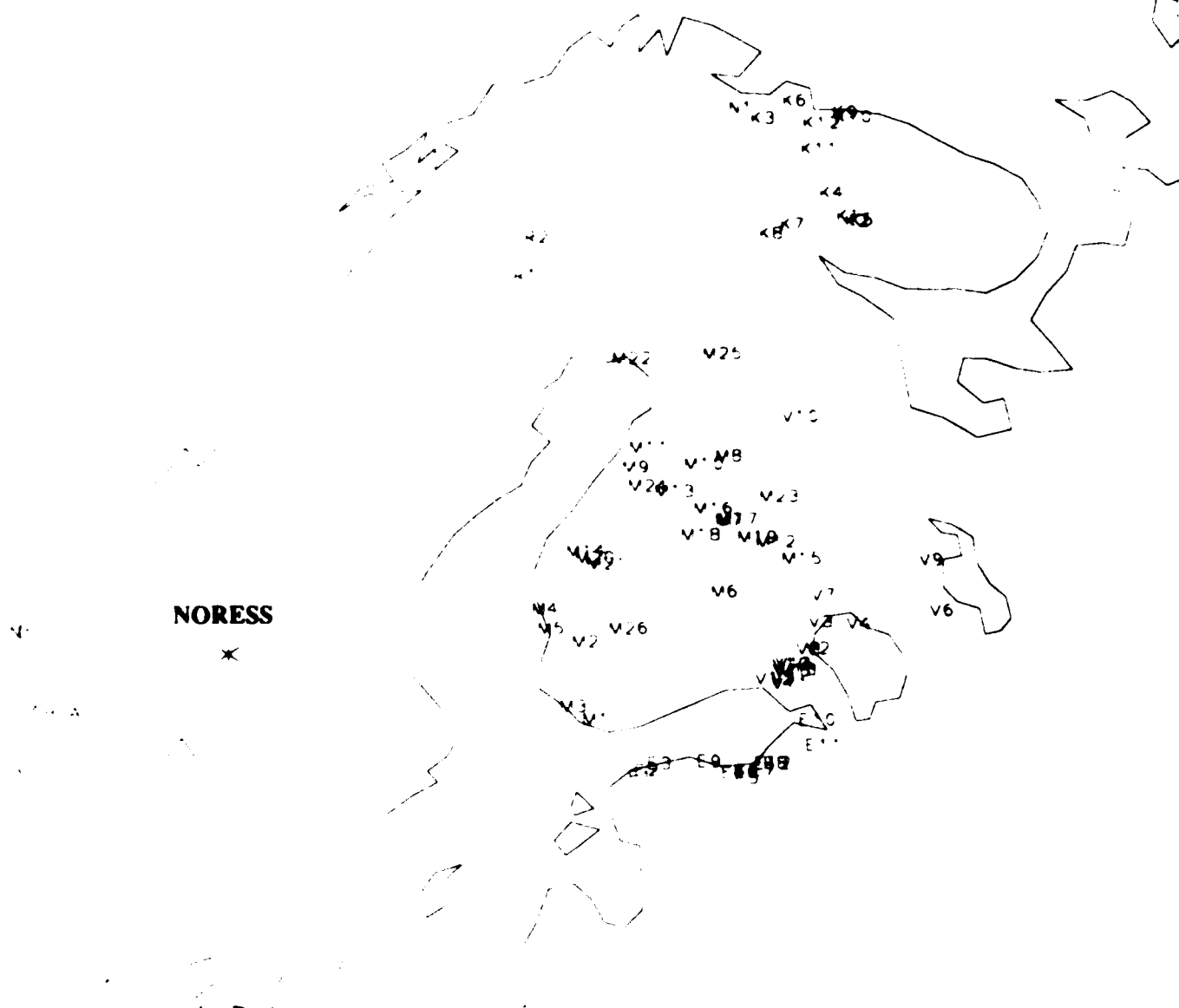


Figure 4.3. Locations of mines listed in Table 4.2.

SAIAP also uses a broad band, frequency-wavenumber calculation (Kvaerna and Ringdal, 1986) that gives more accurate azimuth estimates than those used in the *RONAPP* locations.

The M_L are based on the Lg amplitude computed by *RONAPP*. They differ slightly from the *RONAPP* M_L in the NORESS bulletin by being distance-corrected to the event location computed by one of the independent networks. For some events *RONAPP* had no detected Lg phase, or chose the wrong phase as Lg . For these events the M_L is that reported by one of the independent networks (if available) or the *RONAPP* uncorrected magnitude. These are listed in Table 4.1 for information but were not included in any subsequent analysis. The relation between seismic moment and magnitude (Section 5.4) was derived using only events with distance-corrected NORESS magnitudes.

The 190 events used in the inversion include 109 explosions, 65 presumed earthquakes, and 16 events of unknown source type. The Pn inversion included 152 of these events, with 83 explosions, 56 presumed earthquakes, and 13 events of unknown source type. The Lg inversion included 170 events, including 97 explosions, 58 presumed earthquakes, and 15 unknown. Of the 190 events, 132 were used for both the Pn and the Lg analyses. The NORESS array location and epicenters of events used in the inversion are plotted in Figure 4.4. The distance range 300-450 km is dominated by events in west to southwest Norway, while events from 700 to 1200 km are located primarily to the east of NORESS. If the attenuation along paths to the east is distinctly different from that along paths to the west, it would not be possible to combine them in the same inversion. However, separate inversions were run for restricted azimuth windows, and significant path differences were not observed. From this we conclude that all of the data are adequately represented by a single frequency-dependent Q model.

Appendix A lists an additional 68 events that were processed but that were not used in the inversion. Most were excluded because of low signal/noise ratios. However, there is a set of southwest Norway off-shore events that were excluded because their spectra were inconsistent with other events at approximately the same distance (Henson and Bache, 1986). It is not clear whether the difference is due to anomalous path effects or to a different source spectrum. These events are discussed in more detail in Section 6.5.

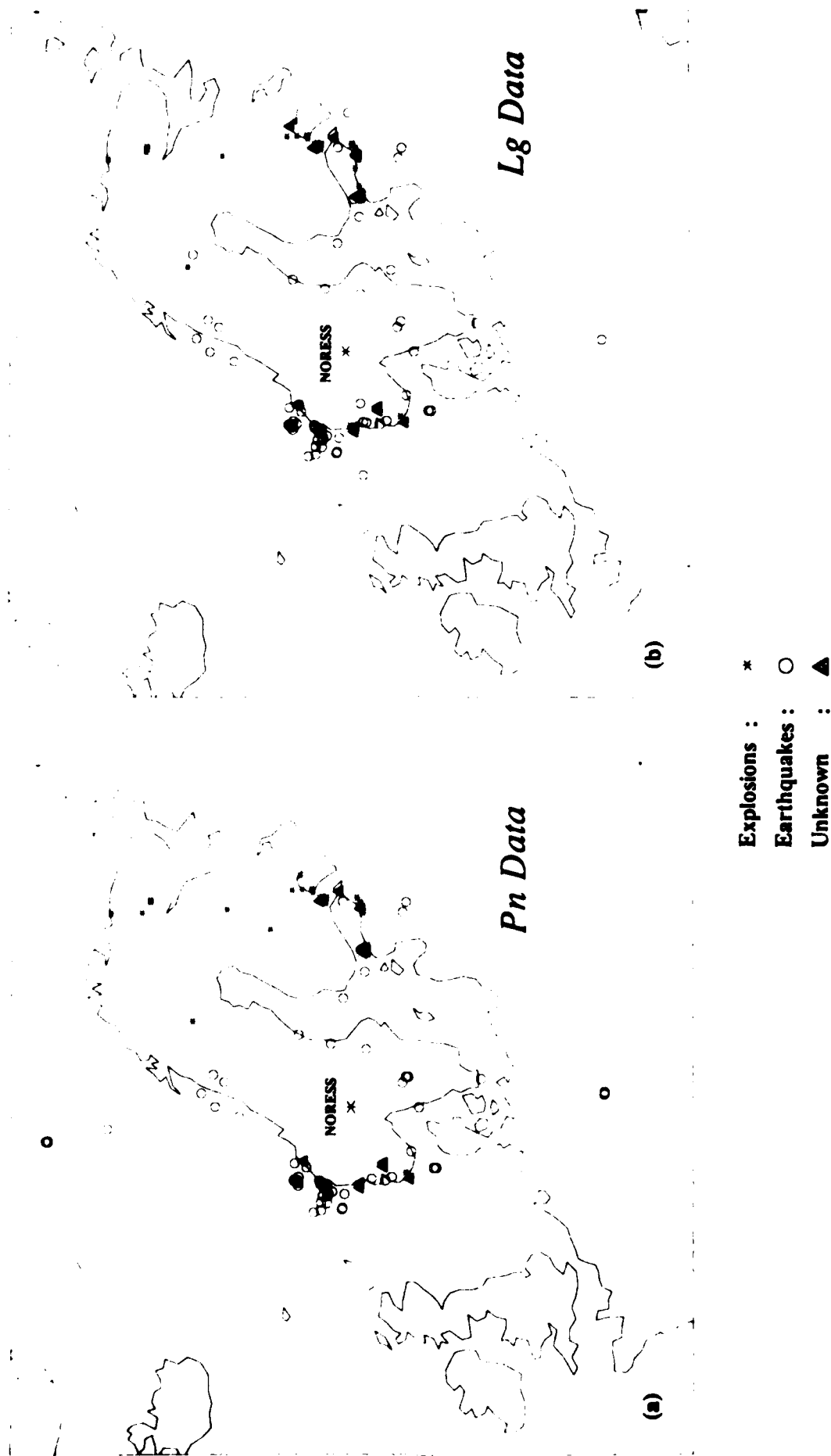


Figure 4.4. Events used in the generalized inversion for (a) P_n and (b) L_g . Earthquakes, explosions, and sources of unknown type are plotted with different symbols. The L_g inversion used spectra of 170 events and the P_n inversion included 152 events.

5. ATTENUATION AND SEISMIC MOMENT ESTIMATES

In this section we present the primary results of this study. The generalized inversion described in Section 3 is applied to regional Pn and Lg spectra recorded at NORESS from 190 events with epicentral distances ranging between 200 and 1300 km. The data used for the separate Pn and Lg inversions were described in Section 4. In this section, we adopt the Mueller-Murphy explosion source model (3.1.4) and geometric spreading defined by (3.1.2) with $m = 1/2$ and $r_0 = 100$ km for Lg and $m = 1.3$ and $r_0 = 1$ km for Pn . In Section 6, the dependence of our results on these assumptions is investigated.

For a given set of source and spreading assumptions, the inversion clearly defines a broad minimum in the data residuals corresponding to a suite of models that fit the data equally well in a least-squares sense. These models involve trade-offs among M_0 , Q_0 , and η . The low frequency spectral level depends upon M_0 and Q_0 . If M_0 increases, then Q_0 will decrease to preserve the fit to the long period spectral level. This trade-off is, however, limited by the spectral slope at low frequencies. In response to the high frequency spectrum, decrease in Q_0 trades-off with increase in η . The parameter c relating M_0 to corner frequency (3.1.6) is fixed by the few events large enough to have a corner frequency within the band used in the inversion. Therefore, when M_0 increases, c increases to retain approximately the same corner frequency for the larger events. To resolve these trade-offs among models that give essentially the same data variance, we add the constraint that the derived source parameters for Lg and Pn , which are inverted separately, be consistent. In this section, the results for our "preferred model" are presented. The trade-off among model parameters is discussed in detail in Section 6.

5.1 Regional Lg spectra

Regional Lg spectra of 170 events (Table 4.1) were inverted simultaneously for seismic moment and $Q(f)$. At ranges greater than about 800 km, the Lg signal/noise ratio is inadequate for most events above 7 or 8 Hz, while at shorter distances Lg spectra are probably contaminated by Sn coda at high frequency (Chun, et al., 1987; Ringdal, 1986; Shin and Herrmann, 1987). The Lg inversion was therefore band limited to frequencies between 1 and 7 Hz. The spectra were smoothed over a 2 Hz bandwidth and sampled every 0.25 Hz. The number of data in the Lg inversion is then 4250, and the number of parameters is 173.

The Lg Q resulting from the inversion is $Q(f) = 350f^{0.41}$. Our short time windows include the onset of Lg which consists of higher mode surface waves sampling, predominantly, the lower crust. Our $Q_{Lg}(f)$ is therefore an approximation to Q of the lower crust, although it also includes the effects of apparent attenuation due to scattering. The parameter c derived from Lg spectra is 28.7. The inverted long period source levels for each event are tabulated in Appendix B. Selected examples of the fit of theoretical spectra to data spectra are shown in Figure 5.1. All of these events have corner frequencies greater than 6 Hz, so the source parameterization has only a minor effect on the results. A complete catalog of the fit to all spectra used in the inversion can be found in Appendix B.

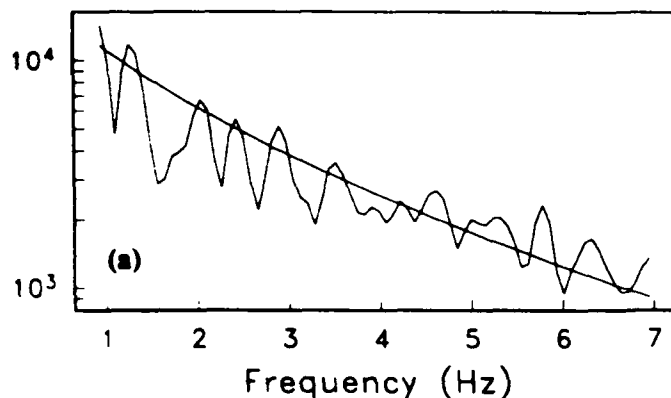
Table 2.1 and Figure 2.1 summarize reported Lg attenuation functions for various regions. It was noted in Section 2 that eastern North America (ENA) is characterized by a higher Q_0 and lower frequency exponent than the western United States (WUS). Our $Q_{Lg}(f)$ is between the ENA and WUS estimates. This is surprising since one would expect attenuation in Scandinavia would be more similar to the tectonically stable North American shield. However, predicted spectral shapes for our Q model are more similar to those for the ENA estimates than those based on WUS Q values. This is illustrated in Figure 5.2 which plots $\exp(-\pi ft/Q(f))$ for the Q functions listed in Table 2.1, and for our $Q(f)$. In particular, the spectral shape between 1 and 7 Hz for our Q model is similar to that predicted for the low exponent ENA Q models (entries 6 and 8 of Table 2.1). On the other hand, a large Q_0 and strong frequency-dependence (entry 10) result in spectra that severely overestimate the observed ratio of high to low frequency spectral content of NORESS data. Our $Q_{Lg}(f)$ is actually very similar to that representing central France (Campillo, et al., 1985). The vertical offset between the ENA curves and ours indicates that our model predicts considerably lower amplitudes for events of equivalent M_0 . It is not clear whether paths to NORESS are distinctly different from ENA paths, or if the disparate Q values can be attributed to different methodologies.

5.2 Regional Pn spectra

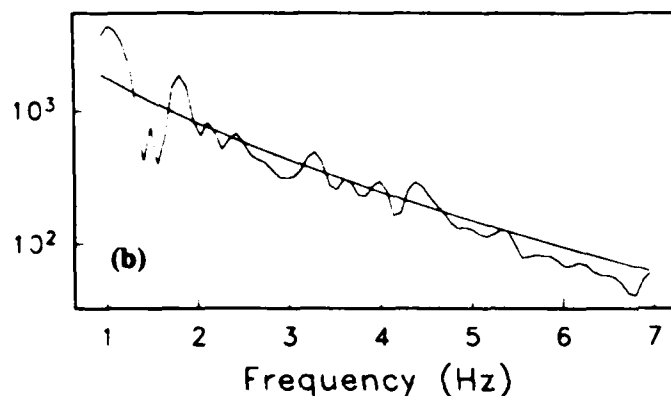
Regional Pn spectra of 152 events (Table 4.1) were inverted between 1 and 15 Hz, smoothed over a 2 Hz bandwidth, and sampled every 0.25 Hz. However, we note that at ranges less than 300-400 km, Pn and Pg arrive within the same 5s window and it is possible that some of our short range spectra include a Pg contribution. The number of data in the Pn inversion is 8664 and the number of parameters is 155. The Pn spectra were corrected for geometric spreading and inverted for seismic moment and $Q(f)$.

EARTHQUAKES

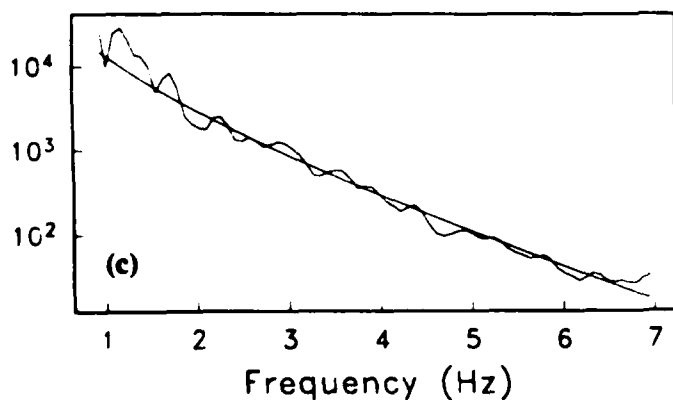
Event 186, $R = 450$ km



Event 4, $R = 600$ km

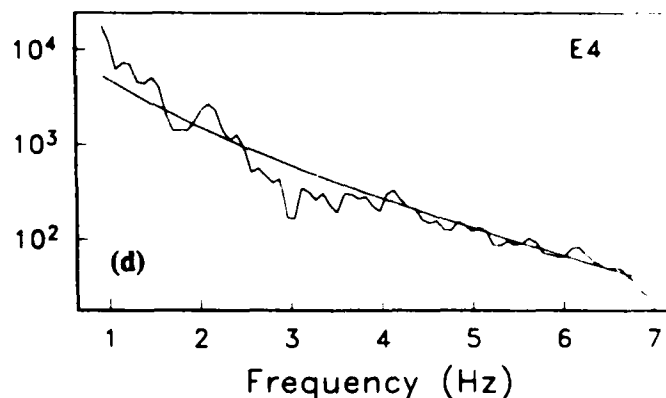


Event 64, $R = 1170$ km

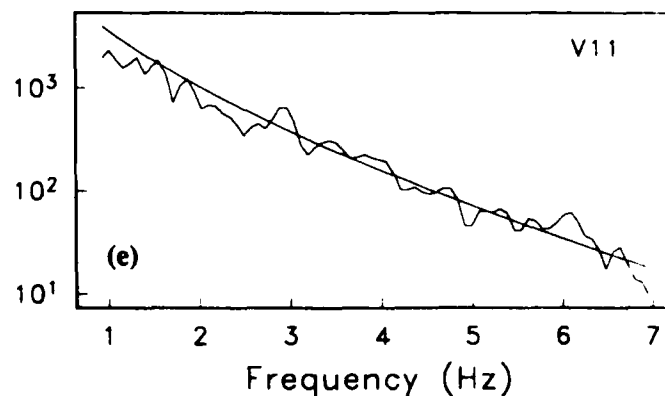


EXPLOSIONS

Event 157, $R = 890$ km



Event 30, $R = 960$ km



Event 124, $R = 1025$ km

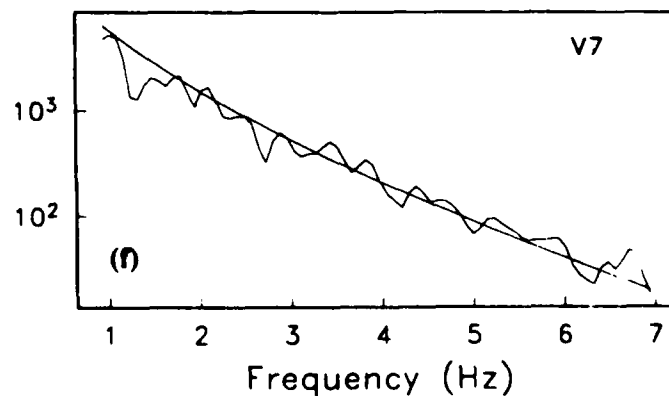


Figure 5.1. Selected comparisons of theoretical L_g spectra, based on the inversion results, to observed spectra. L_g spectra of earthquakes (events 186, 4, and 64 of Table 4.1) are on the left and L_g spectra of mine blasts (events 157, 30, and 124 of Table 4.1) are on the right. The explosion spectra are labeled by the Helsinki mine identification code (Table 4.2).

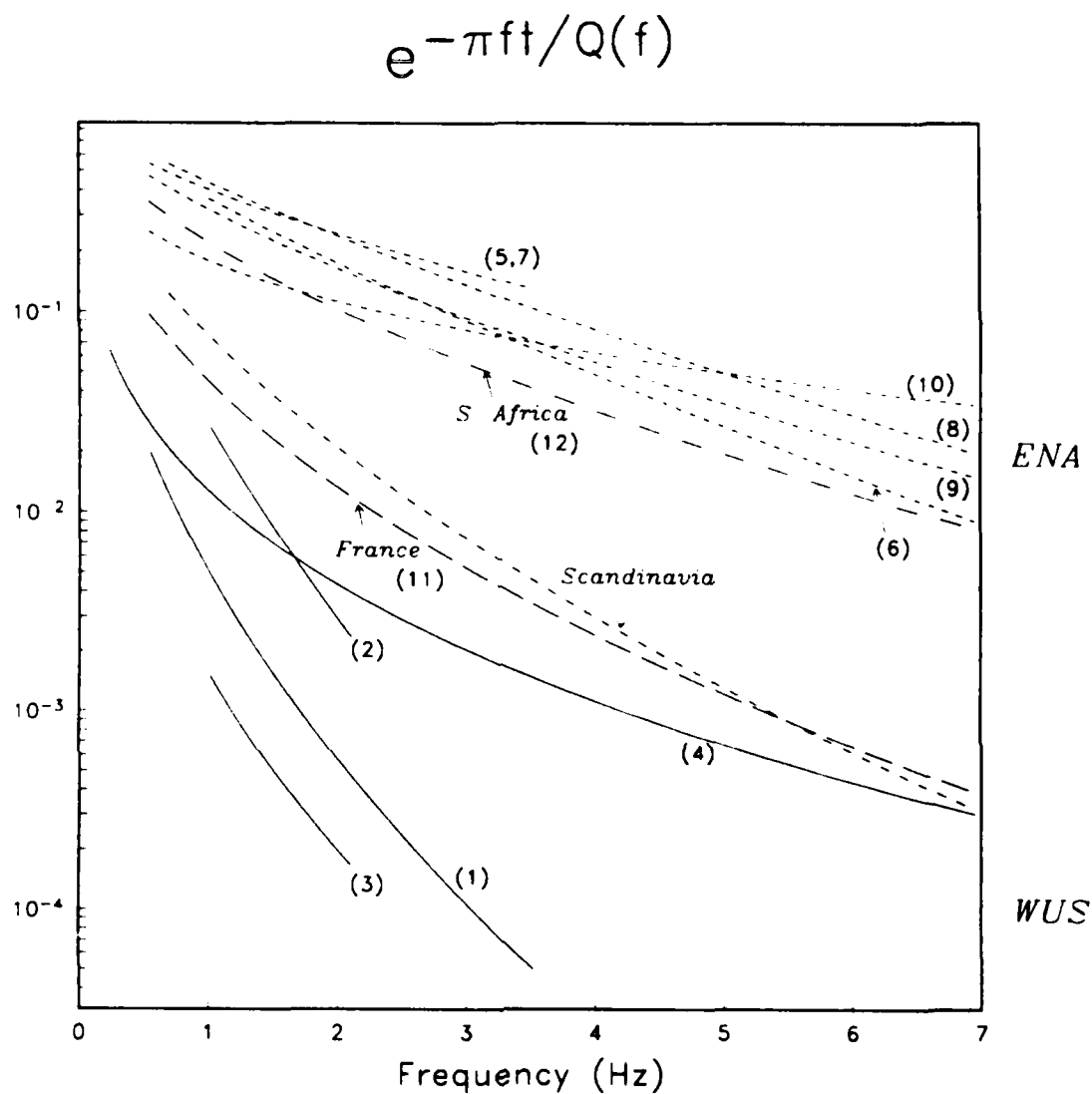


Figure 5.2. L_g spectral attenuation for the Q models listed in Table 2.1 and for our Scandinavian Q estimate. The curves are identified by their numbered entries in Table 2.1. Attenuation is plotted as $\exp(-\pi f t / Q(f))$ where the travel time t is appropriate for a range of 1000 km. Note the distinct offset between eastern North America (ENA) and western United States (WUS).

The apparent attenuation from the Pn inversion is represented by $Q(f) = 300f^{0.49}$. The corner frequency scaling parameter c derived from Pn spectra is 29.2. The inverted long period source levels for each event are tabulated in Appendix B. Selected examples of the fit of theoretical spectra to data spectra are shown in Figure 5.3. The Pn amplitude is more variable than the Lg amplitude probably due to greater sensitivity to source radiation pattern, focussing/defocussing, and scattering. Nevertheless, acceptable fits to the Pn spectra were achieved with our simple parameterization. A complete catalog of the fits to all the spectra used in the inversion can be found in Appendix B.

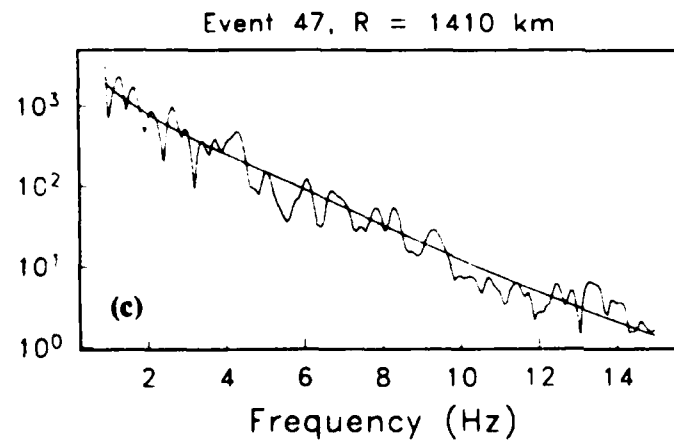
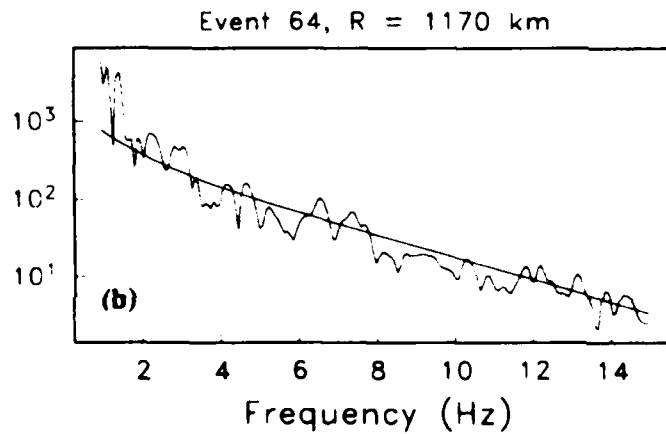
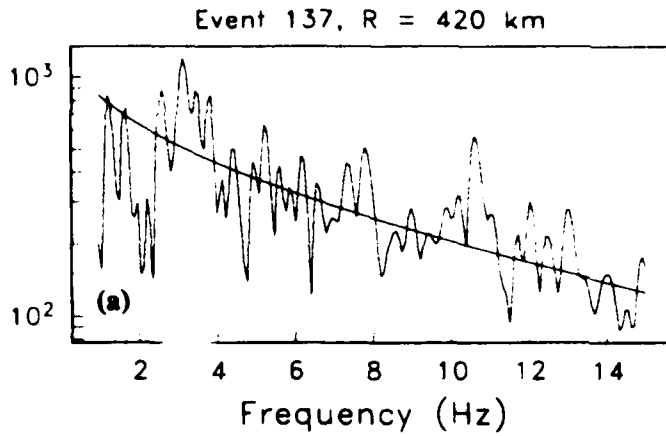
5.3 Pn/Lg consistency

An important constraint on the attenuation estimates is the consistency of the derived source parameters from the independently inverted Pn and Lg spectra. In particular, the ratio of the Lg to Pn long period source levels should be range-independent. Range dependence would indicate that geometric spreading and/or Q have been improperly modeled for one or both phases. Figure 5.4 is a plot of $S_0(Lg)/S_0(Pn)$ for the 132 events common to both inversions. Note that for explosions the ratio does not show evidence of range dependence. Examples of models that demonstrate an obvious range dependence are presented in Section 6. There is a much larger scatter in the earthquake ratios, as expected from source radiation pattern effects. Based on the explosions, the range-independent value of $S_0(Lg)/S_0(Pn)$ is approximately 0.7. Combining equations (3.1.7), (3.1.9) and (3.1.10), this implies for earthquakes and explosions of equal moment

$$\kappa \frac{\rho_s \alpha_s^3}{\rho_c \beta_c^3} \approx 0.7 \quad (5.3.1)$$

Assuming surface values of $\rho_s = 2.5 \text{ gm/cm}^3$ and $\alpha_s = 5.0 \text{ km/s}$ and average crustal values of $\rho_c = 2.7 \text{ gm/cm}^3$ and $\beta_c = 3.5 \text{ km/s}$, we have $\kappa \approx 0.26$. Simply stated, this means that the average Lg earthquake excitation is approximately 4 times the average Lg explosion excitation for sources of equal moment. We note that this is consistent with earlier studies. For example, Willis (1963), compared Lg amplitudes from an NTS explosion and a co-located earthquake at a range of 450 km and found a factor of 5 for their ratio. Pomeroy (1977) found a ratio of 3-5 for relative Lg excitation by comparing 12 earthquakes to the SALMON nuclear explosion detonated in Mississippi. However, other studies have found a less distinct separation (e.g., Murphy and Bennett, 1982; Nuttli, 1981). We will address the sensitivity of κ with respect to spreading assumptions in Section 6.3. Finally, we note in Figure 5.4 that the $S_0(Lg)/S_0(Pn)$ ratio separates many of the earthquakes from the explosions, however, there is considerable

EARTHQUAKES



EXPLOSIONS

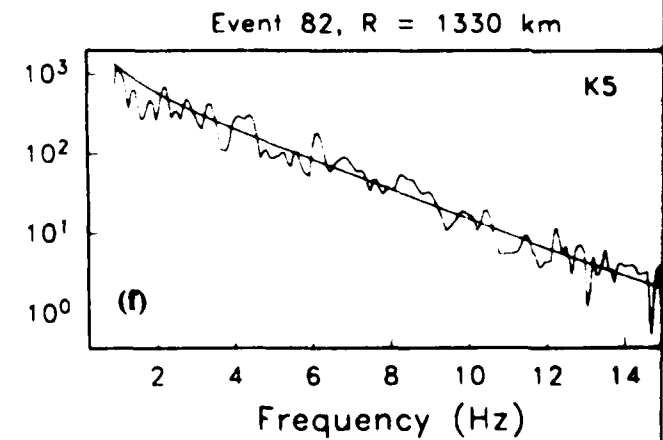
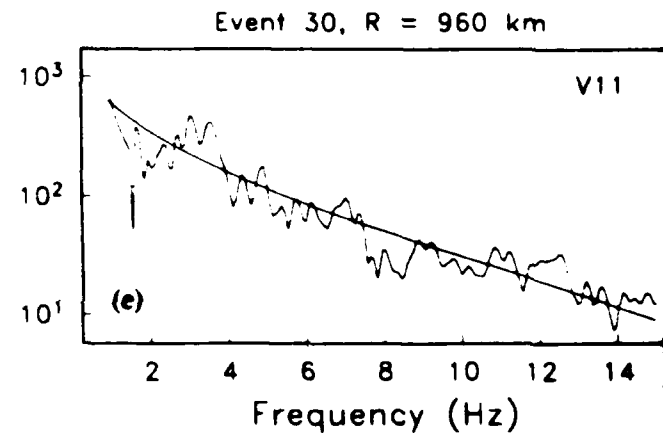
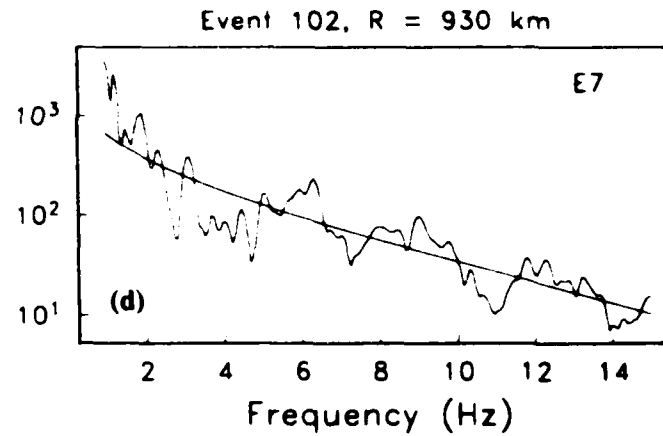


Figure 5.3. Selected comparisons of theoretical P_n spectra, based on the inversion results, to observed spectra. P_n spectra of earthquakes (events 137, 64 and 47 of Table 4.1) are on the left and P_n spectra of mine blasts (events 102, 30, and 82 of Table 4.1) are on the right. The explosion spectra are labeled by the Helsinki mine identification code (Table 4.2).

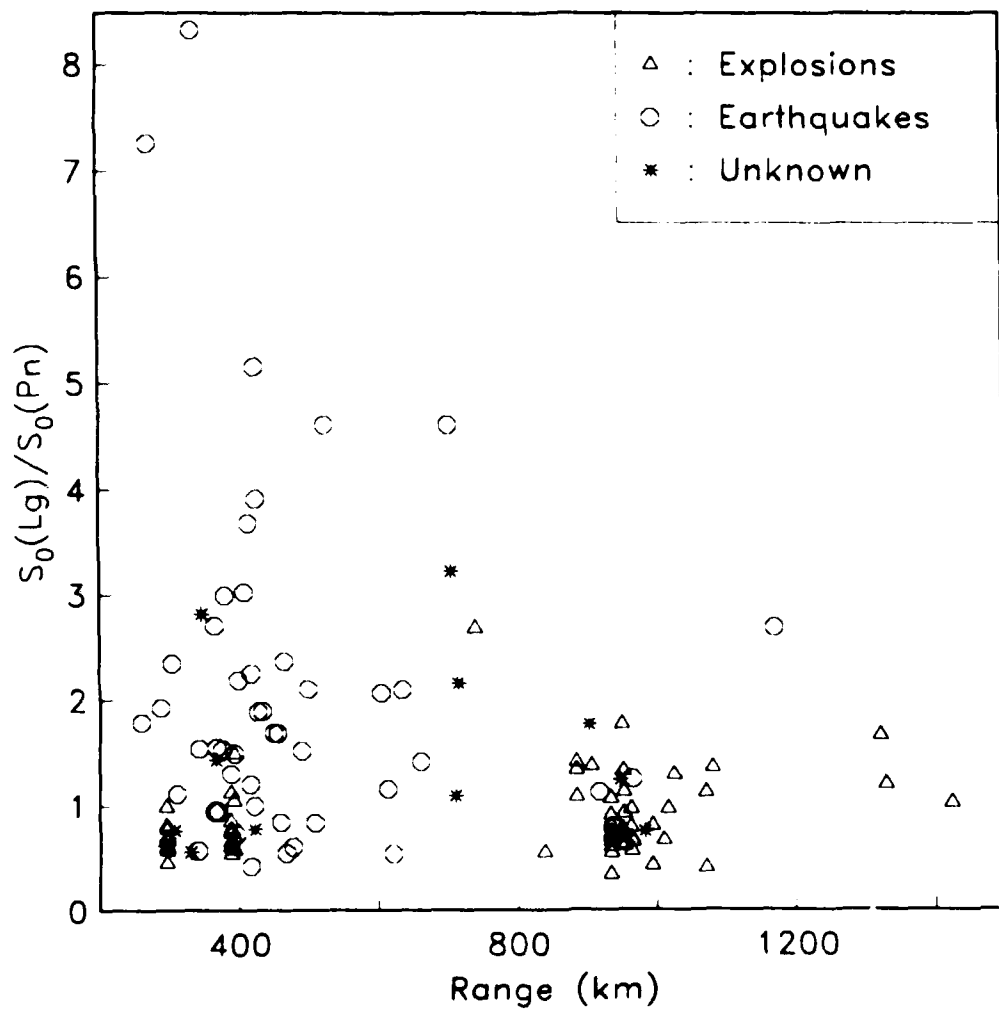


Figure 5.4. Ratio of *Lg* to *Pn* inverted long period source levels as a function of epicentral distance. Explosions, earthquakes and events of unknown source type are plotted with different symbols.

overlap between the two populations. The large ratios for some earthquakes are presumably due to the source radiation pattern for Pn .

Corner frequency is not well-constrained in the Lg inversion. Most of the events used in this study have local magnitudes less than 3.0 and correspondingly high corner frequencies. The 1-7 Hz bandwidth used in the Lg inversion was insufficient to resolve the corner frequency with much confidence. We compute the ratio of the Pn derived corner frequency to the Lg derived corner frequency from

$$\frac{f_c(Pn)}{f_c(Lg)} = \frac{c(Pn)}{c(Lg)} \left[\frac{S_0(Lg)}{S_0(Pn)} \right]^{1/3} \quad (5.3.2)$$

With $c(Pn) = 29.2$, $c(Lg) = 28.7$ and $S_0(Lg)/S_0(Pn)$ ratio of 0.7 typical for the explosions, the corner frequency ratio is 0.9, which is not significantly different from unity. We conclude that the $Q(f)$ models we have derived result in consistent source parameters for the events common to both inversions, which substantially improves confidence in the validity of the results.

5.4 Seismic moments

Seismic moment is estimated from the inversion parameter, S_0 , using equations (3.1.7) to (3.1.10). The events are at different depths and locations, so our estimates are "relative moments" in that we use the same near-source material properties for all events. The near-surface values used are $\rho_s = 2.5 \text{ gm/cm}^3$ and $\alpha_s = 5.0 \text{ km/s}$, and crustal values used are $\rho_c = 2.7 \text{ gm/cm}^3$ and $\beta_c = 3.5 \text{ km/s}$. Appendix B tabulates the estimated moments for most of the events used in the inversion. Moments were not estimated for earthquakes for which only the Pn data were inverted, or for events of unknown source type. Similarly, moments were not estimated for explosions for which only Lg data were inverted because of uncertainty in the constant, κ (3.1.10).

In Figure 5.5 we plot explosion moment versus NORESS local magnitude. The least-squares linear fits to $\text{Log}M_0$ are given by

$$Pn : \text{Log}M_0^{\text{Exp}} = 1.12 M_L + 17.6 \quad (5.4.1)$$

$$Lg : \text{Log}M_0^{\text{Exp}} = 1.16 M_L + 17.5 \quad (5.4.2)$$

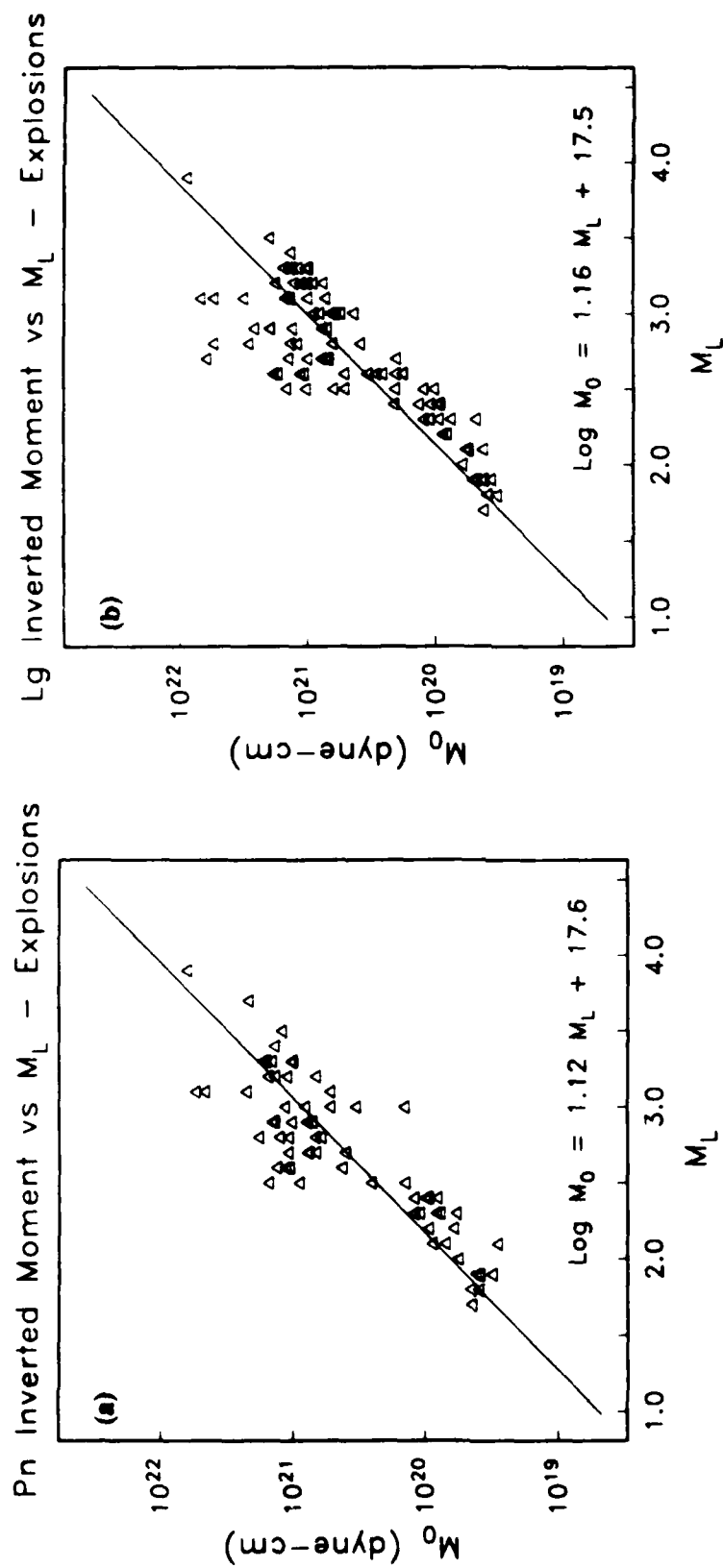


Figure 5.5. Inverted explosion moment versus NORESS local magnitude for (a) P_n (3.1.7) and (b) L_g (3.1.10) with $\kappa = 0.26$. The best fitting straight line to $\text{Log } M_0$ is shown in each figure.

For Lg , we assume $\kappa = 0.26$. The κ effects the intercept, but not the slope in (5.4.2). Our distance-corrected NORESS M_L were used because they provide a consistent magnitude measure for the data set. Events for which we do not have this M_L were not included. Comparing the two moment-magnitude relationships, the M_0^{exp} derived from Lg is equal to the M_0^{exp} from Pn when $M_L = 2.5$. This is near the center of the M_L distribution for our data set and provides further confirmation of the internal consistency of our analysis.

The earthquake moments were estimated from Lg spectra using (3.1.9) and the result is displayed in Figure 5.6. The least-squares linear fit to these data is

$$\text{Log} M_0^q = 1.04 M_L + 17.1 \quad (5.4.3)$$

Comparing (5.4.3) to (5.4.1), for equivalent moments the earthquake M_L (i.e., $\log Lg$ amplitude) is larger than the explosion M_L by 0.6 to 0.7, or a factor of 4 to 5 in Lg amplitude. Table 5.1 compares our earthquake moment-magnitude relation to results of previous studies. The Bungum, et al. (1982) study used near-field S wave spectra from the 1978 Meloy earthquake sequence in northern Norway. In general, our results for earthquake moment as a function of local magnitude are in agreement with those of similar studies and, in particular, with the result of Bungum, et al. (1982) which utilized data from the same geographic region. In that magnitude does not enter the inversion, this result lends considerable support to our derived Q model.

5.5 Corner frequency

Cube-root corner frequency scaling (3.1.6) was assumed and we inverted for the constant, c , relating corner frequency to long period source level. Appendix B tabulates corner frequencies for each event using the $c(Pn)$ and $c(Lg)$ from the inversion and the S_0 for each event. On average, our results indicate that an $M_L = 3.0$ earthquake has a corner frequency of approximately 11 Hz. Most of the events have $M_L < 3.0$ and thus have high corner frequencies. Therefore, the data do not clearly resolve source corner frequency, but we note that our results are consistent with those from similar studies. For example, Bungum, et al. (1982) expressed the corner frequency-moment relationship for the 1978 Meloy earthquake sequence in northern Norway as

$$f_c = -205 + 30.8 \text{Log} M_0 - (\text{Log} M_0)^2 \quad (5.5.1)$$

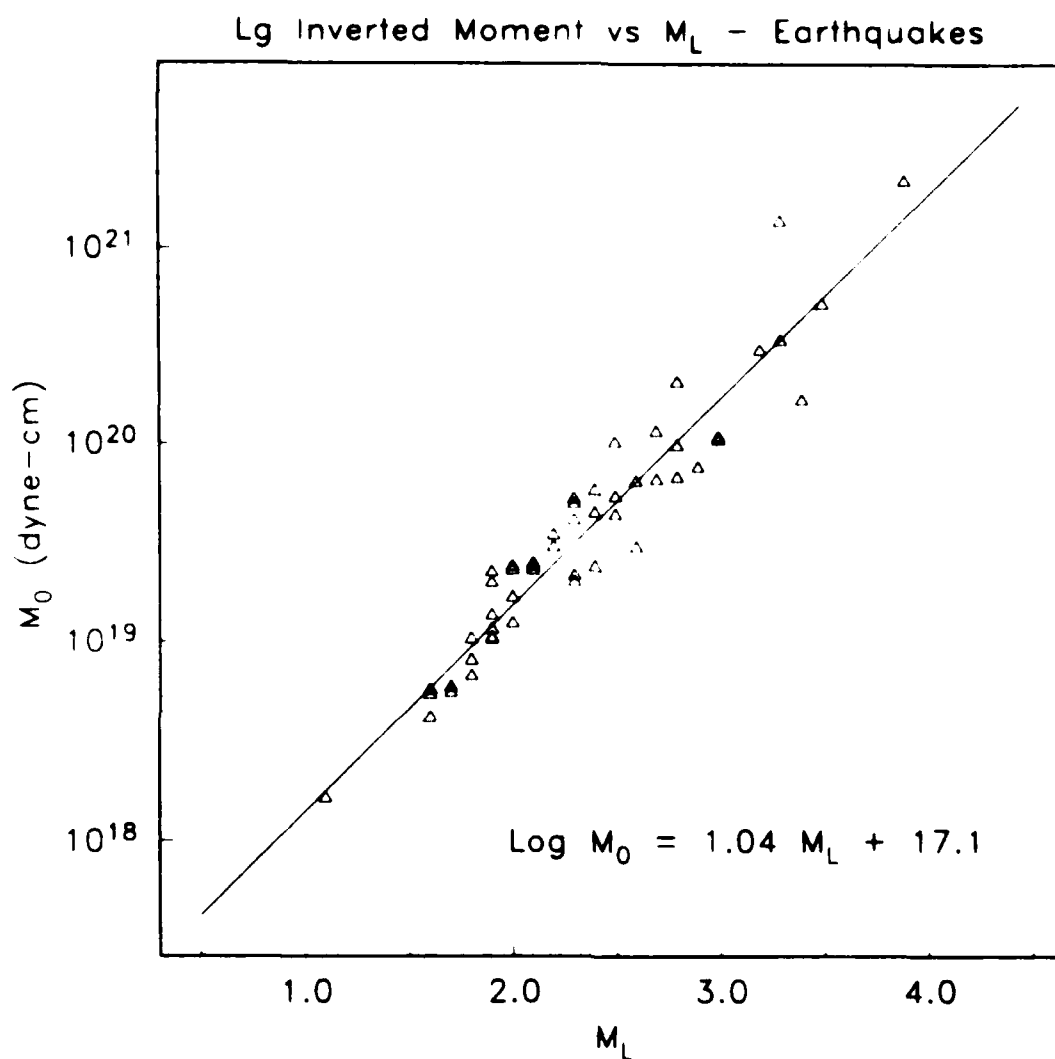


Figure 5.6. Inverted earthquake moment versus NORESS local magnitude for Lg (3.1.9). The solid line is the best-fitting straight line to $\text{Log } M_0$.

Table 5.1. Moment-magnitude relations.

M_L	ρ (gm/cm ³)	β (km/s)	$\text{Log}M_0$	Distance	Reference
-0.4 - 2.2	2.7	3.5	$0.90M_L + 17.5$	near-field	Bungum, et al. (1982)
1.0 - 3.5	2.7	3.5	$1.01M_L + 16.7^\dagger$	near-field	Mueller and Cranswick (1985)
2.1 - 4.3	2.8	3.8	$1.18M_L + 16.6^\dagger$	regional	Shin and Herrmann (1987)
1.0 - 4.2	2.8	3.8	$0.94M_L + 17.32$	regional	Hasegawa (1983)
1.8 - 4.9	2.5	3.5	$1.26M_L + 16.44$	< 200 km	Dwyer, et al. (1983)
1.1 - 3.8	2.7	3.5	$1.04M_L + 17.1$	regional	Sereno, et al. (this study)

[†] We estimated the regression coefficients from tabulated moments and magnitudes.

Adopting their moment-magnitude relation (Table 5.1), this gives a corner frequency of 9 Hz for an $M_L = 3.0$ event. Similarly, assuming cube-root scaling, a least-squares fit to the Miramichi aftershock corner frequencies derived by Mueller and Cranswick (1985) gives a corner frequency of 12 Hz for an $M_L = 3.0$ earthquake. In general, the corner frequencies derived in this study are within a few Hertz of the near-field estimates.

6. ERROR ANALYSIS

The separate *Pn* and *Lg* inversions are each characterized by a broad minimum in the data residuals, and therefore a range of models that fit the data equally well. In Section 5 we described our "preferred model" and in this section we define the range of acceptable models and the basis upon which our selection was made. The following list summarizes the selection process.

- (1) Identify the full range of parameter trade-offs for each phase. For fixed source and spreading assumptions, the separate *Pn* and *Lg* inversions identify the range of *Q* models that produce essentially the same data variance.
- (2) Select *Pn* and *Lg* models that give consistent source parameters for the events common to both inversions. That is, constrain $S_0(Lg)/S_0(Pn)$ to be range-independent. This reduces the acceptable solutions to a set of model pairs. That is, for a fixed *Lg Q* model, tight bounds are placed on acceptable *Pn Q* models. From the range-independent value of the source level ratio, estimate the relative *Lg* excitation of earthquakes and explosions.
- (3) Analyze the trade-off between data variance and M_0 - M_L variance. It was found that models which reduced the data variance increased the variance of the M_0 - M_L relation. By excluding models that increase either variance without significant decrease in the other, we define the range of acceptable model pairs. The "preferred model" (for fixed source and spreading assumptions) is selected from the mid-range of the acceptable model pairs.
- (4) Change source assumptions. It was found that our results were not strongly dependent upon the details of our source assumptions because of the high corner frequencies for most of the events.
- (5) Change spreading assumptions. We fix *Lg* spreading (which is well-constrained theoretically and empirically) and change the *Pn* spreading rate. The new set of *Pn Q* models are input to steps (2) and (3) above to define acceptable models for this *Pn* spreading rate. Next, compare the *Lg* earthquake-explosion ratio to the results of other studies to bound the *Pn* spreading rate.

We present in Section 6.1 the formal inversion errors in the form of a parameter covariance matrix. However, we note that the relatively small formal errors obtained do not reflect the true uncertainty in our parameter estimates. In Section 6.2 we discuss the trade-offs among model parameters for the fixed spreading and source assumptions used in Section 5. The consequences of changing these assumptions are explored in Section 6.3. Section 6.4 describes observed systematic variations in source moment versus Lg amplitude for different mines. Section 6.5 presents examples of data that were not well-modeled by the inversion results.

6.1 Formal inversion errors

The variance of the inversion is defined as the sum of the squared data residuals divided by the number of data (nd) minus the number of parameters (np). That is

$$\sigma_d^2 = \frac{1}{nd-np} \sum_{i=1}^{nd} (d_i - d_i^h)^2 \quad (6.1.1)$$

In this case, the data are log amplitudes corrected for geometric spreading. Figure 6.1 displays the Pn and Lg spectra for a magnitude 3.3 German earthquake at a range of 1170 km. Superimposed are theoretical spectra for the model presented in Section 5 bounded by single standard deviation curves (σ_d). The variance of the Pn inversion is approximately 0.06 and the Lg variance is approximately 0.03. Note that σ_d^2 is the variance of the smoothed spectra and is therefore lower than the true data variance.

Formal error estimates on the individual inversion parameters are obtained from the parameter covariance matrix. For the least-squares solution, (3.1.24), the parameter covariance matrix is

$$K_m = \sigma_d^2 (A^T A)^{-1} \quad (6.1.2)$$

The parameter covariance matrix for the damped least-squares solution, (3.1.25), is

$$K_m = \sigma_d^2 (A^T A + \lambda I)^{-1} A^T A (A^T A + \lambda I)^{-1} \quad (6.1.3)$$

The Lg Q model presented in Section 5 had $Q_0 = 349$ with a formal inversion error of ± 8 and $\eta = 0.408 \pm 0.008$. The Pn Q model had $Q_0 = 301 \pm 9$ and $\eta = 0.486 \pm 0.010$. The corner frequency parameters are $c(Pn) = 29.24 \pm 0.04$ and $c(Lg) = 28.66 \pm 0.05$. The artificially small formal errors on c are a consequence of the poor resolution of this parameter. That is, damping has decreased the variance of the parameter estimate with an associated decrease in its resolution. The variance of the individual S_0 estimates increase with increasing

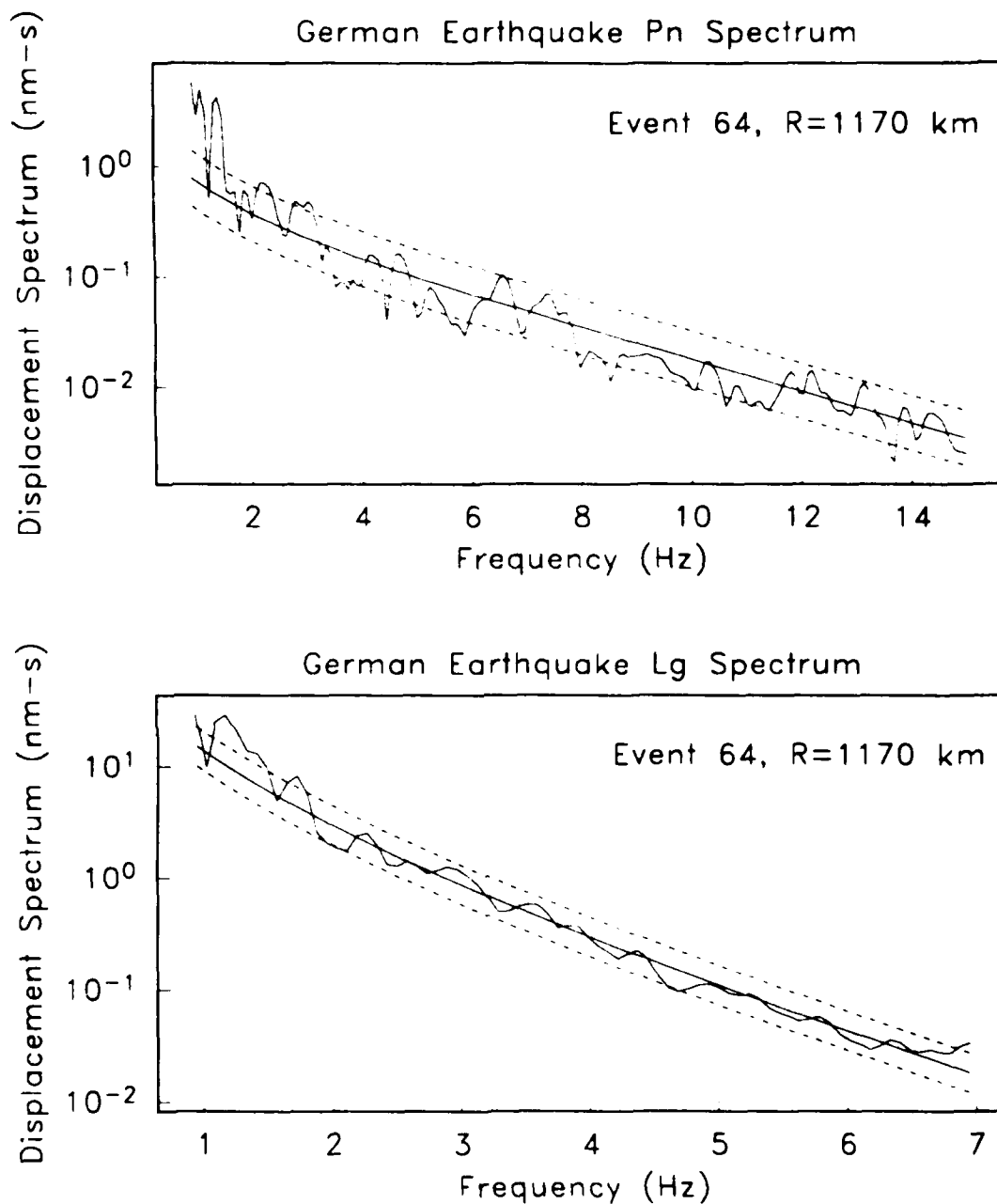


Figure 6.1. *Pn* and *Lg* spectra of a German earthquake (event 64 of Table 4.1) at a distance of 1170 km from NORESS. The solid curves superimposed on the observed spectra are the theoretical *Pn* and *Lg* spectra for this event based on the inversion results. The dashed lines indicate one standard deviation, σ_d .

epicentral distance but, on the average, the S_0 standard deviations were of the order of 10%. The standard errors of the explosion moment-magnitude relations are $\text{Log}M_0 = 1.12(\pm 0.08)M_L + 17.6(\pm 0.2)$ for Pn and $\text{Log}M_0 = 1.16(\pm 0.08)M_L + 17.5(\pm 0.2)$ for Lg . The Lg earthquake moment-magnitude relation is $\text{Log}M_0 = 1.04(\pm 0.04)M_L + 17.1(\pm 0.1)$. These errors must be taken into account in analyzing the predictability of regional wave spectra of events of a given magnitude (Section 7). The single standard deviation curves in Figure 6.1 reflect only the estimated uncertainty in the spectral estimate for fixed moment, and do not include the scatter in the moment-magnitude relationship.

6.2 Parameter trade-off

In this section, we discuss the tradeoffs among M_0 , Q_0 , η , and c for fixed source and spreading assumptions. The effect of varying the source and spreading assumptions will be discussed in the next section. The low frequency spectral level depends on M_0 and Q_0 . When M_0 increases, Q_0 decreases within a range of models that preserve the fit to the long period spectral level and slope. In response to the high frequency spectrum, when Q_0 decreases, η increases. The corner frequency scaling parameter c is constrained by a few large events, and increases in the estimates for M_0 cause an increase in c to retain approximately the same corner frequency for these events. These trade-offs are illustrated in Table 6.1 with 6 models (Q_0 varying between 300 and 427) obtained from the Lg inversion that have data variances that differ by less than 5%.

The trade-offs in the Pn results are illustrated in Table 6.2 with 7 Pn models that have data variances within 13%. All were done with the $r^{-1.3}$ spreading assumption. If the Q model for Lg is fixed then the requirement that $S_0(Lg)/S_0(Pn)$ be range-independent places tight bounds on acceptable Pn Q models. For example, in Figure 6.2 we plot this ratio for Lg $Q_0 = 350$ and three Pn models with $Q_0 = 401, 300$, and 201 . Only explosions were included in this figure because the earthquake ratio is contaminated by unknown Pn radiation pattern effects. The ratios for the $Q_0 = 401$ and 201 models display a clear range dependence. Thus, if Lg Q_0 is 350, then the corresponding choice for Pn Q_0 is 300 and these are the models used in Section 5.

For other choices of Lg Q_0 , other Pn Q models are consistent with a range-independent S_0 ratio. In particular, Lg $Q_0 = 400$ suggests Pn $Q_0 \approx 375$ and Lg $Q_0 = 300$ suggests Pn $Q_0 \approx 250$. There is no obvious basis for choosing among the model pairs. However, there is a trade-off between data variance and variance of the moment-magnitude relation. Figure 6.3

Table 6.1. Lg parameter trade-off

Model Index	Q_0	η	c	$\text{Log}M_o^{\text{exp}} (\kappa = 0.26)$	$\text{Log}M_o^{\text{eq}}$	σ_d^2
1	427	0.34	19.1	$1.04M_L + 17.65$	$1.03M_L + 17.03$	0.0320
2	396	0.37	22.6	$1.09M_L + 17.60$	$1.03M_L + 17.06$	0.0315
3	374	0.38	25.3	$1.12M_L + 17.56$	$1.04M_L + 17.08$	0.0312
4†	350	0.41	28.7	$1.16M_L + 17.51$	$1.04M_L + 17.10$	0.0310
5	325	0.43	33.0	$1.21M_L + 17.46$	$1.05M_L + 17.13$	0.0307
6	300	0.46	39.0	$1.27M_L + 17.40$	$1.06M_L + 17.16$	0.0305

† The model discussed in Section 5.

Table 6.2. Pn parameter trade-off

Model Index	Q_0	η	c	$\text{Log}M_o^{\text{exp}}$	σ_d^2
1	498	0.39	16.0	$0.99M_L + 17.63$	0.0703
2	401	0.43	20.8	$1.04M_L + 17.63$	0.0667
3	373	0.44	22.8	$1.05M_L + 17.62$	0.0657
4	356	0.45	23.3	$1.07M_L + 17.61$	0.0653
5†	300	0.49	29.2	$1.12M_L + 17.57$	0.0637
6	248	0.53	36.6	$1.19M_L + 17.52$	0.0625
7	201	0.57	48.8	$1.29M_L + 17.43$	0.0614

† The model discussed in Section 5.

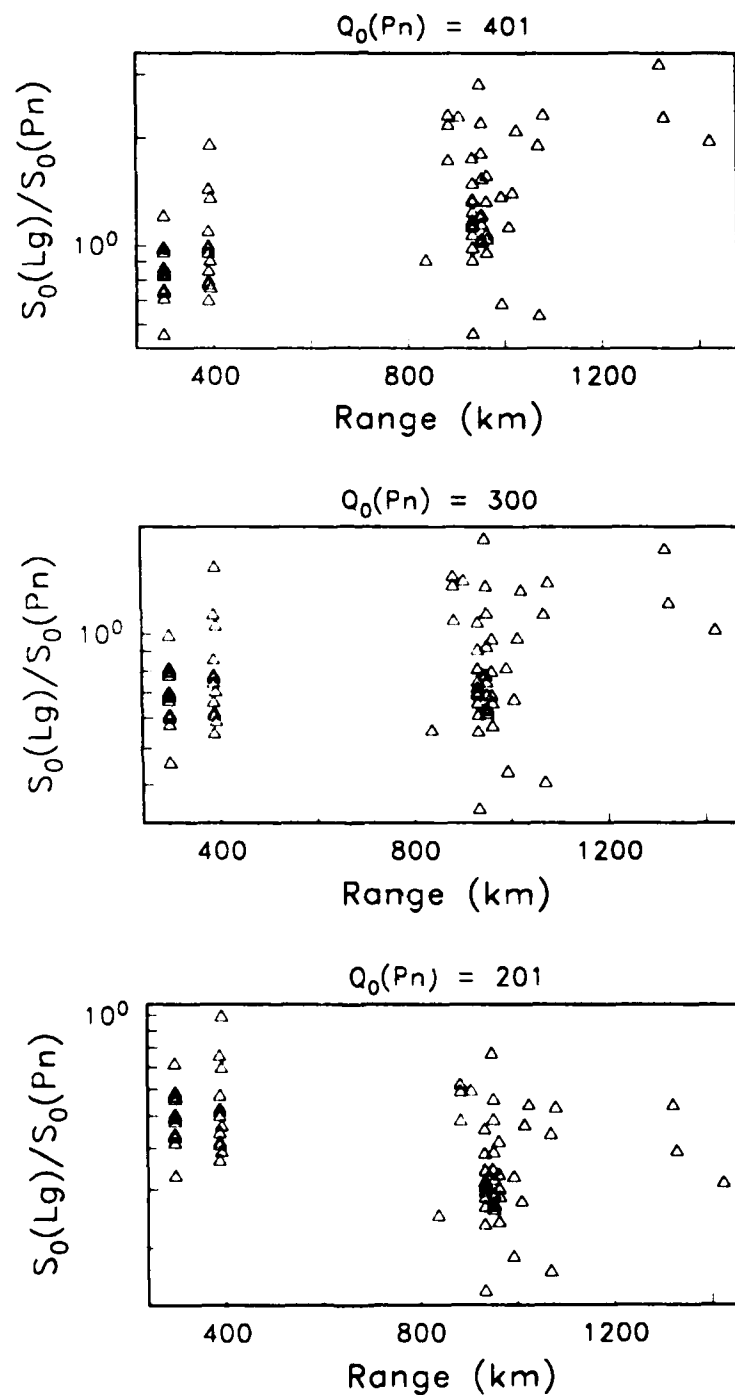


Figure 6.2. Ratio of *Lg* to *Pn* inverted long period explosion source levels as a function of epicentral distance. *Lg* Q_0 is fixed for all 3 plots at 350 (#4 of Table 6.1). *Pn* Q_0 is varied from 401 to 201 (numbers 2, 5, and 7 of Table 6.2).

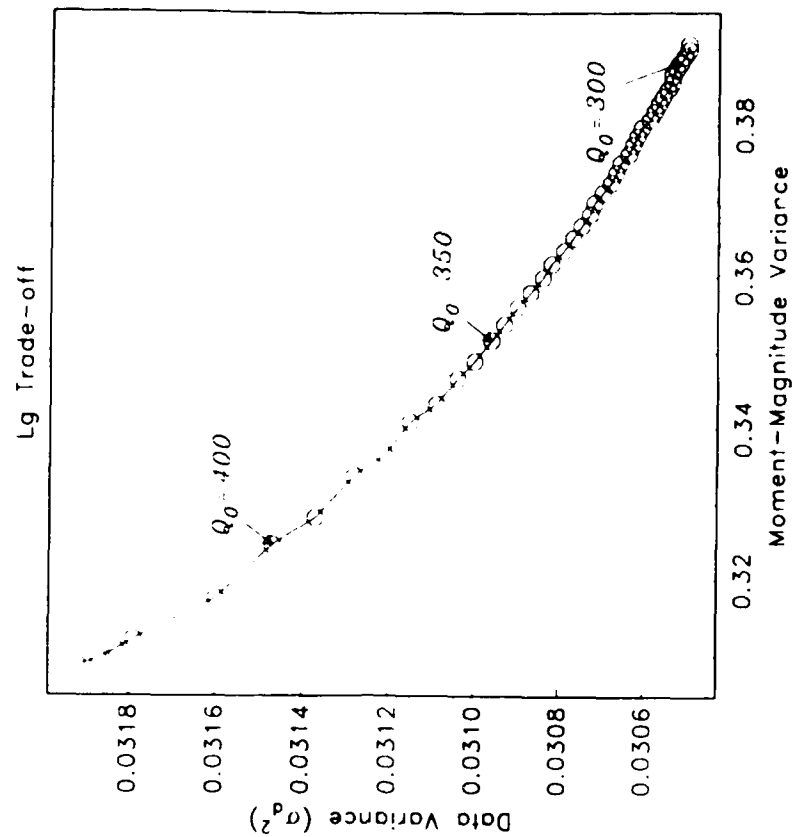
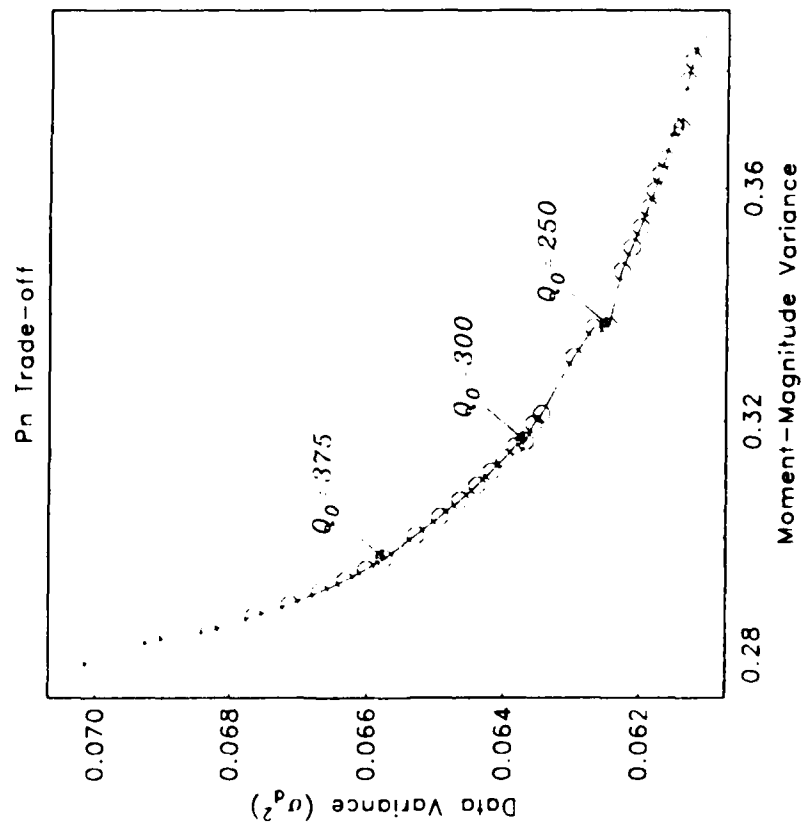


Figure 6.3. Trade-off between data variance (σ_d^2) and variance of the moment-magnitude relation for (a) P_n and (b) L_g . Symbols define models for different iterations of the inversion. Three of the models are identified in each plot by their Q_0 values. For L_g these are models 2, 4, and 6 of Table 6.1 and for P_n they are models 3, 5, and 6 of Table 6.2.

plots this trade-off for the range of models defined in Tables 6.1 and 6.2. The figure demonstrates that the lower Q models reduce the data variance but result in increased scatter in the moment-magnitude relationship. On the other hand, the higher Q models reduce the M_0 - M_L variance but increase the data variance.

From Figure 6.3, we note that models with $Pn\ Q_0 > 375$ cause a rapid increase in data variance with only a slight reduction in M_0 - M_L variance. Also, models with $Pn\ Q_0 < 250$ increase the M_0 - M_L variance without reduction in data variance. We therefore define the range of acceptable $Pn\ Q$ models as $Q_0(Pn) = 250$ -375 with η between 0.53 and 0.44. Therefore, the range-independence of the source level ratios requires the range of acceptable $Lg\ Q$ models to be $Q_0(Lg) = 300$ -400 with η between 0.46 and 0.37. These, of course, cannot be chosen in any combination. For a fixed $Lg\ Q$ model, a tight bound on $Pn\ Q$ is placed by the range-independence of the Lg to Pn source level ratio. From the mid-range of acceptable models, we selected the $Lg\ Q_0 = 350$ and $Pn\ Q_0 = 300$ model pair as our "preferred model" to present in Section 5.

6.3 Result dependence on parameterization

In Section 6.2, we discussed the parameter trade-off for a fixed set of source and geometric spreading assumptions. In this section, we analyze the dependence of our results on these assumptions.

6.3.1 Source parameterization

All of the results of this study were obtained by assuming an ω^2 source function with cube-root corner frequency scaling. However, most of the events considered have local magnitudes less than 3.0, so the corner frequencies are near or beyond the upper end of the frequency band inverted. The results are therefore not very sensitive to our source parameterization.

All of the results discussed previously were obtained assuming the simplified Mueller-Murphy (1971) explosion source function (3.1.4) with cube-root corner frequency scaling (3.1.6). We also inverted the Lg data assuming the Brune (1970, 1971) earthquake source model (3.1.5) with cube-root corner frequency scaling. For the same Q_0 , the Brune source model leads to Q with stronger frequency dependence. For example, when $Lg\ Q_0$ is 350, η is 0.41 for the Mueller-Murphy model and 0.48 for the Brune model. The reason for this slight difference is that the Brune model has a less abrupt corner frequency (Figure 3.1), and the reduced high frequency source contribution is compensated for by a higher Q at high frequency. The Brune

model inversions give a data variance that is 2% greater than that obtained with the Mueller-Murphy model.

If we assume a flat source (no corner frequency), the results are nearly the same as those from the Mueller-Murphy (1971) model, with a slight increase in the data variance. This merely indicates that the corner frequencies of most of the events are greater than 7 Hz. We have not explored other alternative source models, but this result indicates that our *Lg* attenuation results are not sensitive to the details of the source parameterization.

The *Pn* inversion is more sensitive to source parameterization than the *Lg* inversion as a result of both radiation pattern and the increased bandwidth. We used the Mueller-Murphy (1971) model for all *Pn* inversions. We have not run the *Pn* inversion with the Brune (1970, 1971) earthquake source function, although we would expect a response similar to that observed for *Lg*. That is, a slight increase in the frequency dependence of *Q* to compensate for the reduced high frequency source contribution. We have not analyzed the sensitivity of our estimate with respect to high frequency source falloff, but it is clear that an increase in *Q* must accompany an increased source spectral decay to preserve the fit at high frequency. Our results for *Pn* must therefore be considered relative to an ω^2 source.

6.3.2 Geometric spreading

The geometric spreading rate for *Lg* is well-constrained both empirically and theoretically, and our assumptions are described in Section 3.1. All of the data used in this study are at ranges greater than 100 km. Therefore, r_0 (in 3.1.2) trades off directly with inverted moment and has no effect on the $Q_{Lg}(f)$ estimate.

The geometric spreading rate of *Pn* is much more difficult to estimate with confidence. Results presented earlier were obtained by assuming $r^{-1.3}$ *Pn* spreading. In this section, we examine the results for alternatives, in particular r^{-1} (spherical spreading) and $r^{-1.5}$ were used. Table 6.3 describes the resulting *Pn* models, all required to give a range-independent $S_0(Lg)/S_0(Pn)$ ratio for the *Lg* *Q* model of Section 5 (#4 in Table 6.1). As the *Pn* spreading rate increases, $Q_0(Pn)$ increases, η decreases, and M_0 increases. The range-independent value of the long period source level ratio can be used to extract the relative *Lg* excitation of explosions and earthquakes (5.3.1). The κ in Table 6.3 indicates the relative excitation of *Lg* for explosions and earthquakes. Note that assuming r^{-1} *Pn* spreading results in greater *Lg* excitation for explosions than for earthquakes of equal moment ($\kappa > 1$). This contradicts empirical

Table 6.3. Pn parameter trade-off as a function of spreading rate

Spreading Rate	Q_0	η	c	$\text{Log}M_o^{\text{exp}}$	κ	σ_d^2
r^{-1}	246	0.53	18.6	$1.09M_L + 16.95$	1.11	0.0623
$r^{-1.3}$	300	0.49	29.2	$1.12M_L + 17.57$	0.26	0.0637
$r^{-1.5}$	352	0.45	68.3	$1.14M_L + 17.99$	0.09	0.0651

observations and so argues for a Pn spreading rate greater than r^{-1} . On the other hand, a Pn spreading rate of $r^{-1.5}$ gives $\kappa = 0.09$, or 11 times greater Lg for earthquakes than explosions. This is much too large a difference. The earthquake Lg excitation for $r^{-1.3}$ Pn spreading is 4 times the explosion excitation, consistent with the observations of Willis (1963) and Pomeroy (1977). This is also a result consistent with theoretical simulations of Pn propagation in realistic earth models (Wallace, personal communication).

6.4 Systematic variations in source moment versus Lg amplitude

We have not accounted for any azimuthal variations in Q , but have combined data from all azimuths into an inversion for a single, average Q model. Examination of the fit of the model to the data (Appendix B) demonstrates the validity of this procedure. However we do note some systematic variations in the Lg amplitude (represented by M_L) for fixed moment obtained from the inversion. In particular, in the M_0 - M_L data in Figure 5.5 there is a set of explosions with lower magnitudes for fixed moment than is indicated by the general trend of the data. These are explosions from mines K1-K12 at azimuths between 34° and 46° and from mines V1-V13 at azimuths between 57° and 84° (Figure 4.3). The neighboring mines, E1-E9 between 91° and 97° , are, however, consistent with the general trend. Figure 6.4 displays the Lg explosion moments versus magnitude for the V mines, K mines, and E mines along with the curve described by (5.4.2). In general, events from the V and K mines have smaller Lg amplitudes for a given moment than events from E mines. Figure 6.5 compares NORESS vertical component recordings of an E7 mine blast to recordings of a V8 mine blast. Both events have NORESS magnitudes of 3.3. The disparate Pn/Lg ratios for the two events indicates that either Lg propagation is structurally inhibited north of E7 or that different mining practices result in distinctly different Pn to Lg excitation ratios. If Lg propagation is structurally inhibited, in must be a broad band blockage because spectra from V8 and E7 mines are consistent with the same Q model (Appendix B).

6.5 Anomalous events

Appendix A lists events that were processed but not included in the inversion. Most of those were excluded because of low signal to noise ratios, signals from multiple events were mixed, or they had uncertain locations due to ambiguous phase association. Also, there were 11 events that occurred within a 24 hour time period off the southwest coast of Norway that were not included because their spectra were inconsistent with those from events at similar distances. The event epicenters are plotted in Figure A.1 (events 15-23 and 25-26 of Table A.1). We are not certain whether these are off-shore earthquakes or underwater explosions (Henson and Bache, 1986). Figure 6.6 is a comparison of Lg spectra for a Titania mine blast and of one of

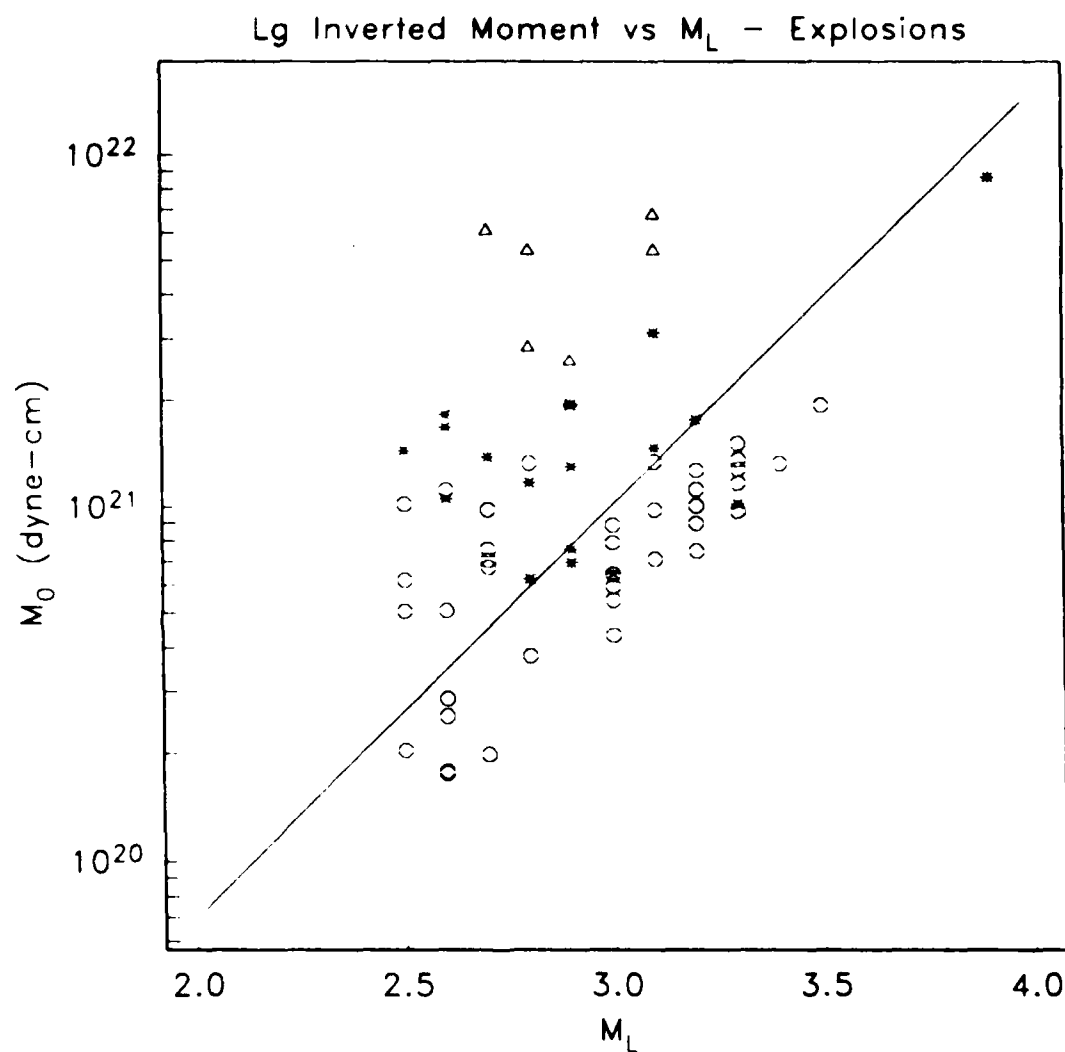
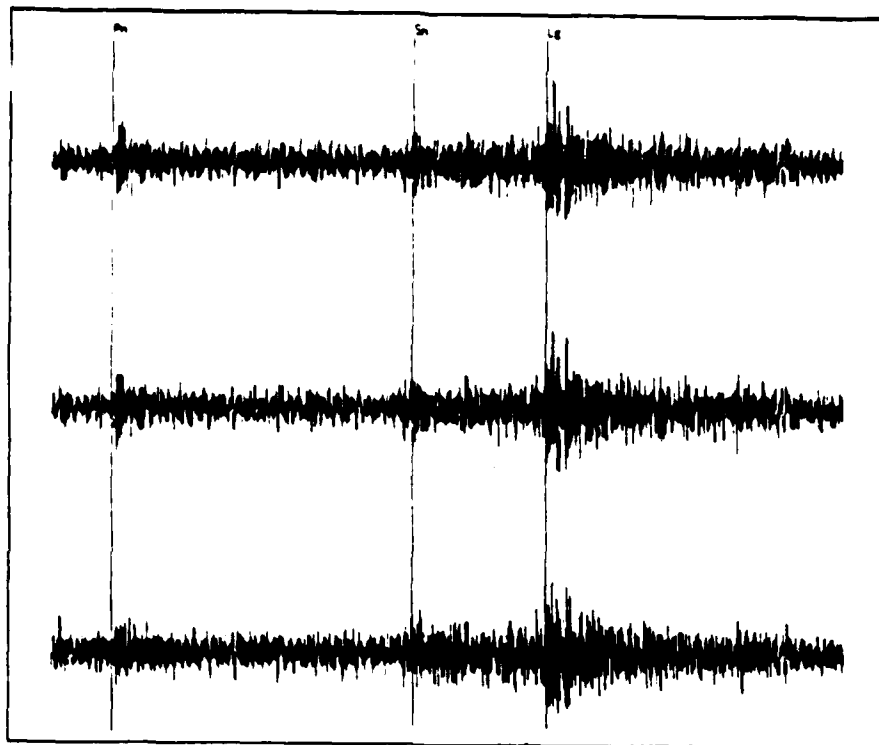


Figure 6.4. Lg inverted explosion moment versus NORESS local magnitude for model 4 of Table 6.1. Only explosions from K, V, and E mines (Table 4.2) are included. The triangles are K-mine explosions, asterisks are V-mine explosions, and circles are E-mine explosions. The line is the $\text{Log}M_0$ -magnitude relation derived using all of the explosions in the data set (5.4.2).

Mine Blast - E7



Mine Blast - V8

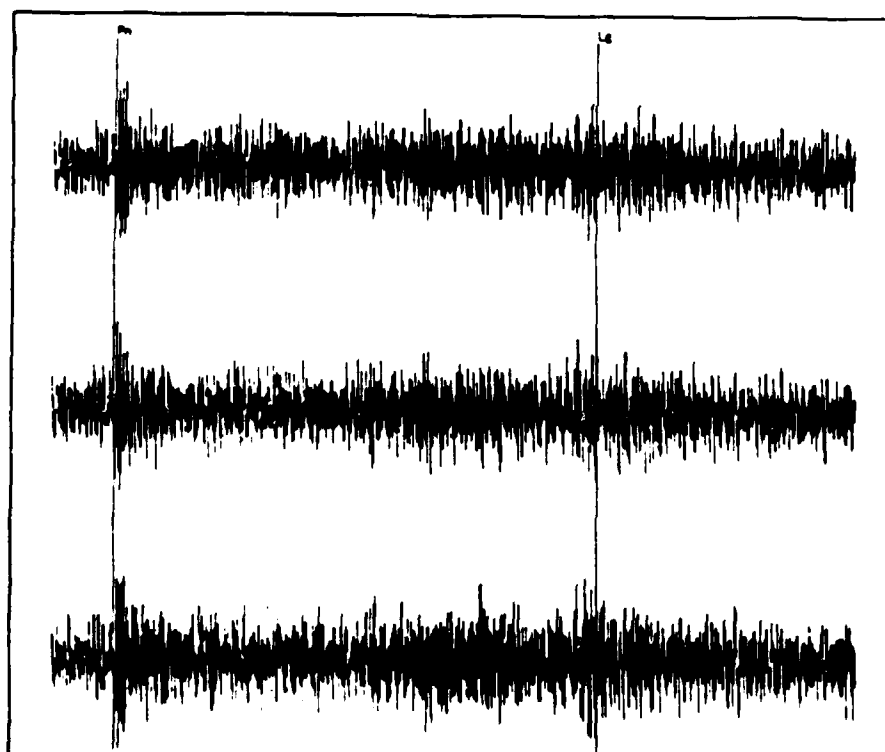


Figure 6.5. Vertical component seismograms of E7 (event 98, Table 4.1) and V8 (event 69, Table 4.1) mine blasts. Detections and phase associations for each event are indicated. The V8 mine is only 60 km further from NORESS than E7, yet the two records have distinctly different Lg to Pn ratios.

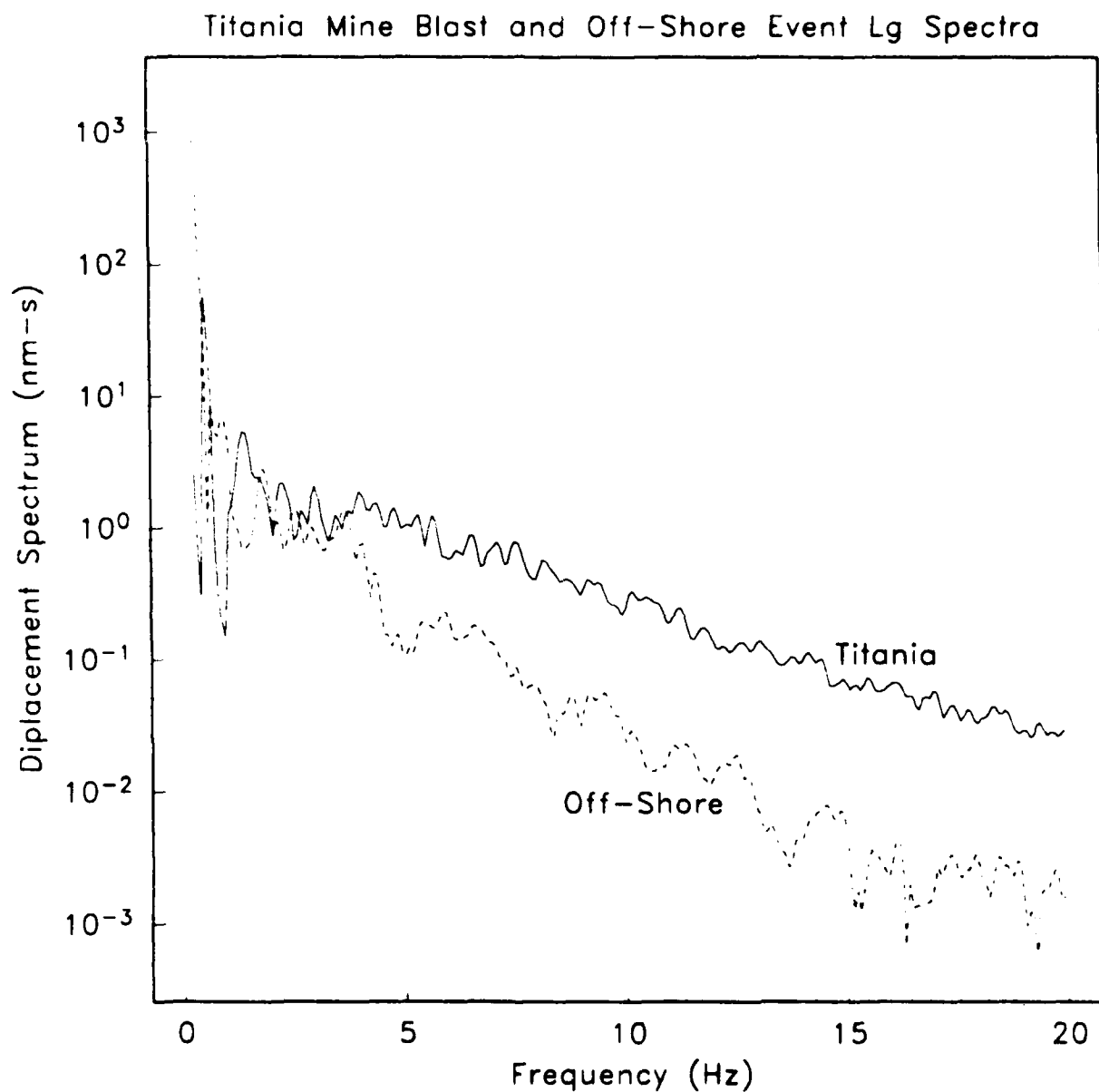


Figure 6.6. Comparison of *Lg* spectra of a Titania mine blast (event 63, Table 4.1) and an off-shore event (event 20, Table A.1). The off-shore event is at approximately the same azimuth and only 80 km further from NORESS than the Titania mine.

the off-shore events. The increased high frequency decay of the off-shore event spectrum cannot be accounted for by the different path lengths. The Pn spectra of the two events have a similar relationship. There are several possible explanations for the difference between the spectra. If the off-shore events are explosions, their high frequency energy could be depleted by near-source sediment resonance. One might also speculate that the difference is caused by some structural feature between the off-shore events and the coast of Norway. However, we note that events 66 and 97 of Table 4.1 are off-shore southwest Norway events that have spectra that are consistent with the Titania mine blast spectra (Appendix B). This suggests that the difference is either from source differences or near-source structure.

7. SIMULATION OF REGIONAL Pn AND Lg SPECTRA

We have developed an accurate parameterization of the observed spectra of regional events recorded at NORESS in terms of familiar seismological parameters characterizing the source and range dependence of these spectra. Using these parameters we can "predict" the spectra for a chosen source and range and be confident that it is correct with well-defined uncertainty of our parameters. Our confidence, of course, degrades if we choose a source or range outside the bounds of our experience; that is, if we attempt to extrapolate our results to situations not yet encountered.

Figure 7.1 displays predicted range-dependent Pn spectra, using the inversion results of Section 5, for a magnitude 3.0 explosion. The relevant parameters are $Q(f) = 300f^{0.49}$, $M_0 = 8.6 \times 10^{20}$ dyne-cm ($S_0 = 21.9$), $f_c = 10.4$ Hz, and a Pn spreading rate of $r^{-1.3}$. Note that these results do not depend on resolving the parameter trade-offs; all of the models identified in Section 6 will give similar predictions. Also shown is the average NORESS noise estimated from samples taken prior to Pn for many events (Henson and Bache, 1986). The Pn spectra approximately parallel the noise curve at a distance of 400-500 km, converging with it at longer ranges and diverging from it at shorter ranges. This observation is supported by average spectral density curves constructed by Ringdal, et al. (1986) using the high frequency element of the NORESS array. Figure 7.2 is the corresponding plot for Lg . The Lg parameters are $Q(f) = 350f^{0.41}$, $M_0 = 9.8 \times 10^{20}$ dyne-cm ($S_0 = 20.7$), $f_c = 10.4$ Hz, and cylindrical spreading with $r_0 = 100$ km. The Lg spectrum reaches the noise level at a much lower frequency than the Pn spectrum, while at long periods the Lg amplitude exceeds the Pn amplitude by as much as a factor of 10. This indicates that these regional seismograms are characterized by Lg the largest amplitude phase and Pn having a higher dominant frequency.

The largest uncertainty in the "predicted" spectra in Figures 7.1 and 7.2 is the absolute level for the magnitude chosen; that is, the scatter in the moment-magnitude relation (Figure 5.5). We must also account for the standard error in the spectral estimate for a particular moment (Figure 6.1), but this is relatively small. Combining variances for these two contributions to the uncertainty, we compute the standard error for our spectral estimate. This is illustrated in Figure 7.3 with the predicted Pn spectrum at 800 km from a NORESS magnitude 3.0 explosion. The Lg spectral estimate has lower variance for fixed moment (Figure 6.1), but the variance of the Lg explosion moment-magnitude relation is larger than the corresponding variance for Pn . The result is that the standard error in our predicted Lg spectra is about the same as the error for Pn , which is illustrated in Figure 7.3.

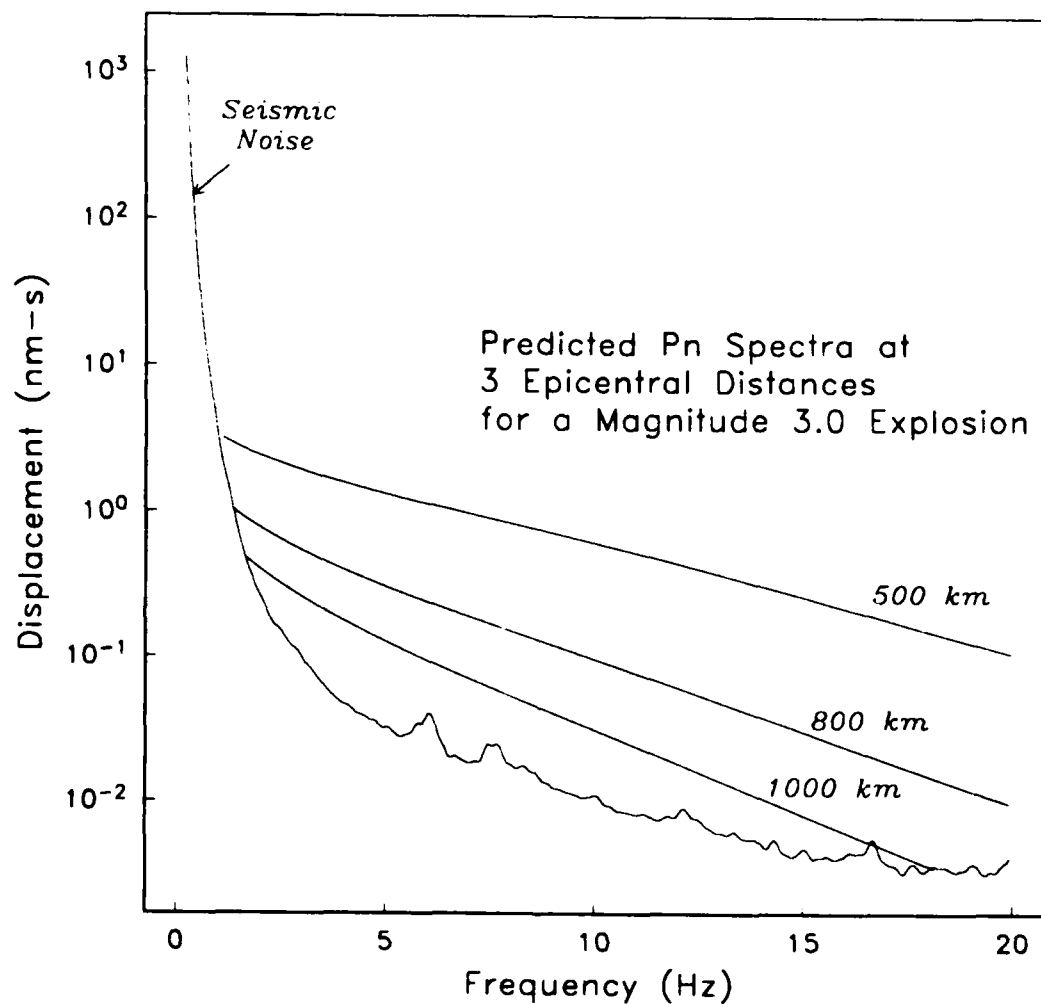


Figure 7.1. Predicted NORESS *Pn* displacement spectra at 3 epicentral distances for a magnitude 3.0 explosion, based on the inversion results. The average NORESS noise was estimated from samples taken prior to *Pn* for many events (Henson and Bache, 1986).

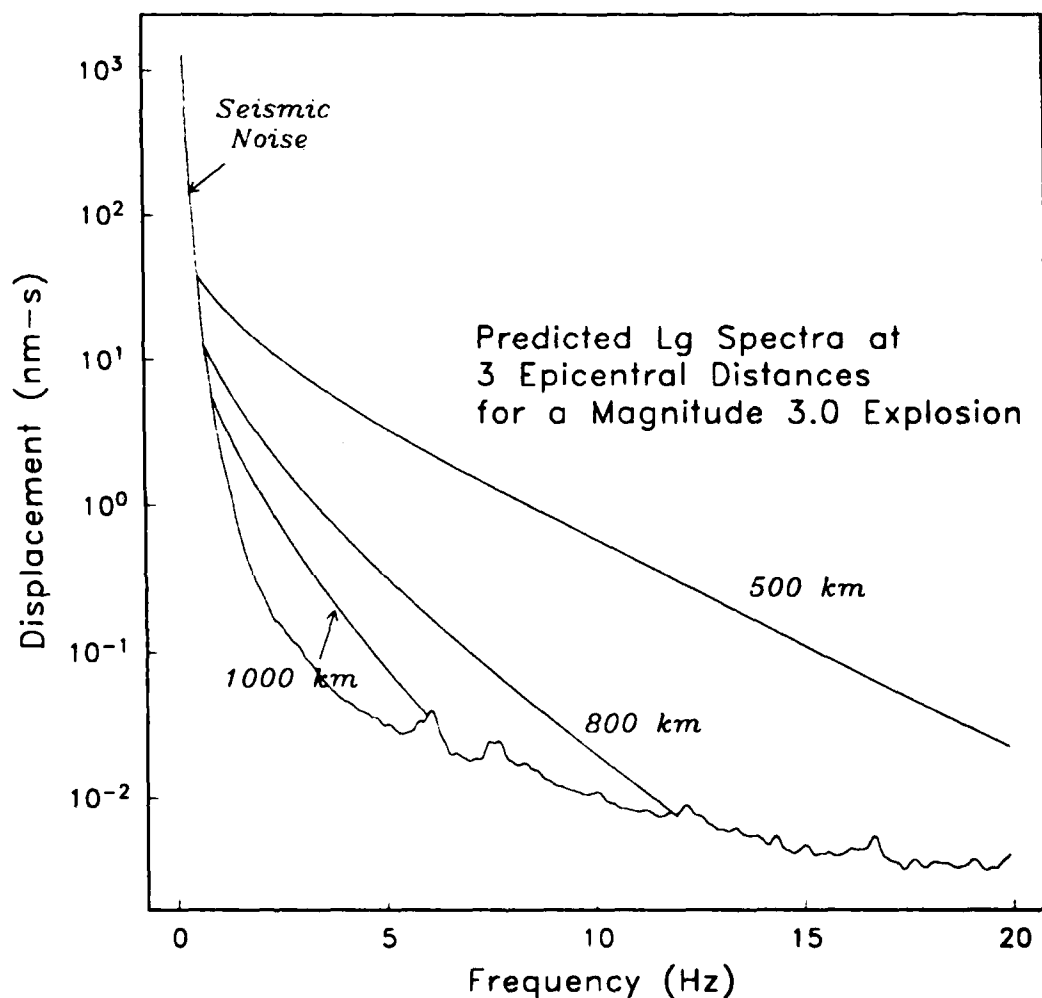


Figure 7.2. Predicted NORESS *Lg* displacement spectra at 3 epicentral distances for a magnitude 3.0 explosion, based on the inversion results. The average NORESS noise was estimated from samples taken prior to *Pn* for many events (Henson and Bache, 1986).

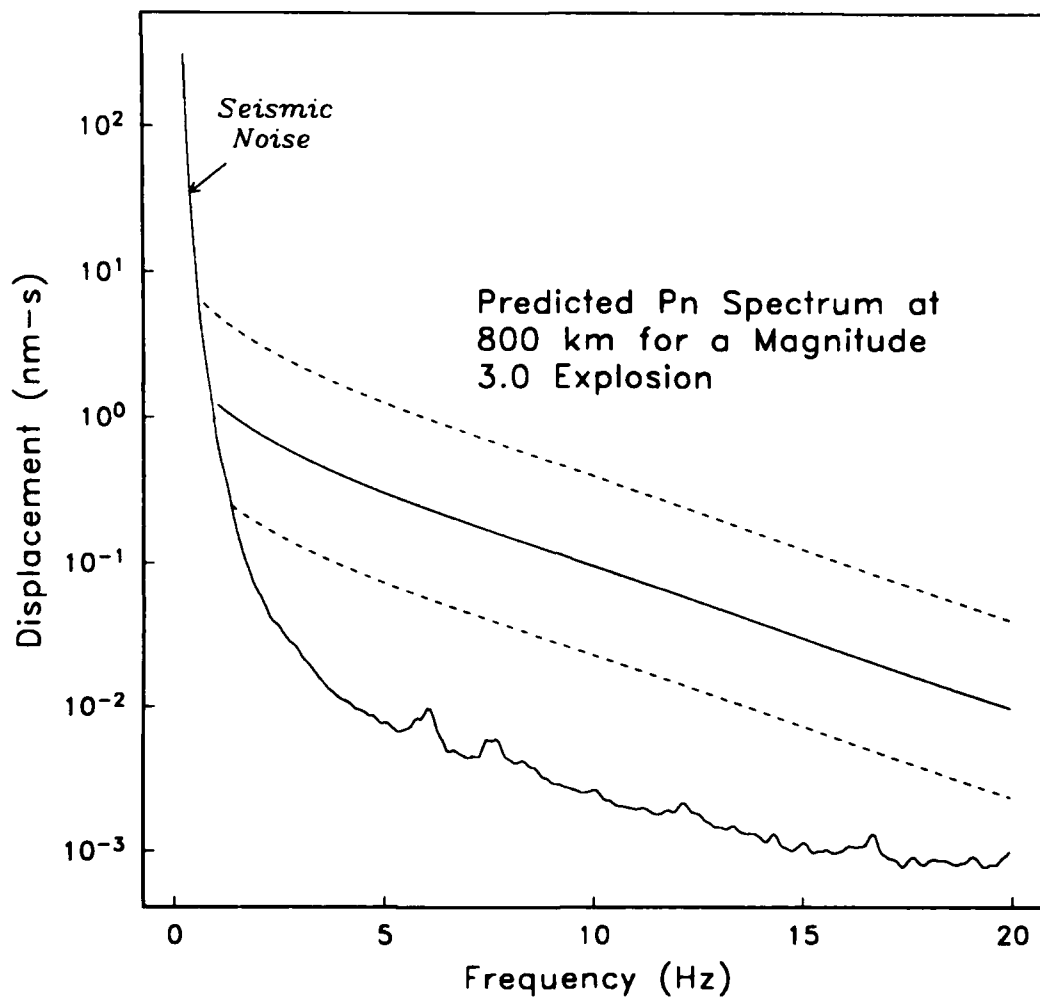


Figure 7.3. Predicted NORESS P_n displacement spectrum at 800 km for a magnitude 3.0 explosion, based on the inversion results. The dashed curves indicate one standard deviation including both the variance for fixed moment, σ_d^2 , and the M_0 - M_L variance. The average NORESS noise was estimated from samples taken prior to P_n for many events (Henson and Bache, 1986).

8. CONCLUSIONS

This report summarizes results of a detailed analysis of regional wave attenuation along continental paths to the NORESS array in Norway. We have developed and implemented a generalized inversion of log amplitude spectra that simultaneously estimates seismic moment and apparent attenuation. The method uses both the spatial and spectral decay of observed signal amplitudes to separate source and path contributions. The inversion was applied to Pn and Lg spectra from 190 regional events recorded at NORESS over distances of 200 to 1300 km. Based on adequate signal/noise, the Lg spectra were inverted between 1 and 7 Hz and Pn spectra between 1 and 15 Hz. The main conclusions of the study are as follows:

- Data from all 190 regional events are adequately modeled by a simple ω^2 source and a single frequency-dependent Q model. Theoretical spectra derived from this simple parameterization were compared to 322 observed regional wave spectra. The ability of the model to reproduce the important spectral characteristics of such a large number and variety of observed data provides support for the results that goes well beyond that in most published studies of regional wave attenuation.
- Regional Lg spectra are adequately represented from 1 to 7 Hz by a power-law frequency dependence of apparent attenuation given by $Q(f) = 350f^{0.41}$. Our short time windows include the onset of Lg which primarily consists of higher mode surface waves sampling the lower crust. Our $Q_{Lg}(f)$ is therefore an approximation to the Q of the lower crust, although it includes the effects of apparent attenuation due to scattering.
- Amplitudes of regional Pn phases are more sensitive to source radiation pattern, focussing and defocussing, and scattering. Nevertheless, a successful parameterization of regional P wave attenuation, particularly at high frequency, has important applications in treaty monitoring seismology. We have found that regional Pn spectra of 152 events are consistent with $r^{-1.3}$ geometric spreading and $Q_{Pn}(f) = 300f^{0.49}$. We do not attempt to distinguish intrinsic absorption from scattering and explicitly acknowledge that our $Q(f)$ is an empirical parameterization of the data.

- Our estimated seismic moments as a function of local magnitude are generally consistent with near-field studies. In that magnitude does not enter the inversion, this lends considerable support to the derived Q model. Corner frequencies, while in agreement with near-field studies, are not clearly resolved by our data.
- For a fixed set of source and spreading assumptions, the inversion defines a broad minimum in the data residuals corresponding to a suite of models that fit the data equally well in a least-squares sense. However, an important constraint on the attenuation estimates is the consistency of the derived source parameters from the independently inverted Pn and Lg spectra. This provides a firm internal consistency check on our attenuation results and reduces the trade-offs among model parameters to a set of model pairs. That is, for fixed $Q_{Lg}(f)$, the source constraint places tight bounds on $Q_{Pn}(f)$. A trade-off between M_0 - M_L variance and data variance is used to define the range of acceptable model pairs. The "preferred model" was merely selected from the mid-range of these acceptable solutions. The range of acceptable Q models for Lg is Q_0 between 300 and 400 and η between 0.46 and 0.37. Similarly, for Pn with $r^{-1.3}$ spreading, the range is Q_0 between 250 and 375 with η between 0.53 and 0.44.
- The $Q_{Lg}(f)$ results are insensitive to the details of our source parameterization. Most events considered had local magnitudes less than 3.0, and corner frequencies greater than the upper limit of the bandwidth inverted. The sensitivity of $Q_{Pn}(f)$ to source parameterization is unknown, although a spectral decay faster than ω^2 must be accompanied a higher Q_{Pn} to preserve the fit at high frequency. Therefore, the derived Q_{Pn} function must be considered relative to an ω^2 source model.
- Pn geometric spreading rates of r^{-1} , $r^{-1.3}$, and $r^{-1.5}$ were investigated. In each case, the inversion resulted in a Q model that could adequately reproduce the Pn spectra. However, only $r^{-1.3}$ resulted in an earthquake to explosion Lg excitation ratio which is consistent with other empirical studies.
- Data from all azimuths were combined into an inversion for a single, average Q model. No evidence for an azimuthal dependence in spectral decay was discovered, although explosions from different mines were found to produce distinctly different observed Lg to Pn ratios. It is not clear whether the low Lg/Pn ratios are due to

structural inhibition of *Lg* propagation or to different mining practices resulting in different *Pn* to *Lg* excitation ratios.

- The *Lg* and *Pn* attenuation models are used to predict range-dependent spectral amplitudes for events of arbitrary magnitude. For a broad distance range, the model predicts regional seismograms characterized by *Lg* the largest amplitude phase and *Pn* having a higher dominant frequency.

The final result of the inversion is an accurate parameterization of observed amplitude spectra of regional events recorded at NORESS that can be used to address a number of seismological problems related to wave propagation in the region and to the treaty monitoring capabilities of small regional networks.

ACKNOWLEDGEMENTS

We are grateful to Dale Breeding of the SCARS Project at Sandia National Laboratories for providing us with the NORESS data used in this report. We also acknowledge the assistance of our colleagues at SAIC. In particular, Ann Suteau-Henson adapted the automated array processing program used at NORSAR (*RONAPP*) for use on the SAIC Sun Computers. Alex Olender processed most of the events and provided us with numerous scripts and utility programs which greatly simplified the data accumulation and selection process. Donna Williams provided assistance in map graphics, on-line event bulletin searching, and data processing. Nancy Woltman contributed to the final preparation of the manuscript and figures.

REFERENCES

- Alewine, R. (1985), Seismic sensing of Soviet tests, in: *Defense 85, December*, American Forces Information Service, Arlington, Virginia, 11-21.
- Bache, T., P. Marshall and L. Bache (1985), Q for teleseismic P waves from central Asia, *J. Geophys. Res.*, **90**, 3575-3587.
- Bache, T., H. Swanger, B. Shkoller and S. Day (1981). Simulation of short-period L_g , expansion of three-dimensional source simulation capabilities and simulation of near-field ground motion from the 1971 San Fernando, California, earthquake, *Systems, Science and Software Final Technical Report SSS-R-81-5081*, July, F49620-80-C-0019.
- Baumgardt, D. and K. Ziegler (1987), Spectral evidence for source multiplicity in explosions, ENSCO, Inc. *Semi-Annual Technical Report SAS-TR-87-01*, January, AFGL-TR-87-0045.
- Bennett, T., J. Murphy and H. Shah (1987), Theoretical analysis of regional phase behavior, *Systems, Science and Software Technical Report SSS-R-87-8113*, July, F08606-85-C-0034.
- Brune, J. (1970), Tectonic stress and the spectra of seismic shear waves from earthquakes, *J. Geophys. Res.*, **75**, 4997-5009.
- Brune, J. (1971), Correction to tectonic stress and the spectra of seismic shear waves from earthquakes, *J. Geophys. Res.*, **76**, 5002.
- Bungum, H., S. Vaage and E. Husebye (1982), The Meloy earthquake sequence, northern Norway; source parameters and their moment scaling relations, *Bull. Seismol. Soc. Am.*, **72**, 197-206.
- Butler, R., C. McCreery, L. N. Frazer and D. Walker (1987), High-frequency seismic attenuation of oceanic P and S waves in the western Pacific, *J. Geophys. Res.*, **92**, 1383-1396.
- Campillo, M., J. Plantet and M. Bouchon (1985), Frequency-dependent attenuation in the crust beneath central France from L_g waves: Data analysis and numerical modeling, *Bull. Seismol. Soc. Am.*, **75**, 1395-1411.
- Chael, E. (1987), Spectral scaling of earthquakes in the Miramichi region of New Brunswick, *Bull. Seismol. Soc. Am.*, **77**, 347-365.
- Chavez, D. and K. Priestley (1986), Measurement of frequency dependent L_g attenuation in the Great Basin, *Geophys. Res. Lett.*, **13**, 551-554.

- Chavez, D. and K. Priestley (1987), Apparent Q of P_g and L_g in the Great Basin, DARPA/AFGL Seismic Research Symposium, 15-18 June 1987, 95-100.
- Cheng, C. and B. Mitchell (1981), Crustal Q structure in the United States from multi-mode surface waves, *Bull. Seismol. Soc. Am.*, **71**, 161-181.
- Chun, K., G. West, R. Kokoski and C. Samson (1987), A novel technique for measuring L_g attenuation - Results from eastern Canada between 1 to 10 Hz, *Bull. Seismol. Soc. Am.*, **77**, 398-419.
- Clements, J. (1982), Intrinsic Q and its frequency dependence, *Phys. Earth Planet. Inter.*, **27**, 286-299.
- Dwyer, J., R. Herrmann and O. Nuttli (1983), Spatial attenuation of the L_g wave in the central United States, *Bull. Seismol. Soc. Am.*, **73**, 781-796.
- Gonciz, J. and W. Dean (1986), Source spectral functions and path attenuation for EUS regional phases by regression analysis of RSTN data, *EOS*, **67**, 316.
- Gupta, I. and K. McLaughlin (1987), Attenuation of ground motion in the eastern United States, *Bull. Seismol. Soc. Am.*, **77**, 366-383.
- Hasegawa, H. (1983), L_g spectra of local earthquakes recorded by the Eastern Canada Telemetered Network and spectral scaling, *Bull. Seismol. Soc. Am.*, **73**, 1041-1061.
- Hasegawa, H. (1985), Attenuation of L_g waves in the Canadian Shield, *Bull. Seismol. Soc. Am.*, **75**, 1569-1582.
- Henson, A. and T. Bache (1986), Spectra of regional phases at Norell, *Science Applications International Corporation Technical Report 86/1967*, AFGL-TR-87-0003.
- Herrmann, R. and A. Kijko (1983), Modeling some empirical vertical component L_g relations, *Bull. Seismol. Soc. Am.*, **73**, 157-171.
- Knopoff, L., F. Schwab and E. Kausel (1973), Interpretation of L_g , *Geophys. J. R. Astr. Soc.*, **33**, 389-404.
- Kvaerna, T. and F. Ringdal (1986), Stability of various f-k estimation methods, Semi-Annual Technical Summary, 1 Apr - 30 Sept, NORSAR, *Sci. Rep. No. 1-86/87*, Kjeller, Norway.
- Langston, C. (1982), Aspects of P_n and P_g propagation at regional distances, *Bull. Seismol. Soc. Am.*, **72**, 457-471.
- Mitchell, B., J. Xie and O. Nuttli (1987), Seismic attenuation and yield estimates: New results using the L_g phase, DARPA/AFGL Seismic Research Symposium, 15-18 June 1987, 90-94.

- Mueller, C. and E. Cranswick (1985), Source parameters from locally recorded aftershocks of the 9 January 1982 Miramichi, New Brunswick, earthquake, *Bull. Seismol. Soc. Am.*, **75**, 337-360.
- Mueller, R. and J. Murphy (1971), Seismic characteristics of underground nuclear detonations, *Bull. Seismol. Soc. Am.*, **61**, 1675-1692.
- Murphy, J. and T. Bennett (1982), A discrimination analysis of short-period regional seismic data recorded at Tonto Forest observatory, *Bull. Seismol. Soc. Am.*, **72**, 1351-1366.
- Mykkeltveit, S., K. Astebol, D. Doornbos and E. Husebye (1983), Seismic array configuration optimization, *Bull. Seismol. Soc. Am.*, **73**, 173-186.
- Mykkeltveit, S. and H. Bungum (1984), Processing of regional seismic events using data from small-aperture arrays, *Bull. Seismol. Soc. Am.*, **74**, 2313-2333.
- Mykkeltveit, S. and F. Ringdal (1979), *P* and *Lg* wave attenuation in selected frequency bands in the 1-5 Hz range using NORSAR short period records, *Sci. Rep. No. 1-79/80*, NTNF/NORSAR, Kjeller, Norway.
- Nuttli, O. (1981), On the attenuation of *Lg* waves in western and central Asia and their use as a discriminant between earthquakes and explosions, *Bull. Seismol. Soc. Am.*, **71**, 249-261.
- Nuttli, O. (1986), Yield estimates of Nevada test site explosions obtained from seismic *Lg* waves, *J. Geophys. Res.*, **91**, 2137-2151.
- Panza, G. and G. Calcagnile (1975), *Lg*, *Li* and *Rg* from Rayleigh modes, *Geophys. J. R. Astr. Soc.*, **40**, 475-487.
- Pesceckis, L. and P. Pomeroy (1984), Determination of *Q* using *Lg* waves and its implications for nuclear yield estimation, *EOS*, **45**, 995.
- Pomeroy, P. (1977), Aspects of seismic wave propagation in eastern North America - A preliminary report, Rondout Associates, Inc., Stone Ridge, New York.
- Pomeroy, P., W. Best and T. McEvilly (1982), Test ban treaty verification with regional data - A review, *Bull. Seismol. Soc. Am.*, **72**, S89-S129.
- Press, W., B. Flannery, S. Teukolsky and W. Vetterling (1986), *Numerical Recipes: The Art of Scientific Computing*, Cambridge University Press, Cambridge.
- Ringdal, F. (1986), Summary of technical reports/papers prepared, Semi-Annual Technical Summary, 1 Oct - 31 March, NORSAR *Sci. Rept. No. 2-85/86*, Kjeller, Norway.
- Ringdal, F., B. Kr. Hokland and T. Kvaerna (1986), Initial results from the NORESS high frequency seismic element (HFSE), Semi-Annual Technical Summary, 1 Oct - 31 March, NORSAR *Sci. Rept. No. 2-85/86*, Kjeller, Norway.

- Sereno, T. and J. Orcutt (1987), Synthetic P_n and S_n phases and the frequency dependence of Q of oceanic lithosphere, *J. Geophys. Res.*, **92**, 3541-3566.
- Shin, T. and R. Herrmann (1987), Lg attenuation and source studies using 1982 Miramichi data, *Bull. Seismol. Soc. Am.*, **77**, 384-397.
- Singh, S. and R. Herrmann (1983), Regionalization of crustal coda Q in the continental United States, *J. Geophys. Res.*, **88**, 527-538.
- Stevens, J. and S. Day (1985), The physical basis of m_b : M_s and variable frequency magnitude methods for earthquake/explosion discrimination, *J. Geophys. Res.*, **90**, 3009-3020.
- Street, R., R. Herrmann and O. Nuttli (1975), Spectral characteristics of the Lg wave generated by central United States earthquakes, *Geophys. J. R. Astron. Soc.*, **41**, 51-63.
- Taylor, S., B. Bonner and G. Zandt (1986), Attenuation and scattering of broadband P and S waves across North America, *J. Geophys. Res.*, **91**, 7309-7325.
- Willis, D. (1963), Comparison of seismic waves generated by different types of sources, *Bull. Seismol. Soc. Am.*, **53**, 965-978.

APPENDIX A. PROCESSED EVENTS NOT INCLUDED IN THE INVERSION

Section 4 tabulates the events used in the generalized inversion. In addition to these, there were 68 events processed that were not included in the inversion. Table A.1 identifies this set of events. Most of these events were excluded because of low signal/noise ratios. Others were excluded because they were out of the regional distance range to NORESS. Event 6 of Table A.1 is a regional Soviet Peaceful Nuclear Explosion (PNE) with $m_b = 5.0$. This event was excluded because it was considerably larger than other events in the data set and because its source spectrum is likely to be inherently different from spectra of the small, near-surface, mine blasts comprising the majority of the events used.

Many of the events in Table A.1 were processed to test and evaluate the performance of the "expert system" currently under development at SAIC. These events were selected because they are, in some sense, difficult as a result of low signal/noise ratios, mixed events, problems in location due to phase misassociation, etc. A few of the events listed in Table A.1 were excluded because signals from multiple events were mixed. Others, without independent network solutions, had ambiguous phase associations and therefore uncertain locations. There were a couple of events that were reported by an independent network, but that location did not agree with the arrival pattern recorded at NORESS.

More fundamentally, however, there were 16 events that had regional wave spectra inconsistent with the other events at approximately the same distance. These are events 15-23, 25-26, 40, 45, and 50-52 of Table A.1. Their locations are plotted on a map relative to NORESS in Figure A.1. For each of these events, the Pn and Lg spectra decay with frequency considerably faster than is predicted by the model derived from the events in Table 4.1. Event 50 is located only 3 km from mine NYG (Table 4.2) and the other 15 events are all presumed earthquakes. Event 45 does not have an independent network solution, although there is nothing apparently wrong with the *RONAPP* phase association. Events 40, 45, and 50 appear to be "anomalous events" in that other events along the same azimuth and approximate distance have spectra consistent with the majority of the events studied. Regional spectra from events 51 and 52 (located near the northern tip of Denmark) may reflect greater path attenuation, however the interpretation is ambiguous. Events 15-23 and 25-26 all occurred within a 24 hour period and were located off the southwest coast of Norway (Figure A.1). It is not known whether these are off-shore earthquakes or underwater explosions (Henson and Bache, 1986). Because they are so nearly contemporaneous and of similar magnitude, it is difficult to rule out anomalous source characteristics as contributing to the difference between these spectra and those of the

Table A.1. Events processed not included in the inversion.

Event	Date	Time	Location	Type	Magnitude	
1	4-25-85	0:57	49.90N 79.00E	EX	5.9	(P)
2	5-17-85	0:25	55.00N 93.00E	EX	3.6	(N)
3	6-18-85	3:58	55.00N 91.00E	EX	4.1	(N)
4	6-30-85	2:39	49.90N 79.00E	EX	6.0	(P)
5	7-11-85	--	-- --	EX	3.5	†
6	7-18-85	21:15	66.00N 40.90E	EX-PNE	5.0	(P)
7	7-25-85	3:11	49.90N 78.20E	EX	5.0	(P)
8	10-30-85	7:40	72.08N 1.34W	EQ	4.4	(P)
9	11- 6-85	9:00	64.70N 30.70E	EX-V10	2.7	(R)
10	11- 8-85	0:08	51.68N 16.20E	EQ	2.6	(R)
11	11-14-85	10:44	62.70N 17.76E	EQ	2.5	(R)
12	11-14-85	18:20	59.40N 34.20E*	EQ	3.2	(R)
13	11-15-85	11:00	67.60N 34.20E	EX-K5	2.7	(H)
14	11-15-85	12:01	63.20N 27.80E	EX-M7	2.1	(H)
15	11-20-85	22:11	57.61N 5.67E	EQ	2.3	(B)
16	11-20-85	22:25	57.66N 5.72E	EQ	2.2	(B)
17	11-20-85	22:57	57.63N 6.27E	EQ	2.2	(B)
18	11-20-85	23:11	57.66N 5.35E	EQ	2.3	(B)
19	11-20-85	23:17	57.69N 5.45E	EQ	2.3	(B)
20	11-20-85	23:23	57.64N 5.62E	EQ	2.2	(B)
21	11-20-85	23:28	57.58N 5.49E	EQ	2.2	(B)
22	11-21-85	14:07	57.75N 5.30E	EQ	2.3	(B)
23	11-21-85	14:18	57.06N 6.36E	EQ	2.3	(B)
24	11-21-85	14:48	54.80N 6.50E*	EQ	2.8	(R)
25	11-21-85	15:05	57.44N 5.74E	EQ	2.3	(B)
26	11-21-85	15:48	58.30N 4.80E*	EQ	2.1	(R)
27	11-29-85	12:24	59.60N 18.70E*	EQ	1.7	(R)
28	12- 4-85	14:00	60.73N 11.31E	EQ	2.3	(B)
29	12-11-85	20:21	15.57N 16.16E	EQ	3.9	(P)
30	12-13-85	11:00	64.70N 30.70E	EX-V10	2.5	(H)
31	12-13-85	14:14	67.60N 34.00E	EX-K2	2.8	(H)
32	12-16-85	16:44	67.10N 20.60E	EX-R1	2.5	(H)
33	12-13-85	2:35	60.38N 1.90E	EQ	2.3	(B)
34	12-23-85	3:25	50.21N 12.39E	EQ	4.3	(P)
35	12-26-85	13:33	58.90N 33.40E*	EQ	3.1	(R)
36	1- 3-86	6:16	59.56N 7.45E	--	2.4	(B)
37	1- 9-86	9:18	54.70N 19.50E*	EQ	2.7	(R)
38	1- 9-86	20:35	51.25N 15.57E	EQ	3.6	(P)
39	1-13-86	9:36	64.60N 20.40E*	EQ	2.2	(R)
40	1-19-86	4:59	64.95N 12.13E	EQ	3.0	(H)
41	1-23-86	2:22	50.21N 12.40E	EQ	4.2	(P)
42	1-24-86	11:00	64.70N 30.70E	EX-V10	2.4	(H)
43	1-31-86	11:02	64.70N 30.70E	EX-V10	2.4	(H)
44	2- 3-86	15:53	58.46N 12.10E	EQ	2.6	(B)
45	2-13-86	19:06	60.30N 15.00E*	EQ	1.4	(R)

Event	Date	Time	Location	Type	Magnitude
46	2-16-86	15:04	58.29N 30.40E	EQ	<2.0 (H)
47	2-24-86	1:13	59.30N 3.70E	EQ	1.5 (R)
48	4- 8-86	10:06	59.30N 27.60E	EX-E6	2.1 (H)
49	4- 8-86	10:30	64.33N 20.56E*	EQ	2.4 (H)
50	4- 8-86	11:28	60.39N 5.29E	--	1.9 (B)
51	4- 9-86	8:16	57.31N 10.60E	EQ	2.5 (B)
52	4- 9-86	8:27	57.30N 10.48E	EQ	2.5 (B)
53	4-18-86	0:44	59.22N 1.42E	EQ	2.4 (B)
54	4-30-86	6:05	57.28N 6.19E	EQ	2.2 (B)
55	4-30-86	6:23	57.40N 6.17E	EQ	2.3 (B)
56	5- 2-86	10:45	60.35N 5.08E	--	1.8 (B)
57	5- 5-86	15:37	60.24N 5.28E	--	1.5 (B)
58	5-27-86	18:36	61.51N 5.84E	EQ	1.6 (B)
59	6-11-86	14:08	59.39N 18.66E	EQ	2.1 (H)
60	6-17-86	12:03	58.59N 18.14E	EQ	2.6 (H)
61	7-19-86	11:54	54.10N 21.67E	EQ	2.3 (H)
62	7-30-86	13:43	59.50N 30.00E	EX	2.0 (H)
63	7-30-86	22:30	59.77N 11.05E	EQ	2.4 (B)
64	8-10-86	5:01	59.99N 5.34E	--	1.5 (B)
65	8-18-86	8:25	59.50N 25.00E	EX-E3	2.0 (H)
66	10-12-86	14:53	60.92N 5.11E	EQ	1.9 (B)
67	10-30-86	9:21	59.60N 10.80E*	EQ	1.2 (R)
68	10-30-86	9:22	60.80N 6.40E*	EQ	1.6 (R)

* *RONAPP* Location

† Alewine, 1985

(B) Bergen network magnitude

(H) Helsinki network magnitude

(N) NORSAR magnitude

(P) PDE magnitude (M_b)

(R) *RONAPP* magnitude

Events With Anomalous Spectra

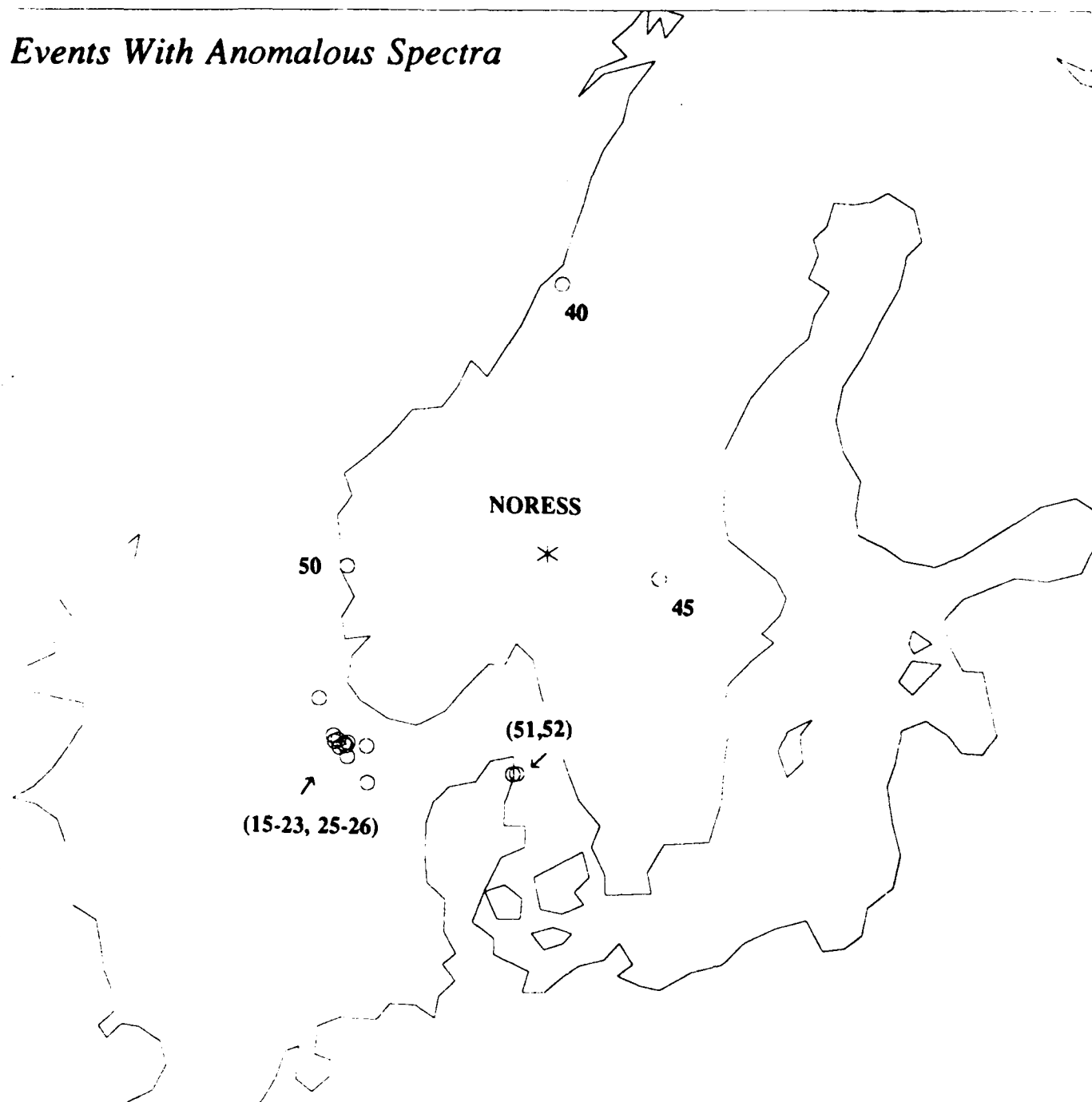


Figure A.1 Locations of events with anomalous spectra. The events are identified by the event numbers in Table A.1. Events 15-23 and 25-56 all occurred within a 24 hour time period and may be underwater explosions (Henson and Bache, 1986).

nearby Titania mine. Clearly, the other possibility is considerable path attenuation between these event epicenters and the coast of Norway. These events will be discussed in more detail in Section 6.5.

APPENDIX B. INVERSION RESULTS

Regional *Pn* and *Lg* spectra of 190 events (Table 4.1) were inverted for $Q(f)$, seismic moment, and the parameter, c , relating corner frequency to long period source level. The source was parameterized by the Mueller-Murphy explosion model (3.1.4) and geometric spreading was modeled by (3.1.2) with $m = 1/2$ and $r_0 = 100$ km for *Lg* and $m = 1.3$ with $r_0 = 1$ km for *Pn*. In terms of a power-law frequency dependence, the path result for *Pn* is $Q(f) = 300f^{0.49}$ and for *Lg* is $Q(f) = 350f^{0.41}$. The parameter, c , derived from *Pn* spectra is 29.2 and from *Lg* spectra is 28.7.

Table B.1 lists the results of the inversion for source parameters. The event numbers correspond to those of Table 4.1 and the mine identifications for the explosions are given in Table 4.2. Corner frequencies were not parameters of the inversion for each event, but were calculated from (3.1.6) using the inversion results for c . For the explosions, seismic moment was estimated from $S_0(Pn)$ using (3.1.7) assuming a surface compressional velocity of 5 km/s and a density of 2.5 gm/cm³. The earthquake moments were estimated from $S_0(Lg)$ using (3.1.9) with an average crustal shear wave velocity of 3.5 km/s and a crustal density of 2.7 gm/cm³. Because the radiation patterns are unknown, moments were not estimated for earthquakes for which only *Pn* spectra were included in the inversion or for events of unknown source type. Similarly, moments were not estimated for explosions without *Pn* spectra because of the uncertainty in the relative *Lg* to *Pn* source excitation (3.1.10).

Figure B.1 displays theoretical and data spectra for all of the events used in the inversion. The theoretical spectra were computed using (3.1.1) with the results of the inversion for $Q(f)$ and $S(f)$. Each spectrum is identified by the event number in Table 4.1. The spectra have been vertically offset for display purposes.

Table B.1. Inverted source parameters

Event	Magnitude	Type	$S_0(Pn)$	$f_c(Pn)$	$S_0(Lg)$	$f_c(Lg)$	M_0 (10^{18} dyne-cm)
1	3.0	EX-E7	28.89	9.5	15.90	11.4	1134.7
2	2.8	(B) EQ	3.20	19.9	4.77	17.0	69.5
3	2.3	EQ	1.71	24.5	3.60	18.7	52.3
4	2.2	EQ	1.00	29.3	2.06	22.5	30.0
5	1.9	(R) EX-BLA	1.77	24.2	1.06	28.1	69.5
6	2.8	EQ	1.25	27.1	4.61	17.2	67.1
7	2.8	EX-V5	27.16	9.7	21.00	10.4	1066.4
8	2.4	EX-BLA	2.05	23.0	1.62	24.4	80.7
9	2.1	EX-TIT	0.72	32.7	0.75	31.6	28.1
10	2.0	(R) --	1.32	26.7	0.74	31.7	---
11	2.6	EX-E3	----	---	4.56	17.3	---
12	2.7	EX-E7	16.89	11.4	12.61	12.3	663.1
13	1.9	EX-TIT	0.98	29.5	0.83	30.4	38.5
14	2.9	EX-V12	36.17	8.8	12.44	12.4	1420.5
15	2.9	EX-V8	34.91	8.9	----	---	1370.8
16	2.4	(H) EX-E4	----	---	15.17	11.6	---
17	1.9	--	1.03	28.9	0.64	33.2	---
18	2.5	EX-E3	----	---	3.65	18.6	---
19	3.0	EX-E8	----	---	10.62	13.0	---
20	3.0	EQ	0.89	30.4	7.39	14.7	107.6
21	2.8	EX-V4	45.96	8.2	----	---	1804.9
22	2.1	(R) EQ	0.63	34.1	0.70	32.2	10.2
23	3.0	EQ	2.39	21.9	7.16	14.9	104.2
24	2.8	EX-K1	----	---	50.54	7.8	---
25	<2.0	(H) EX-V2	17.35	11.3	----	---	681.5
26	3.1	EX-E4	----	---	12.72	12.3	---
27	2.2	--	0.48	37.3	1.35	25.9	---
28	1.9	EQ	0.46	37.9	0.71	32.1	10.3
29	3.2	EX-E8	----	---	13.41	12.1	---
30	2.0	(R) EX-V11	17.04	11.4	13.51	12.0	669.1
31	2.0	EQ	3.01	20.3	1.64	24.3	23.8
32	3.3	EX-E8	42.87	8.4	27.11	9.5	1683.3
33	2.8	EX-E6	----	---	6.78	15.1	---
34	2.8	EX-E8	32.04	9.2	23.84	10.0	1258.2
35	2.4	(H) EX-V2	38.85	8.6	----	---	1525.8
36	2.5	(H) EX-V2	43.83	8.3	----	---	1721.3
37	3.2	(R) EQ	17.54	11.3	----	---	---
38	2.6	(R) EQ	19.97	10.8	----	---	---
39	2.6	EX-E3	----	---	3.18	19.5	---
40	2.9	EX-V1C	19.83	10.8	13.55	12.0	778.6
41	2.6	EX-E6	----	---	5.12	16.6	---
42	2.7	EQ	9.95	13.6	7.91	14.4	115.0
43	2.2	(H) EX-V4	21.92	10.4	----	---	861.0
44	3.3	EX-E8	36.72	8.8	22.92	10.1	1442.0

Event	Magnitude	Type	$S_0(Pn)$	$f_c(Pn)$	$S_0(Lg)$	$f_c(Lg)$	M_o (10^{18} dyne-cm)
45	2.4	(H)	EX-V2	42.05	8.4	----	1651.2
46	2.8		EQ	5.96	16.1	6.70	97.5
47	4.7	(P)	EQ	149.01	5.5	----	---
48	2.7		EX-E9	----	---	3.56	18.8
49	2.7		--	----	---	4.68	17.1
50	4.8	(P)	EQ	222.96	4.8	----	---
51	4.6	(P)	EQ	135.12	5.7	----	---
52	2.3	(H)	EX-M7	4.12	18.2	----	161.7
53	2.1		EX-TIT	1.78	24.1	0.97	29.0
54	2.9		EX-V7	18.04	11.1	23.32	10.0
55	2.8		--	18.97	11.0	23.64	10.0
56	1.8		EX-TIT	0.99	29.3	0.58	34.3
57	2.6		EQ	----	---	2.05	22.6
58	2.5		EX-E7	22.54	10.4	18.19	10.9
59	2.7		--	2.35	22.0	7.56	14.6
60	3.4		EX-E8	34.73	9.0	23.83	10.0
61	2.7		EX-E8	19.59	10.8	12.04	12.5
62	3.3		EX-E7	40.22	8.5	24.44	9.9
63	2.3		EX-TIT	3.08	20.1	2.16	22.2
64	3.3		EQ	35.17	8.9	94.57	6.3
65	2.5		EQ	3.19	19.9	3.69	18.5
66	1.7		EQ	0.67	33.5	0.41	38.7
67	2.9		EQ	2.21	22.5	5.18	16.6
68	2.5		EQ	1.51	25.5	6.95	15.0
69	3.3		EX-V8	42.24	8.4	18.23	10.9
70	3.3		EX-E7	25.26	10.0	17.41	11.1
71	1.9		EX-TIT	1.00	29.3	0.74	31.7
72	2.9		EX-K2	----	---	46.23	8.0
73	1.9		EQ	----	---	0.72	32.0
74	1.6		EQ	----	---	0.39	39.2
75	2.3		EQ	1.48	25.7	2.80	20.3
76	1.9		EQ	0.81	31.4	1.54	24.8
77	2.6		EX-E7	28.68	9.6	20.01	10.6
78	2.6		EX-R1	----	---	3.61	18.7
79	3.1		EX-V10	137.90	5.7	55.80	7.5
80	2.5		EX-E12	----	---	11.07	12.9
81	1.9	(R)	EQ	----	---	31.21	9.1
82	2.8	(H)	EX-K5	85.18	6.6	102.19	6.1
83	2.2	(H)	EQ	4.78	17.4	6.79	15.1
84	2.7		EX-E8	19.08	10.9	17.58	11.0
85	2.2		EQ	----	---	2.36	21.5
86	2.4		EX-TIT	2.50	21.6	3.72	18.5
87	2.3	(B)	EX-TIT	0.63	34.1	----	---
88	1.8		EQ	----	---	0.46	37.1
89	2.5		EX-R1	----	---	1.80	23.6
90	1.7		EQ	0.40	39.6	0.38	39.6
91	2.5	(H)	EX-E4	----	---	12.57	12.3

Event	Magnitude	Type	$S_0(Pn)$	$f_c(Pn)$	$S_0(Lg)$	$f_c(Lg)$	M_o (10^{18} dyne-cm)
92	3.1	EX-E4	----	---	24.06	9.9	---
93	2.6	EX-V10	26.84	9.8	30.10	9.2	1054.1
94	3.1	EX-K2	57.25	7.6	95.22	6.3	2248.0
95	1.9	EQ	0.62	34.3	1.36	25.9	19.7
96	3.2	EX-E9	----	---	16.08	11.4	---
97	1.8	EQ	1.29	26.9	0.71	32.1	10.3
98	3.3	EX-E7	26.04	9.9	20.94	10.4	1022.6
99	1.9	EQ	0.61	34.4	0.93	29.4	13.5
100	2.1	EQ	0.75	32.2	1.69	24.1	24.6
101	3.2	EX-E7	34.76	9.0	22.77	10.1	1365.1
102	3.2	EX-E7	16.96	11.4	18.04	10.9	665.9
103	2.8	EX-V8	15.44	11.7	----	---	606.3
104	2.9	EX-V5	19.55	10.9	34.60	8.8	767.8
105	2.8	EX-K5	----	---	95.20	6.3	---
106	2.6	EX-E3	----	---	3.15	19.6	---
107	2.5	EX-E4	6.41	15.7	9.05	13.8	251.9
108	2.0	EQ	0.85	30.9	0.85	30.3	12.4
109	3.5	EX-E8	30.83	9.3	34.73	8.8	1210.9
110	1.6	EQ	0.22	48.6	0.28	43.6	4.1
111	1.9	EX-TIT	1.04	28.8	0.64	33.2	41.0
112	4.4	(H) EQ	1593.86	2.5	----	---	---
113	2.0	EQ	0.75	32.2	1.15	27.4	16.7
114	2.8	--	13.39	12.3	14.63	11.7	---
115	3.0	EX-V1C	20.35	10.7	11.58	12.7	799.3
116	1.8	(B) EX-NYG	----	---	0.26	44.9	---
117	2.1	--	1.62	24.9	1.27	26.5	---
118	2.7	EX-K2	----	---	108.05	6.0	---
119	2.5	EX-V2	38.56	8.7	25.82	9.7	1514.3
120	2.4	--	0.86	30.8	1.23	26.8	---
121	2.6	EQ	----	---	4.40	17.5	63.9
122	2.2	EX-BLA	1.55	25.2	1.53	24.9	61.0
123	2.3	EQ	----	---	1.37	25.8	19.9
124	3.1	EX-V7	----	---	26.29	9.6	---
125	2.4	EQ	0.78	31.8	3.03	19.8	44.1
126	2.6	--	----	---	25.19	9.8	---
127	2.3	EX-BLA	1.48	25.7	0.85	30.3	57.9
128	2.4	EX-BLA	3.08	20.1	2.39	21.5	120.9
129	2.0	EQ	1.21	27.5	1.15	27.4	16.7
130	2.7	EQ	1.49	25.6	4.50	17.4	65.5
131	3.9	EX-V3	159.16	5.4	154.30	5.3	6250.2
132	1.7	EX-TIT	1.12	28.1	0.74	31.7	44.1
133	3.0	EX-E5	----	---	7.75	14.5	---
134	3.7	EX-V3	54.67	7.7	----	---	2146.9
135	2.6	EX-V1C	33.74	9.0	32.54	9.0	1325.0
136	3.1	--	6.94	15.3	14.99	11.6	---
137	3.2	EQ	3.99	18.4	20.58	10.5	299.4
138	1.1	EQ	----	---	0.11	59.4	1.6

Event	Magnitude	Type	$S_0(Pn)$	$f_c(Pn)$	$S_0(Lg)$	$f_c(Lg)$	M_o (10^{18} dyne-cm)
139	2.5	EX-BLA	3.59	19.1	2.19	22.1	141.0
140	1.6	EQ	0.87	30.6	0.37	39.9	5.4
141	1.8	EX-TIT	1.14	28.0	0.69	32.5	44.7
142	2.9	EX-V4	25.78	9.9	35.01	8.8	1012.5
143	2.1	EQ	0.58	35.1	1.57	24.7	22.8
144	2.4	--	3.52	19.2	2.69	20.6	---
145	2.6	EX-V10	----	---	18.86	10.8	---
146	2.8	EQ	11.29	13.0	14.15	11.9	205.8
147	2.7	EX-V12	27.35	9.7	24.74	9.8	1074.2
148	3.2	--	41.64	8.4	31.41	9.1	---
149	2.7	EX-E4	10.14	13.5	13.54	12.0	398.3
150	2.3	EX-BLA	2.08	22.9	1.65	24.3	81.7
151	2.0	EQ	1.68	24.6	1.58	24.6	22.9
152	4.3	EQ	67.22	7.2	----	---	---
153	3.2	EX-V8	39.10	8.6	31.63	9.1	1535.6
154	3.4	EQ	5.93	16.2	11.43	12.7	166.3
155	3.1	EX-K9	117.64	6.0	120.25	5.8	4619.6
156	3.5	EQ	7.73	14.8	35.61	8.7	518.0
157	3.0	EX-E4	13.11	12.4	14.17	11.8	515.0
158	2.3	EX-BLA	2.79	20.8	1.94	23.0	109.6
159	3.1	EX-E8	13.24	12.4	17.58	11.0	519.9
160	3.0	EX-E6	8.37	14.4	11.51	12.7	328.8
161	2.8	EX-V1B	17.05	11.4	11.16	12.8	669.7
162	2.2	EX-BLA	2.39	21.9	1.42	25.5	93.8
163	2.6	(H) EX-K4	93.90	6.4	----	---	3687.4
164	2.3	EX-BLA	1.94	23.4	1.32	26.2	76.3
165	3.2	EX-E7	27.99	9.6	20.10	10.5	1099.3
166	2.6	EX-E4	----	---	9.08	13.7	---
167	2.8	--	8.97	14.1	15.89	11.4	---
168	2.4	EX-BLA	2.51	21.5	1.67	24.2	98.7
169	3.1	--	5.78	16.3	----	---	---
170	3.0	EX-E2	3.63	19.0	9.73	13.4	142.5
171	2.6	EX-R1	10.83	13.2	6.00	15.8	425.3
172	1.9	EX-TIT	0.79	31.6	0.89	29.8	31.1
173	2.4	EX-BLA	2.40	21.8	1.93	23.0	94.2
174	2.3	EQ	1.23	27.3	1.48	25.2	21.5
175	3.9	EQ	64.09	7.3	151.96	5.4	2210.6
176	2.1	EX-BLA	2.23	22.4	1.02	28.5	87.7
177	3.0	--	----	---	14.50	11.8	---
178	2.4	EX-BLA	2.49	21.6	1.70	24.0	97.7
179	2.5	EQ	1.42	26.0	2.99	19.9	43.5
180	3.3	EQ	3.19	19.9	23.14	10.1	336.6
181	1.9	EQ	1.08	28.5	0.79	31.0	11.5
182	1.9	EX-TIT	0.98	29.5	0.76	31.5	38.3
183	2.0	EX-TIT	1.41	26.1	1.08	28.0	55.5
184	2.1	EQ	1.97	23.3	1.64	24.3	23.9
185	2.4	EQ	2.34	22.0	3.95	18.1	57.5

Event	Magnitude		Type	$S_0(Pn)$	$f_c(Pn)$	$S_0(Lg)$	$f_c(Lg)$	M_o (10^{18} dyne-cm)
186	2.6	(B)	EQ	4.57	17.6	7.71	14.5	112.1
187	2.3		EQ	4.02	18.4	3.39	19.1	49.3
188	2.4		EQ	1.06	28.7	1.63	24.4	23.7
189	3.4	(B)	EQ	12.06	12.8	21.57	10.3	313.8
190	1.8		EQ	0.97	29.6	0.55	34.9	8.1

(B) Bergen network magnitude

(H) Helsinki network magnitude

(P) PDE magnitude (M_b)

(R) *RONAPP* uncorrected magnitude

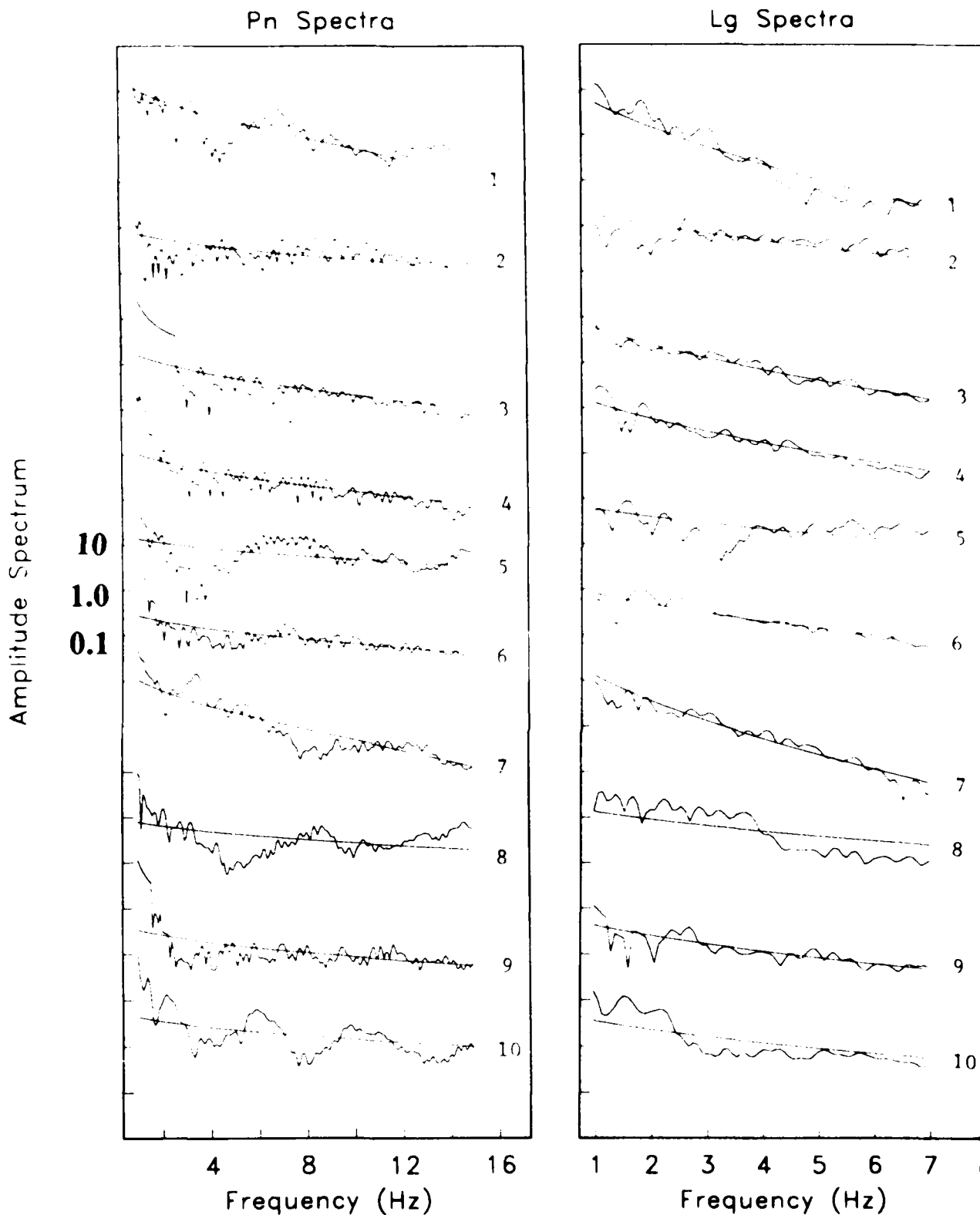


Figure B.1 Theoretical Pn and Lg spectra compared to observed spectra for the 190 events used in the generalized inversion. The theoretical spectra were computed using the inversion parameters described in Appendix B and listed in Table B.1.

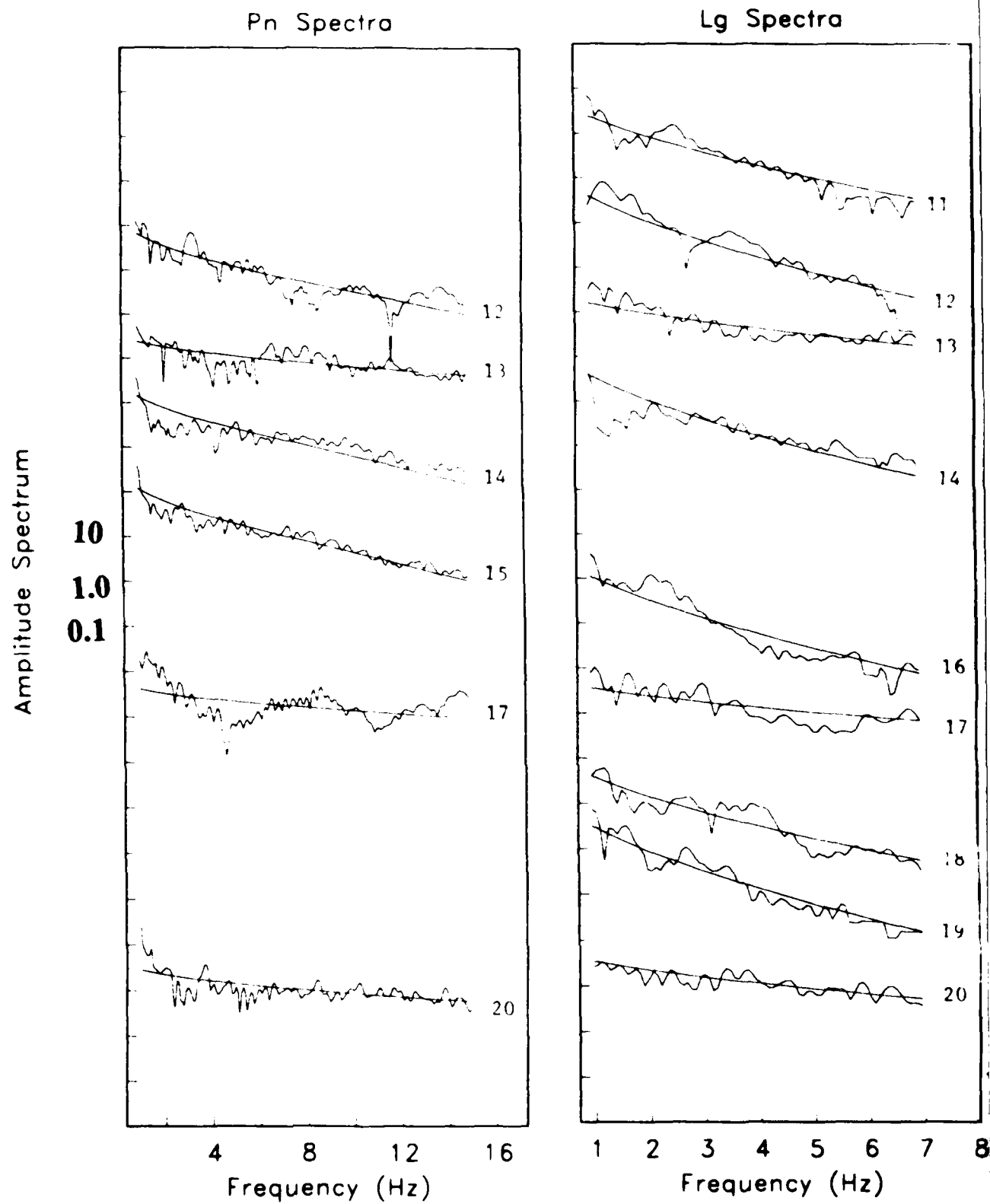


Figure B.1 (Continued).

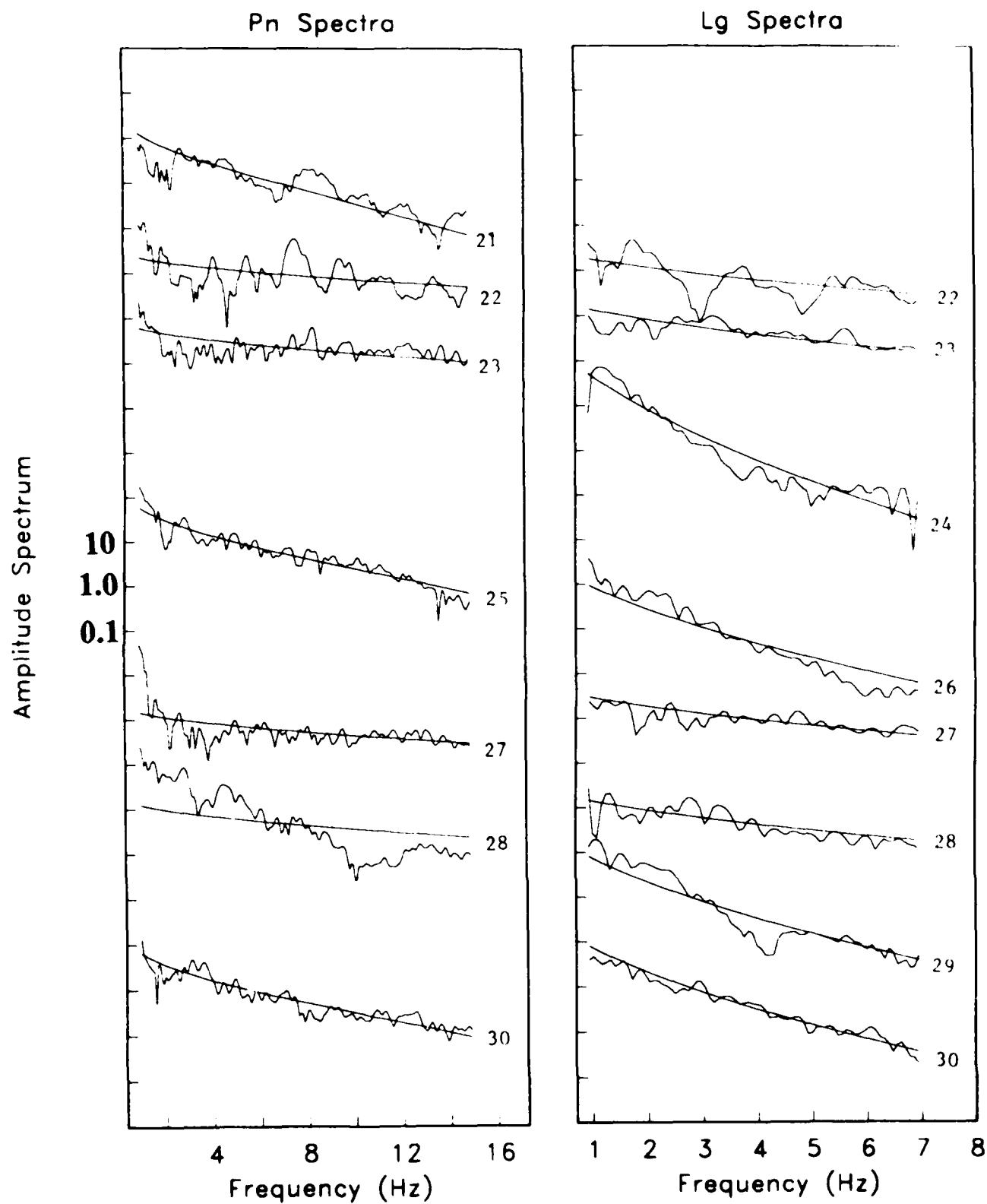


Figure B.1 (Continued).

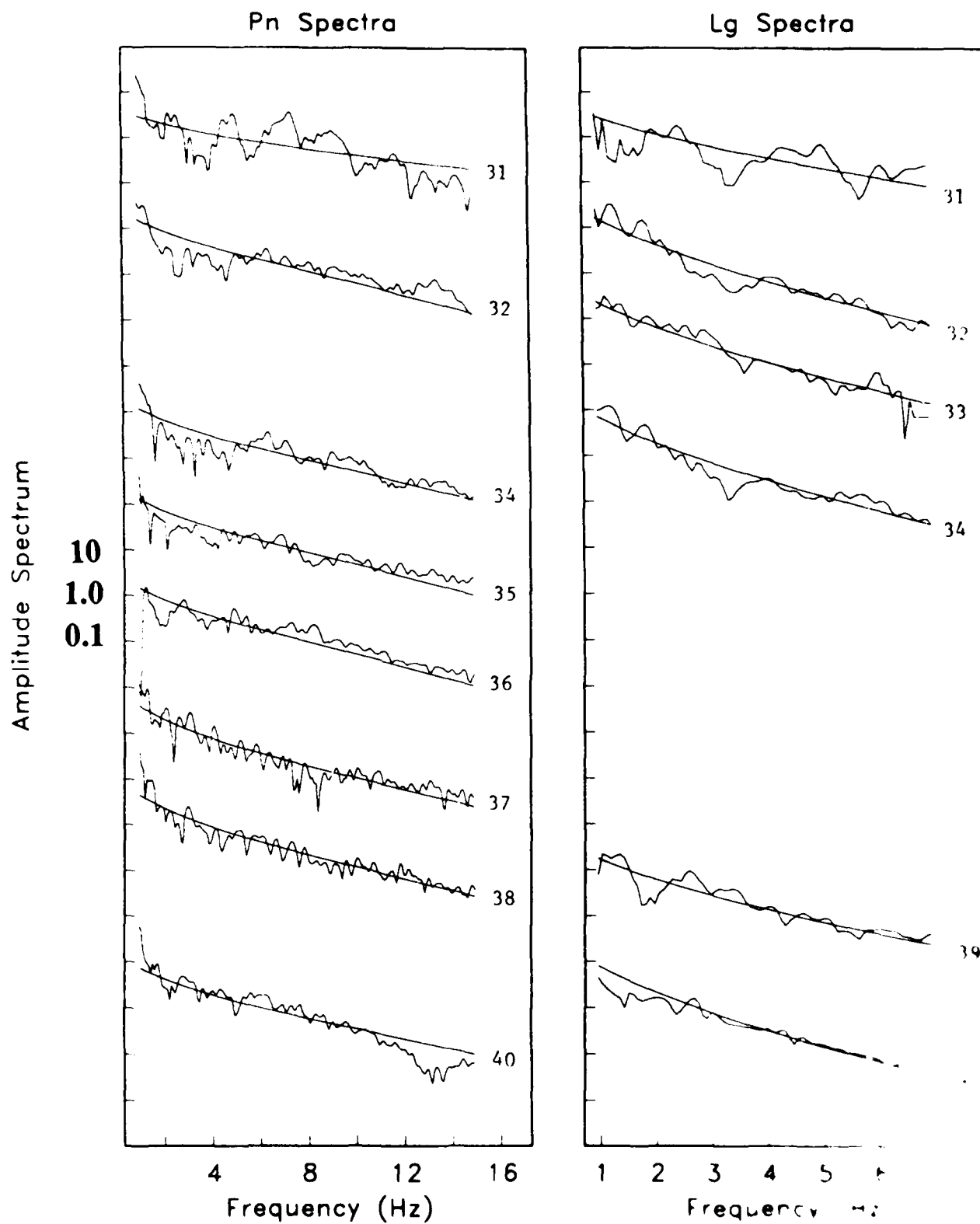


Figure B.1 (Continued).

AD-A187 399

REGIONAL WAVE ATTENUATION AND SEISMIC MOMENT FROM THE
INVERSION OF NORESS (U) SCIENCE APPLICATIONS
INTERNATIONAL CORP SAN DIEGO CA T J SERENO ET AL

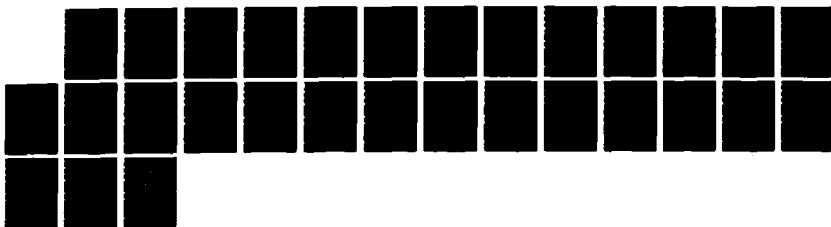
2/2

UNCLASSIFIED

31 JUL 87 SAIC-87/1736 AFGL-TR-87-0237

F/G 8/11

NL





MICROCOPY RESOLUTION TEST CHART
NATIONAL BUREAU OF STANDARDS-1963-A

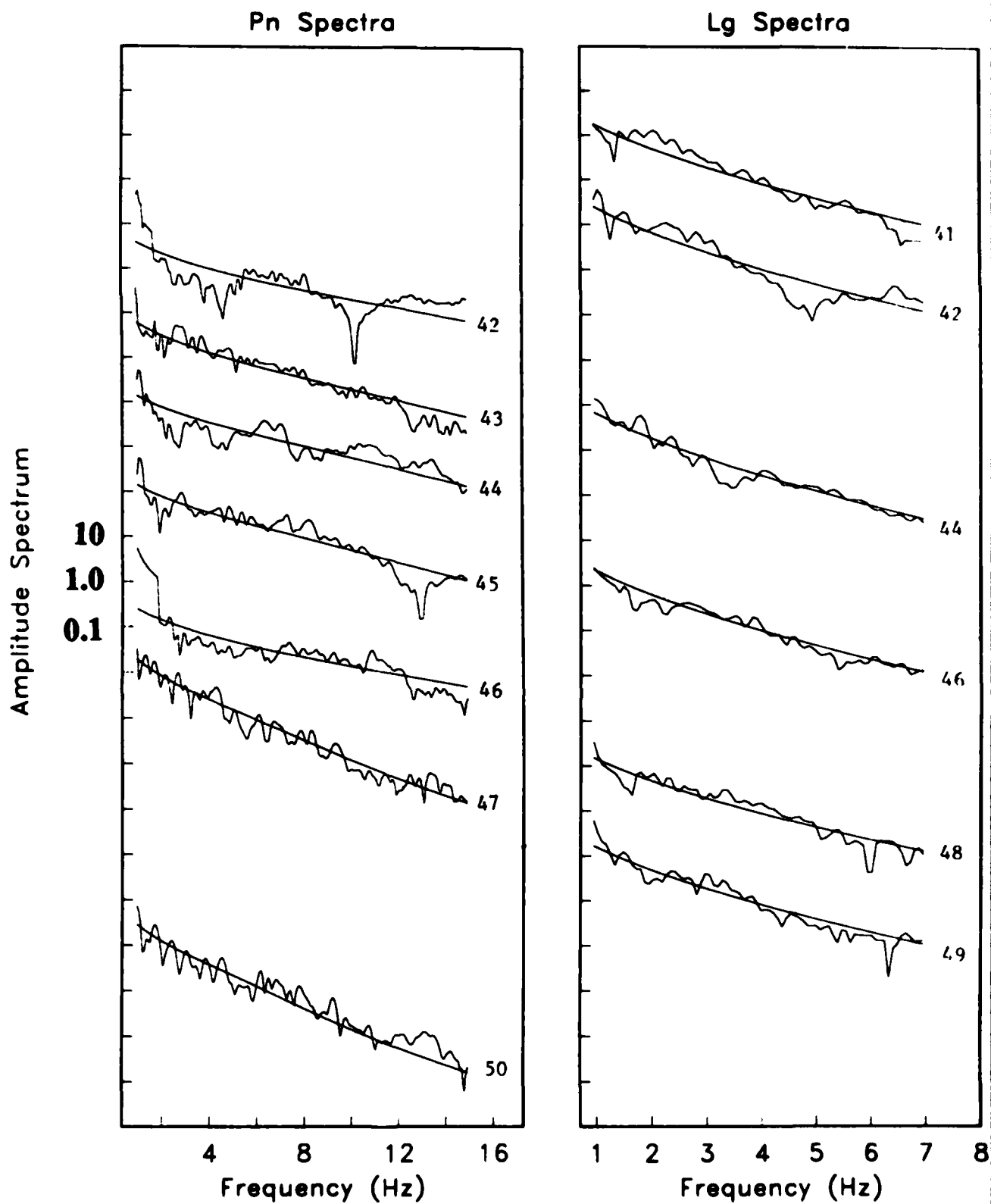


Figure B.1 (Continued).

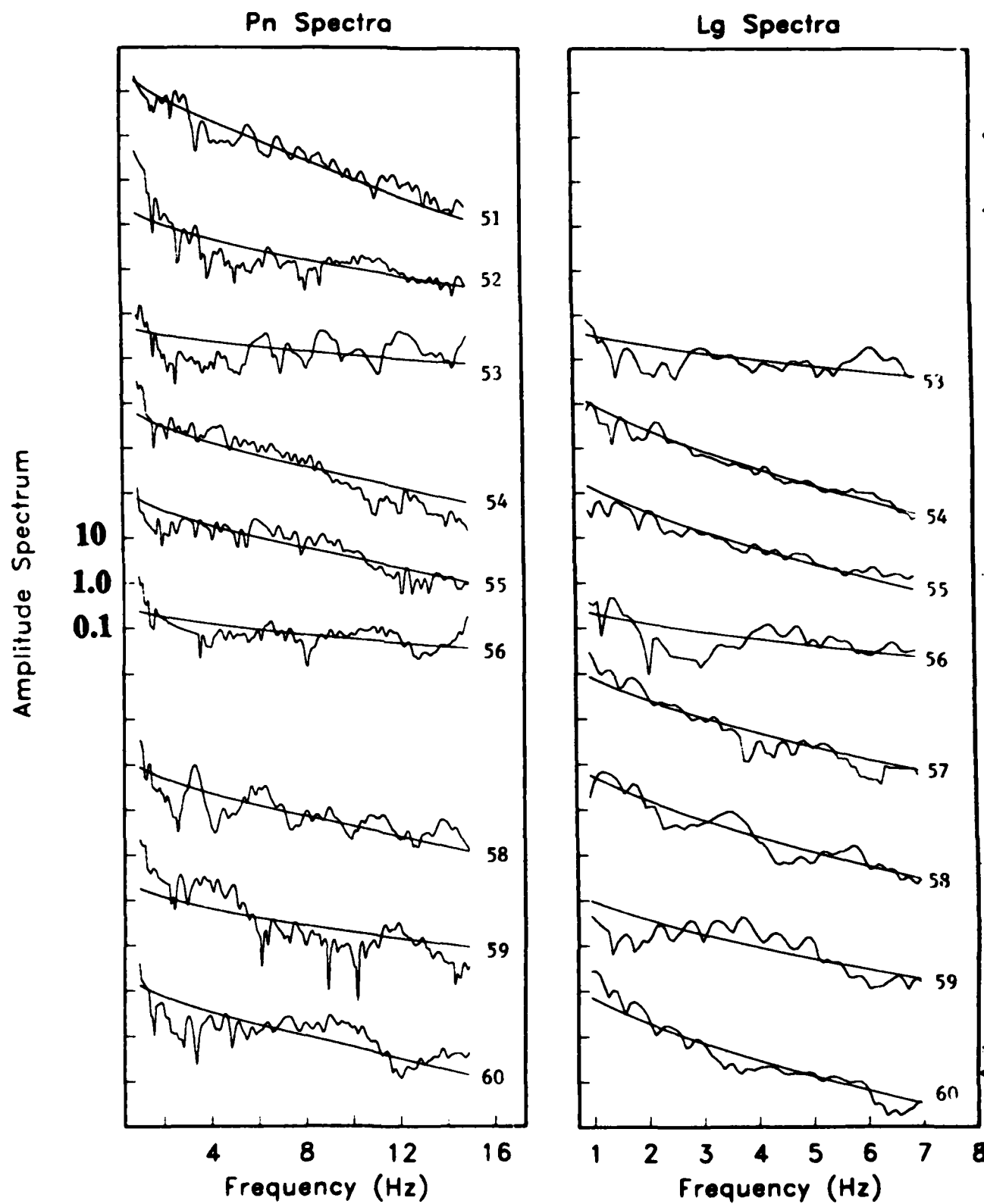


Figure B.1 (Continued).

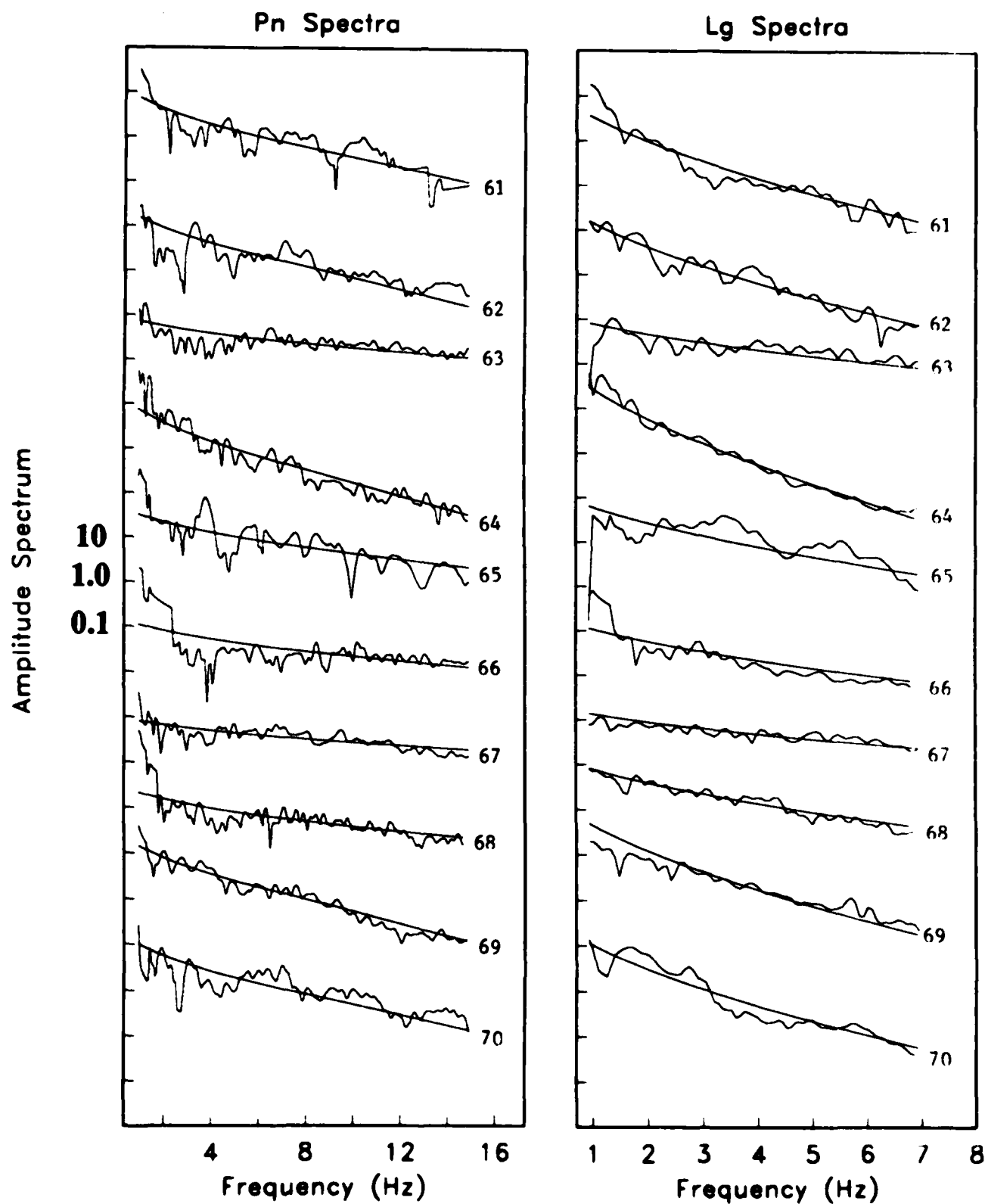


Figure B.1 (Continued).

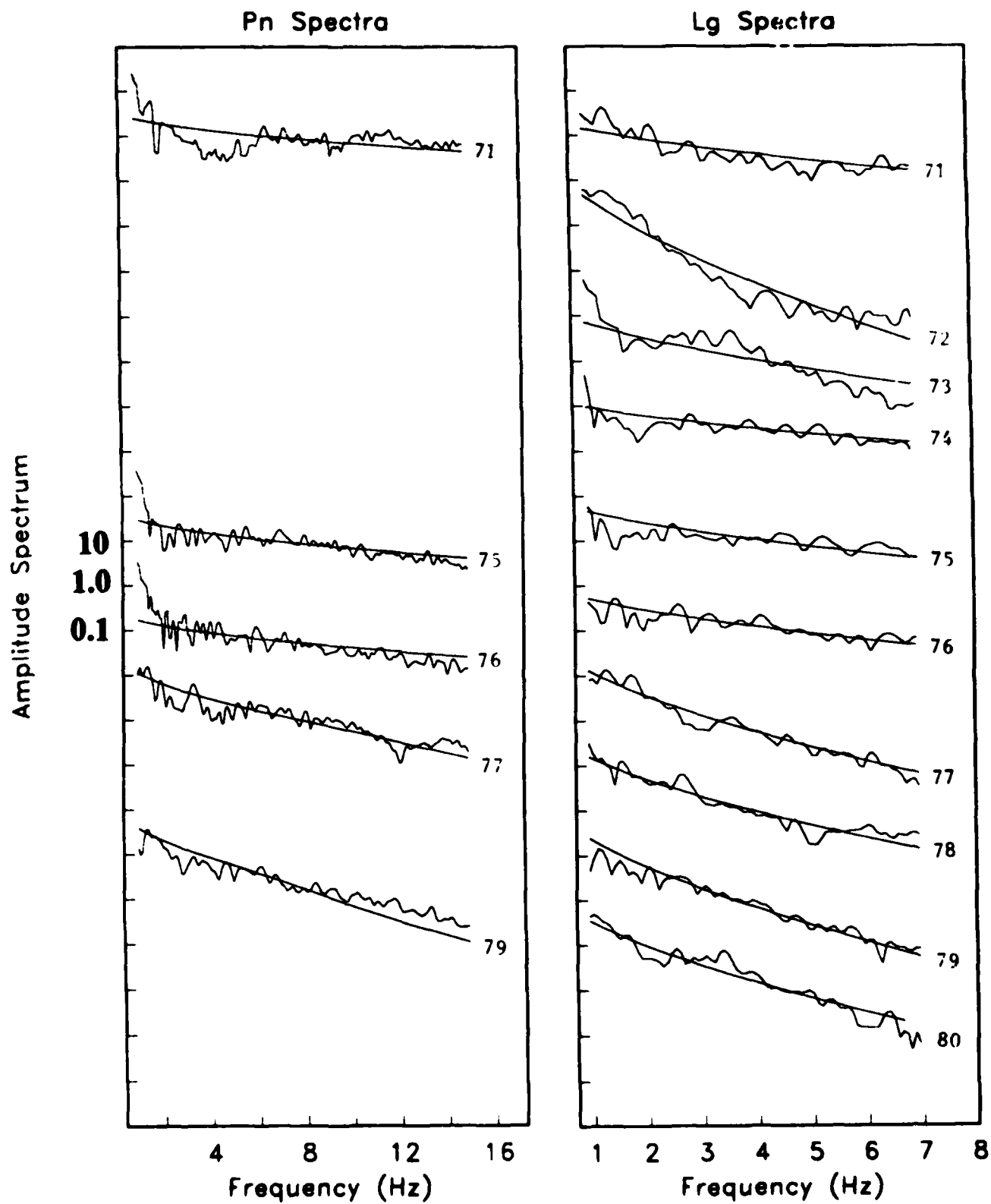


Figure B.1 (Continued).

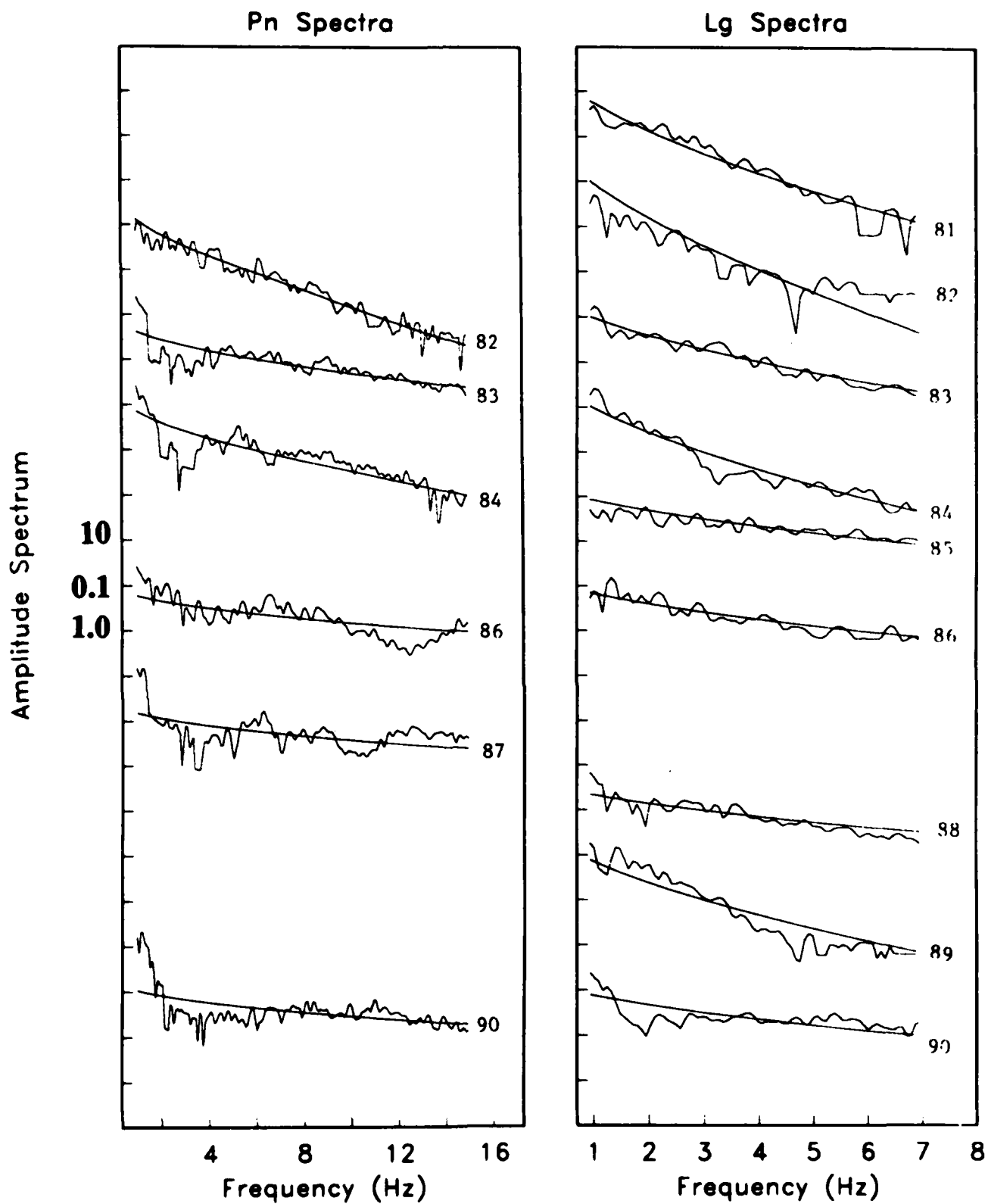


Figure B.1 (Continued).

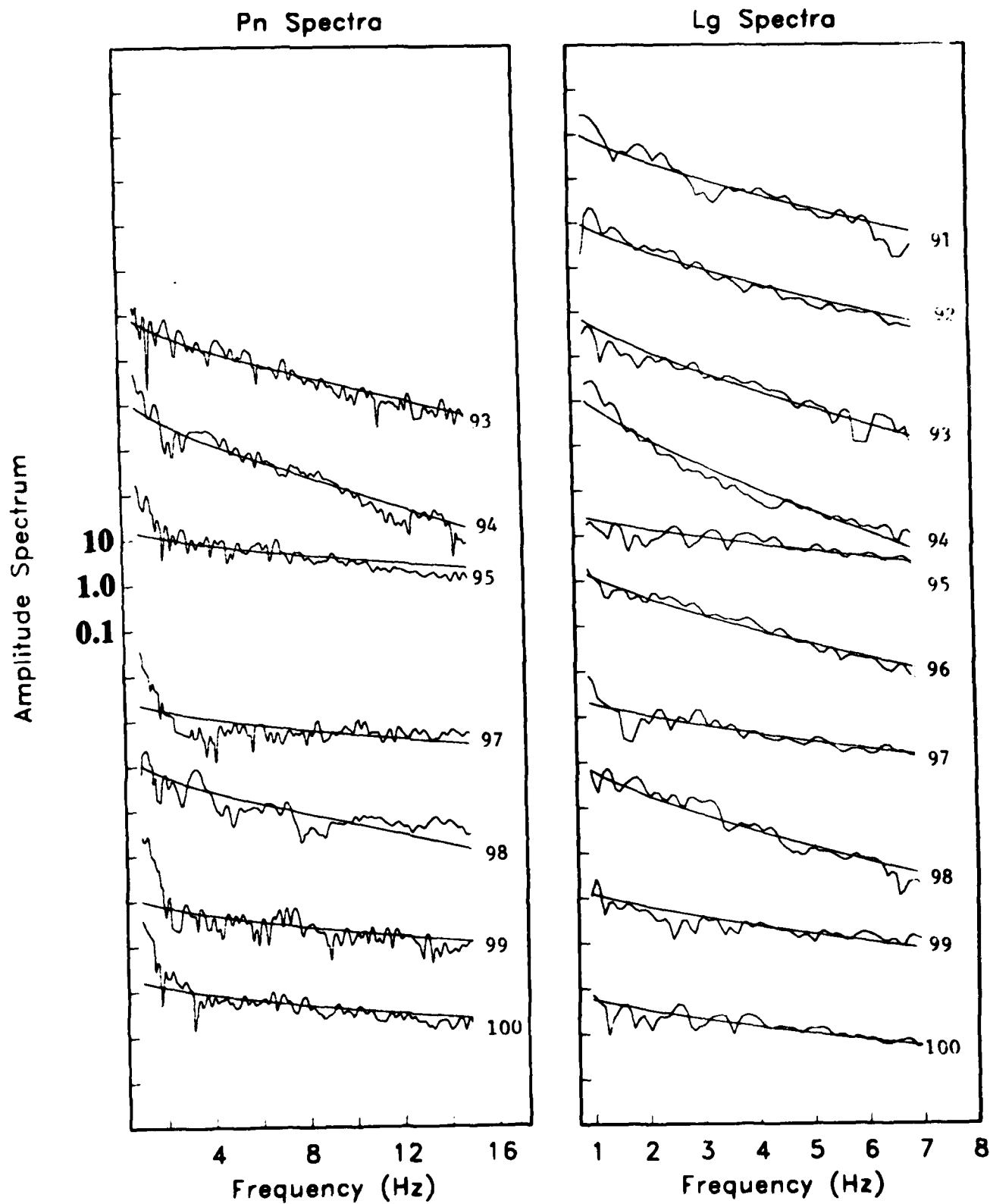


Figure B.1 (Continued).

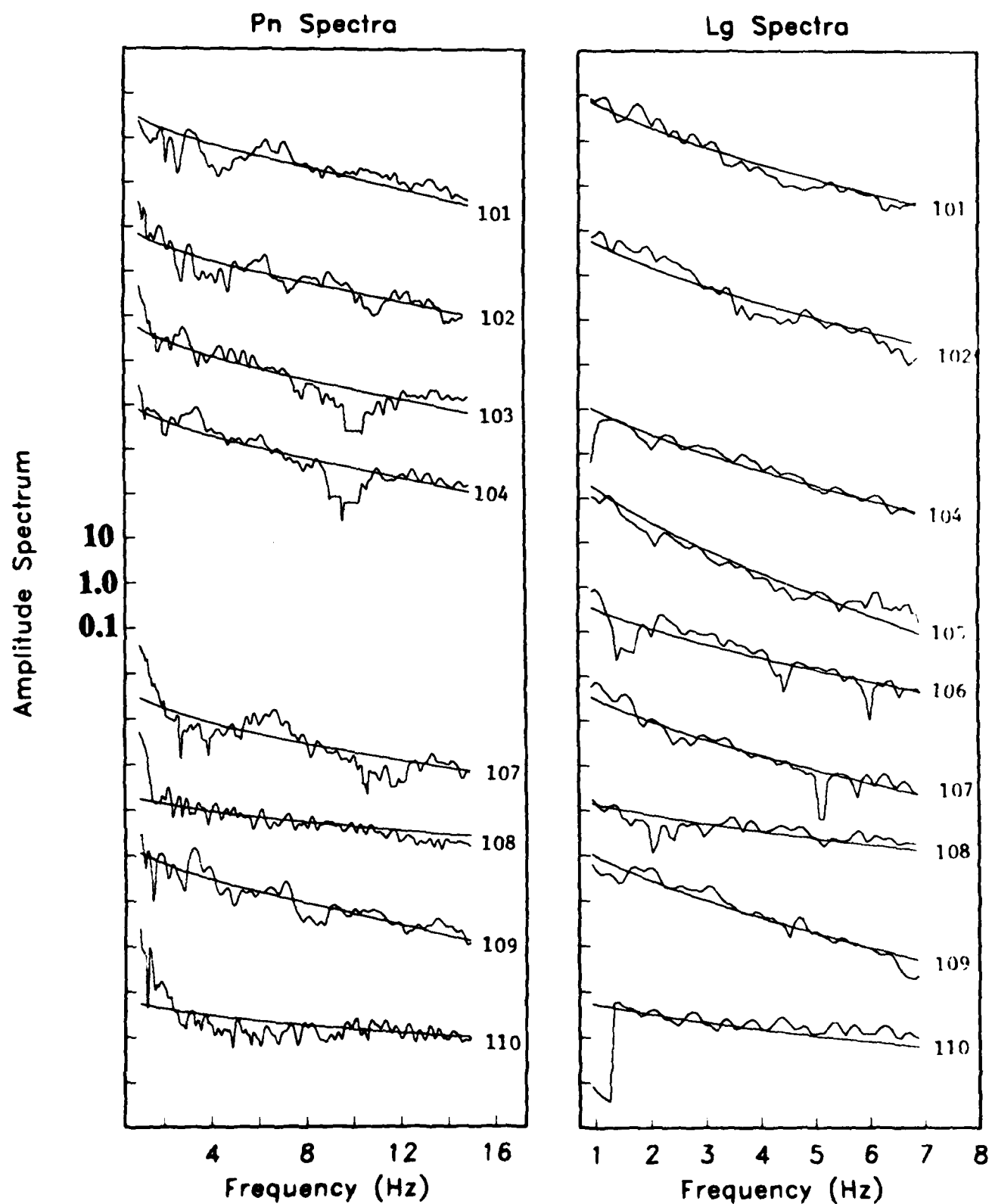


Figure B.1 (Continued).

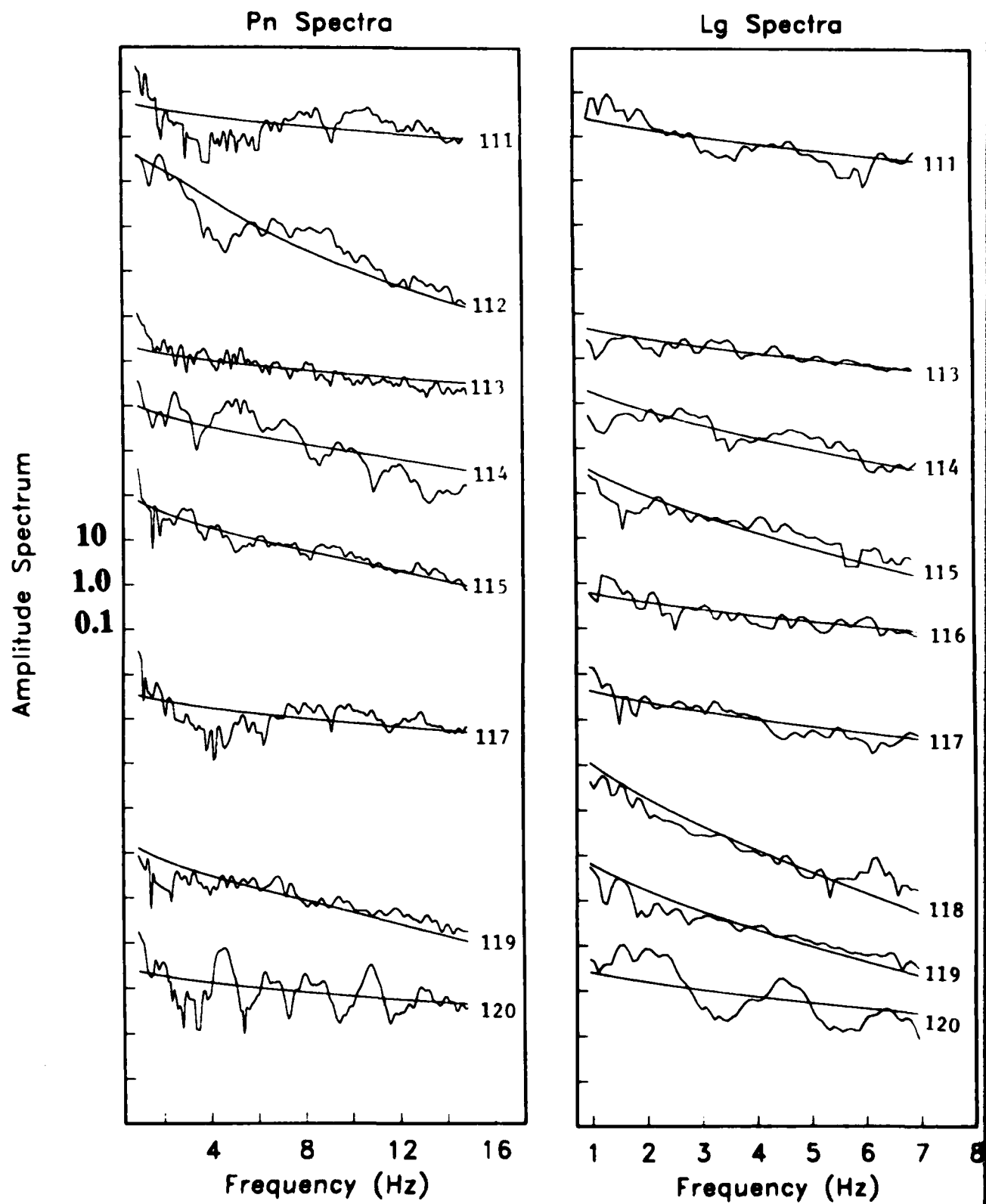


Figure B.1 (Continued).

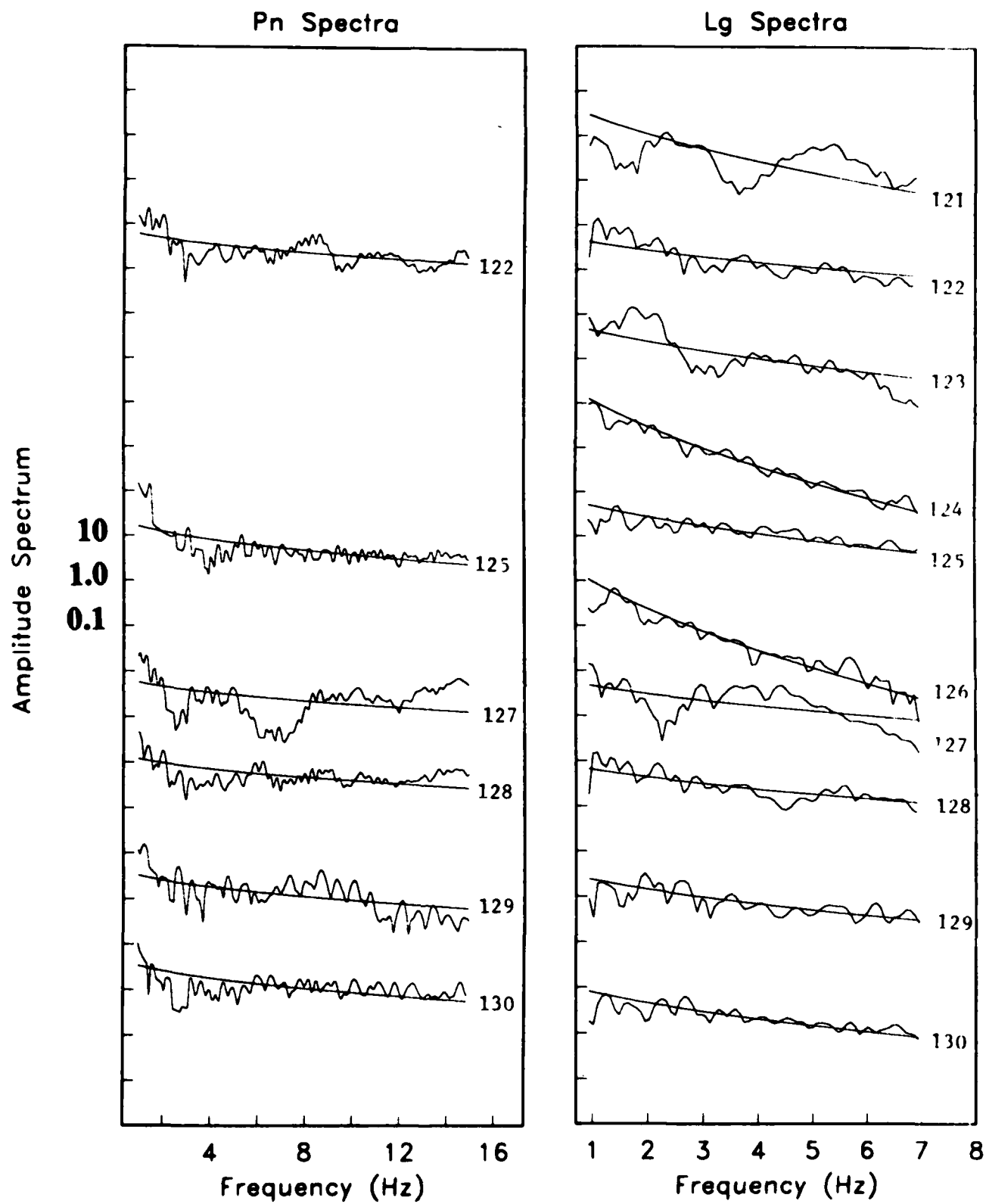


Figure B.1 (Continued).

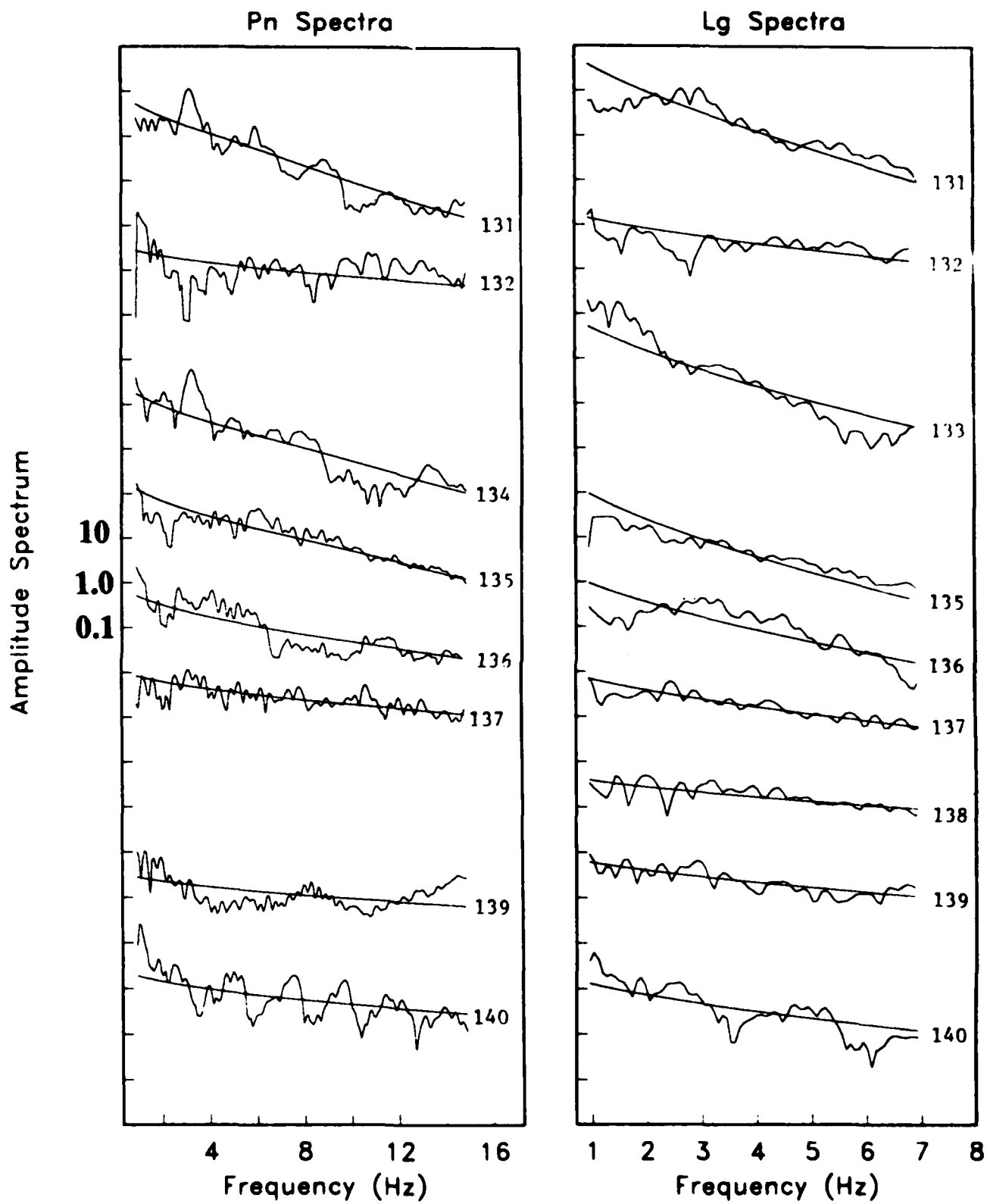


Figure B.1 (Continued).

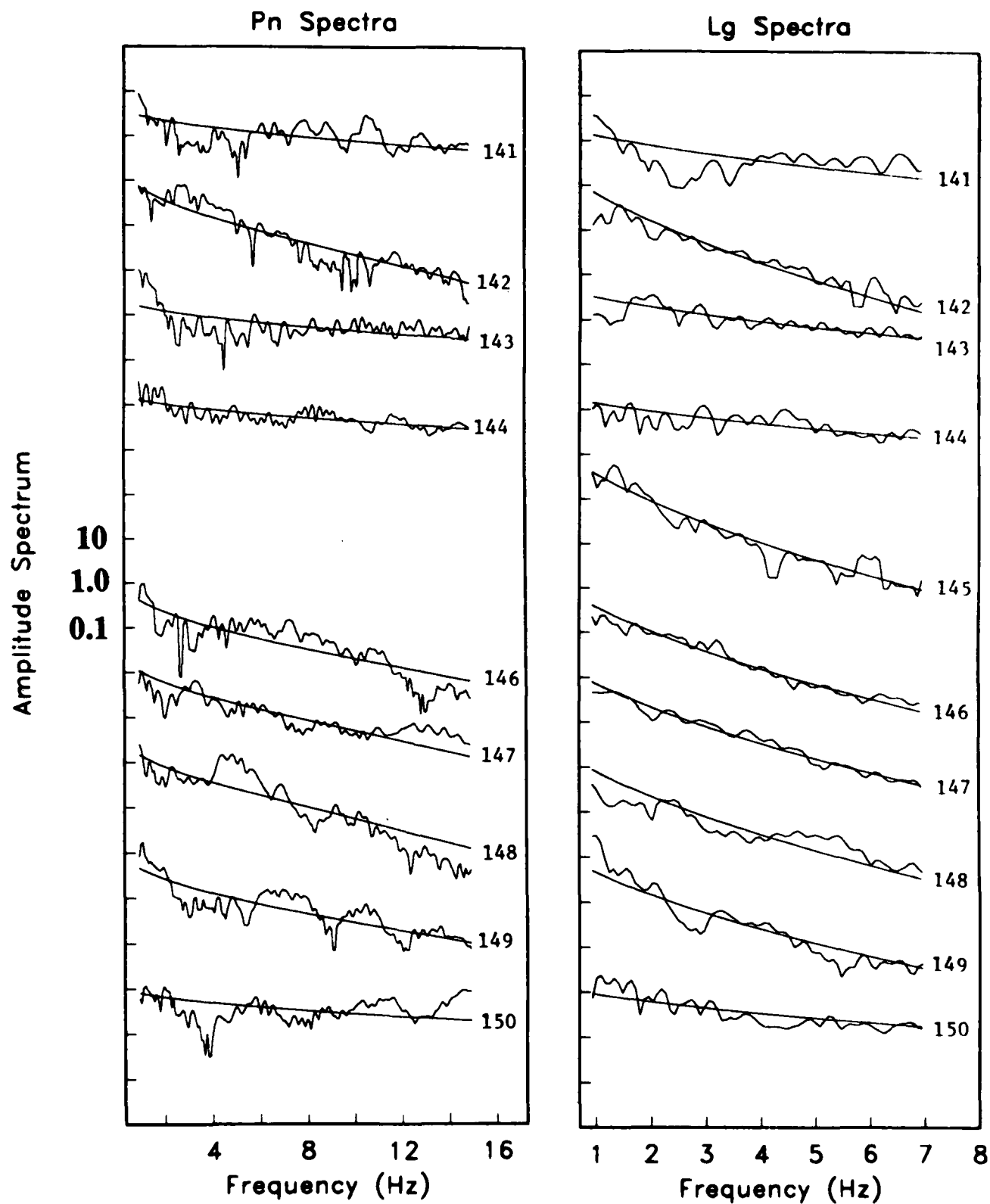


Figure B.1 (Continued).

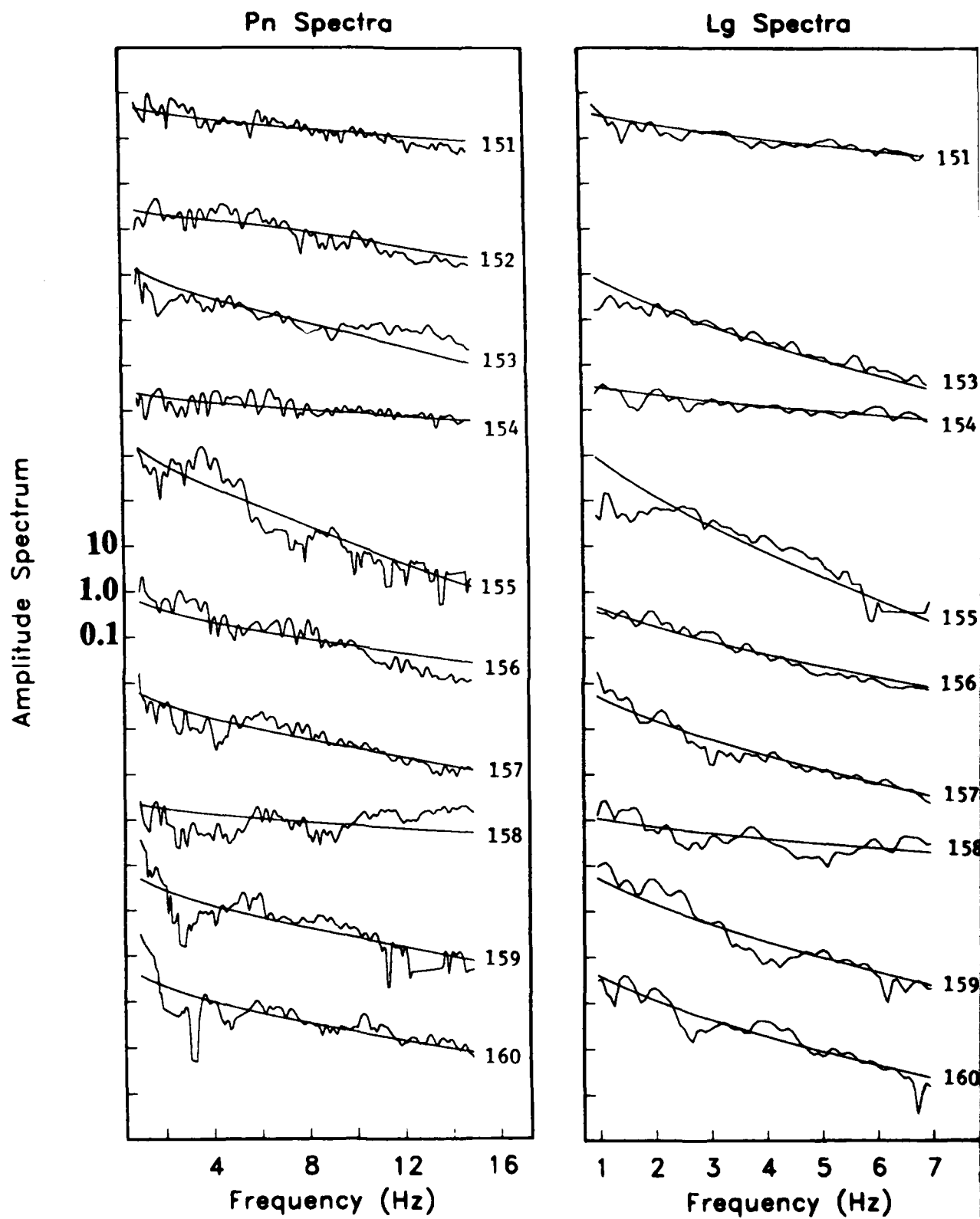


Figure B.1 (Continued).

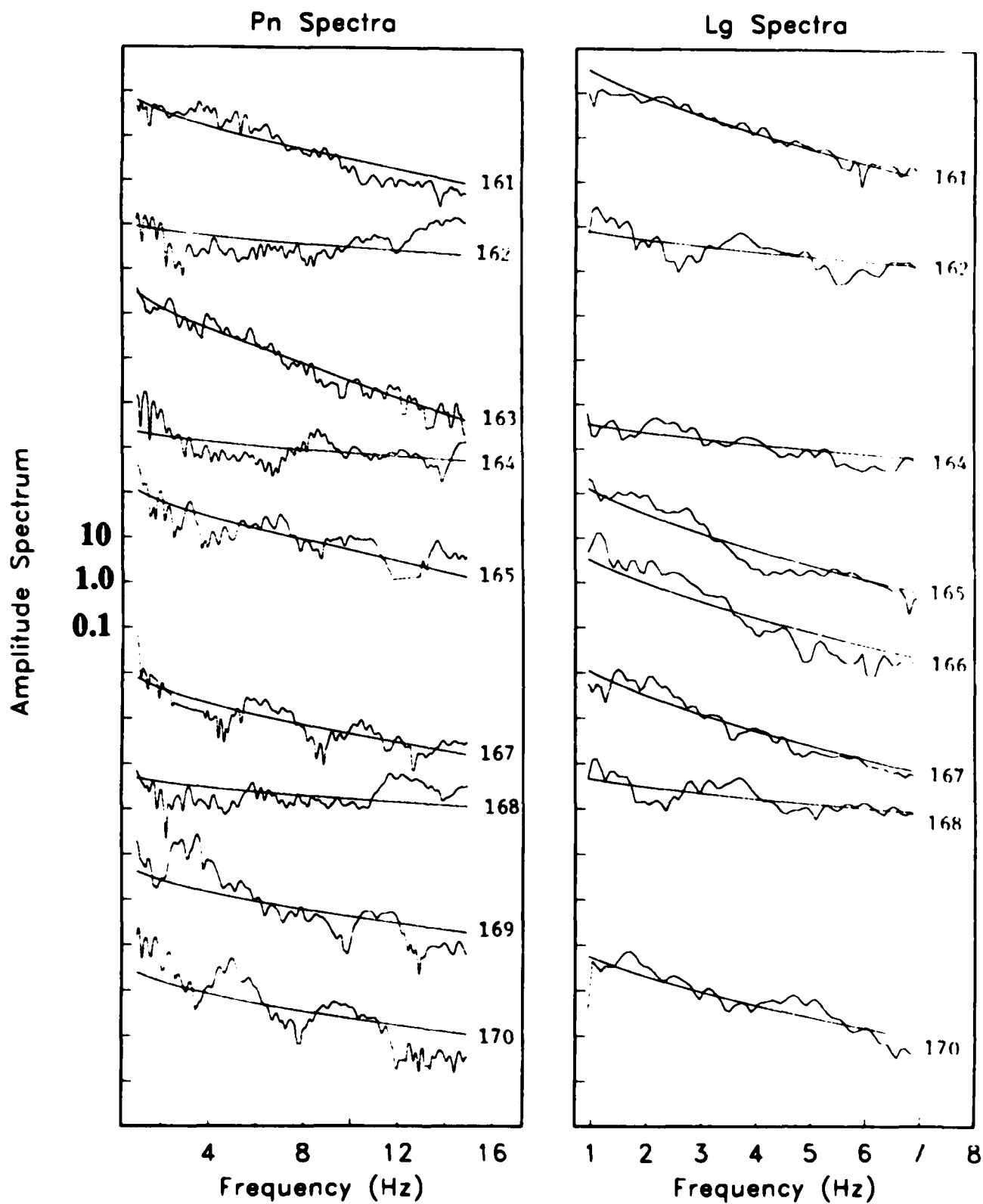


Figure B.1 (Continued).

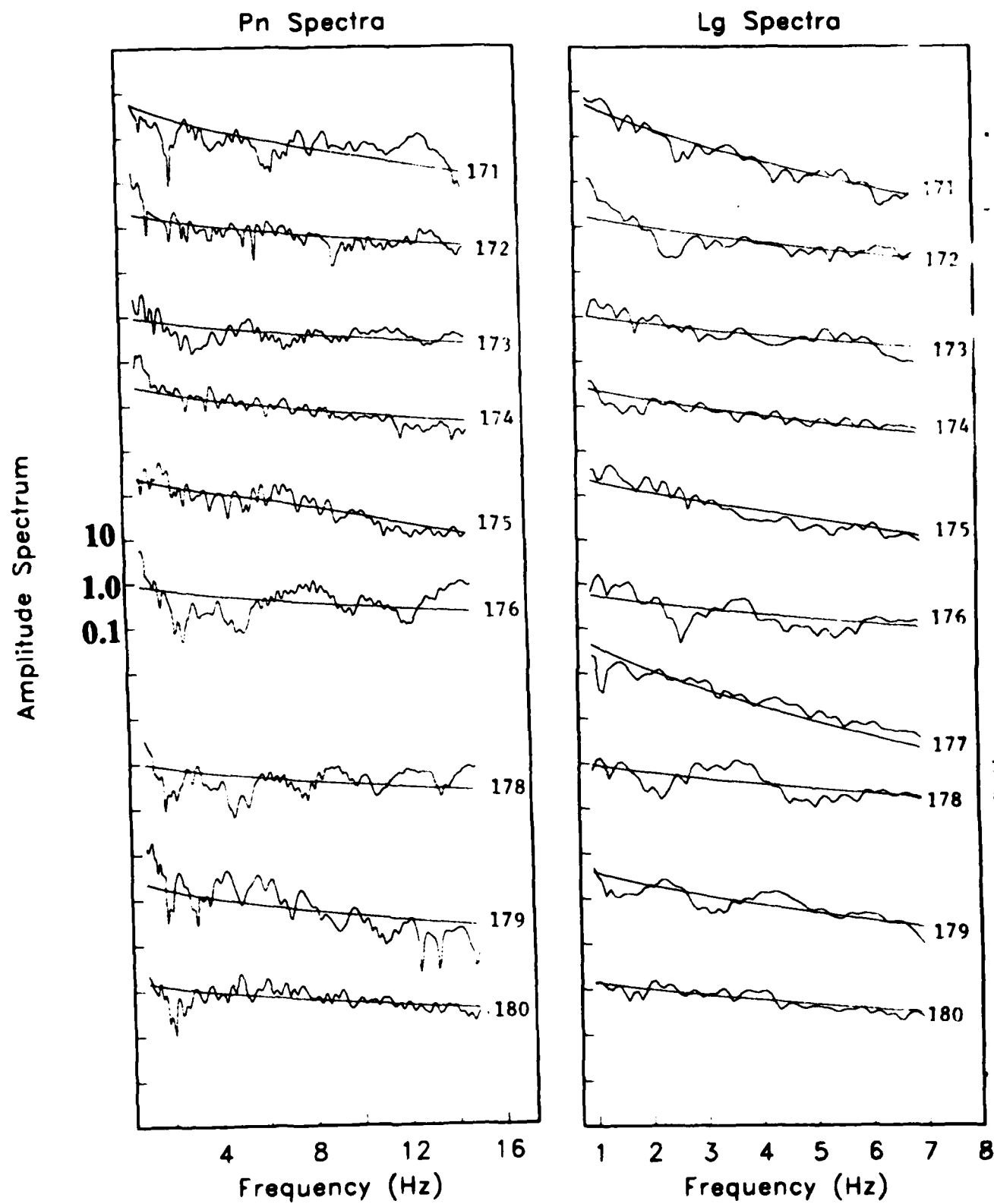


Figure B.1 (Continued).

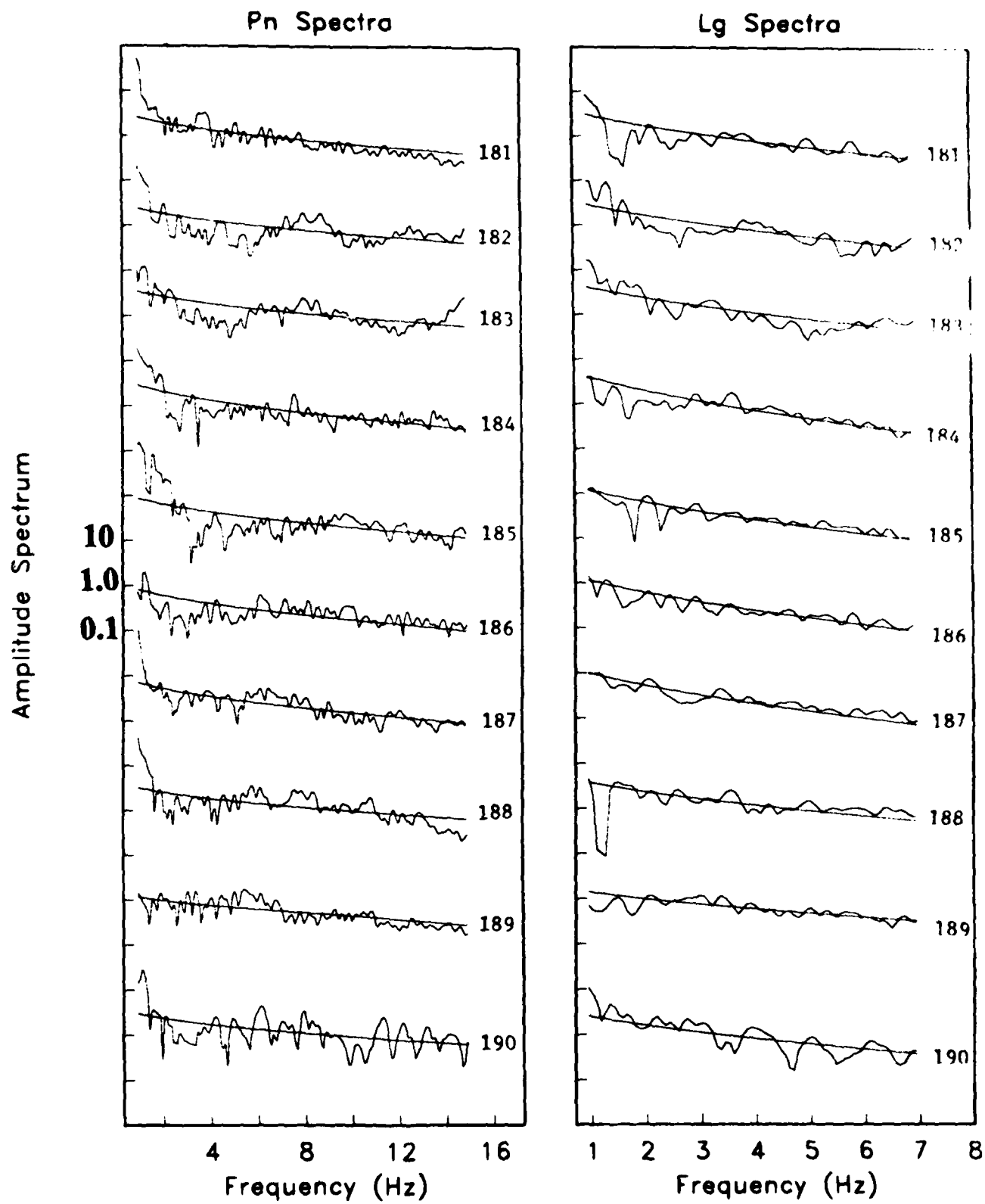


Figure B.1 (Continued).

DISTRIBUTION LIST

Dr. Monem Abdel-Gawad
Rockwell Internat'l Science Center
1049 Camino Dos Rios
Thousand Oaks, CA 91360

Professor Keiiti Aki
Center for Earth Sciences
University of Southern California
University Park
Los Angeles, CA 90089-0741

Dr. Ralph Alewine III
DARPA/STO/GSD
1400 Wilson Boulevard
Arlington, CA 22209-2308

Professor Shelton S. Alexander
Geosciences Department
403 Deike Building
The Pennsylvania State University
University Park, PA 16802

Professor Charles B. Archambeau
Cooperative Institute for Resch
in Environmental Sciences
University of Colorado
Boulder, CO 80309

Dr. Thomas C. Bache Jr.
Science Applications Int'l Corp.
10210 Campus Point Drive
San Diego, CA 92121

Dr. Robert Blandford
DARPA/STO/GSD
1400 Wilson Boulevard
Arlington, CA 22209-2308

Dr. Lawrence Braile
Department of Geosciences
Purdue University
West Lafayette, IN 47907

Dr. James Bulau
Rockwell Int'l Science Center
1049 Camino Dos Rios
P.O. Box 1085
Thousand Oaks, CA 91360

Dr. Douglas R. Baumgardt
Signal Analysis & Systems Div.
ENSQ, Inc.
5400 Port Royal Road
Springfield, VA 22151-2388

Dr. G. Blake
US Dept of Energy/DP 331
Forrestal Building
1000 Independence Ave.
Washington, D.C. 20585

Dr. S. Bratt
Science Applications Int'l Corp.
10210 Campus Point Drive
San Diego, CA 92121

Woodward-Clyde Consultants
ATTN: Dr. Lawrence J. Burdick
Dr. Jeff Barker
P.O. Box 93245
Pasadena, CA 91109-3245 (2 copies)

Dr. Roy Burger
1221 Serry Rd.
Schenectady, NY 12309

Professor Robert W. Clayton
Seismological Laboratory/Div. of
Geological & Planetary Sciences
California Institute of Technology
Pasadena, CA 91125

Dr. Vernon F. Ormier/Earth Resources
Lab, Dept of Earth, Atmospheric and
Planetary Sciences
MIT - 42 Carleton Street
Cambridge, MA 02142

Professor Anton W. Dainty
AFGL/LWH
Hanscom AFB, MA 01731

Dr. Zoltan A. Der
ENSQ, Inc.
5400 Port Royal Road
Springfield, VA 22151-2388

Professor Adam Dziewonski
Hoffman Laboratory
Harvard University
20 Oxford St.
Cambridge, MA 02138

Professor John Ebel
Dept of Geology & Geophysics
Boston College
Chestnut Hill, MA 02167

Dr. Jack Evernden
USGS-Earthquake Studies
345 Middlefield Road
Menlo Park, CA 94025

Professor John Ferguson
Center for Lithospheric Studies
The University of Texas at Dallas
P.O. Box 830688
Richardson, TX 75083-0688

Mr. Edward Giller
Pacific Seirra Research Corp.
1401 Wilson Boulevard
Arlington, VA 22209

Dr. Jeffrey W. Given
Sierra Geophysics
11255 Kirkland Way
Kirkland, WA 98033

Professor Steven Grand
Department of Geology
245 Natural History Building
1301 West Green Street
Urbana, IL 61801

Professor Roy Greenfield
Geosciences Department
403 Deike Building
The Pennsylvania State University
University Park, PA 16802

Dr. James Hannon
Lawrence Livermore Nat'l Lab.
P.O. Box 808
Livermore, CA 94550

Professor David G. Harkrider
Seismological Laboratory
Div of Geological & Planetary Sciences
California Institute of Technology
Pasadena, CA 91125

Professor Donald V. Helmberger
Seismological Laboratory
Div of Geological & Planetary Sciences
California Institute of Technology
Pasadena, CA 91125

Professor Eugene Herrin
Institute for the Study of Earth
& Man/Geophysical Laboratory
Southern Methodist University
Dallas, TX 75275

Professor Robert B. Herrmann
Department of Earth & Atmospheric
Sciences
Saint Louis University
Saint Louis, MO 63156

U.S. Arms Control & Disarm. Agency
ATTN: Mrs. M. Hoinkes
Div. of Multilateral Affairs
Room 5499
Washington, D.C. 20451

Professor Lane R. Johnson
Seismographic Station
University of California
Berkeley, CA 94720

Professor Thomas H. Jordan
Department of Earth, Atmospheric
and Planetary Sciences
Mass Institute of Technology
Cambridge, MA 02139

Dr. Alan Kafka
Department of Geology &
Geophysics
Boston College
Chestnut Hill, MA 02167

Ms. Ann Kerr
DARPA/STO/GSD
1400 Wilson Boulevard
Arlington, VA 22209-2308

Professor Charles A. Langston
Geosciences Department
403 Deike Building
The Pennsylvania State University
University Park, PA 16802

Professor Thorne Lay
Department of Geological Sciences
1006 C.C. Little Building
University of Michigan
Ann Harbor, MI 48109-1063

Dr. Arthur Lerner-Lam
Lamont-Doherty Geological Observatory
of Columbia University
Palisades, NY 10964

Dr. George R. Mellman
Sierra Geophysics
11255 Kirkland Way
Kirkland, WA 98033

Professor Brian J. Mitchell
Department of Earth & Atmospheric
Sciences
Saint Louis University
Saint Louis, MO 63156

Professor Thomas V. McEvilly
Seismographic Station
University of California
Berkeley, CA 94720

Dr. Keith L. McLaughlin
Teledyne Geotech
314 Montgomery Street
Alexandria, VA 22314

Mr. Jack Murphy - S-CUED
Reston Geophysics Office
11800 Sunrise Valley Drive
Suite 1212
Reston, VA 22091

Dr. Carl Newton
Los Alamos National Lab.
P.O. Box 1663
Mail Stop C335, Group E553
Los Alamos, NM 87545

Professor Otto W. Nuttli
Department of Earth &
Atmospheric Sciences
Saint Louis University
Saint Louis, MO 63156

Professor J. A. Orcutt
Geological Sciences Div.
Univ. of California at
San Diego
La Jolla, CA 92093

Dr. Frank F. Pilotte
Director of Geophysics
Headquarters Air Force Technical
Applications Center
Patrick AFB, Florida 32925-6001

Professor Keith Priestley
University of Nevada
Mackay School of Mines
Reno, Nevada 89557

Mr. Jack Raclin
USGS - Geology, Rm 3 C136
Mail Stop 928 National Center
Reston, VA 22092

Professor Paul G. Richards
Lamont-Doherty Geological
Observatory of Columbia Univ.
Palisades, NY 10964

Dr. Norton Rimer
S-CUBED
A Division of Maxwell Lab
P.O. 1620
La Jolla, CA 92038-1620

Dr. George H. Rothe
Chief, Research Division
Geophysics Directorate
HQ Air Force Technical
Applications Center
Patrick AFB, Florida 32925-6001

Professor Larry J. Ruff
Department of Geological Sciences
1006 C. C. Little Building
University of Michigan
Ann Arbor, MI 48109-1063

Dr. Alan S. Ryall, Jr.
Center of Seismic Studies
1300 North 17th Street
Suite 1450
Arlington, VA 22209-2308

Professor Charles G. Sammis
Center for Earth Sciences
University of Southern California
University Park
Los Angeles, CA 90089-0741

Dr. David G. Simpson
Lamont-Doherty Geological Observ.
of Columbia University
Palisades, NY 10964

Dr. Jeffrey L. Stevens
S-CUBED,
A Division of Maxwell Laboratory
P.O. Box 1620
La Jolla, CA 92038-1620

Professor Brian Stump
Institute for the Study of Earth & Man
Geophysical Laboratory
Southern Methodist University
Dallas, TX 75275

Professor Ta-liang Teng
Center for Earth Sciences
University of Southern California
University Park
Los Angeles, CA 90089-0741

Dr. R. B. Tittmann
Rockwell International Science Ctr
1049 Camino Dos Rios
P.O. Box 1085
Thousand Oaks, CA 91360

Professor M. Nafi Toksoz/Earth Resources
Lab - Dept of Earth, Atmospheric and
Planetary Sciences
MIT - 42 Carleton Street
Cambridge, MA 02142

Dr. Lawrence Turnbull
OSWR/NED
Central Intelligence Agency
CIA, Room 5G48
Washington, D.C. 20505

Professor Terry C. Wallace
Department of Geosciences
Building #11
University of Arizona
Tucson, AZ 85721

Professor John H. Woodhouse
Hoffman Laboratory
Harvard University
20 Oxford St.
Cambridge, MA 02138

DARPA/PM
1400 Wilson Boulevard
Arlington, VA 22209

Defense Technical
Information Center
Cameron Station
Alexandria, VA 22314
(12 copies)

Defense Intelligence Agency
Directorate for Scientific &
Technical Intelligence
Washington, D.C. 20301

Defense Nuclear Agency/SPSS
ATTN: Dr. Michael Shore
6801 Telegraph Road
Alexandria, VA 22310

AFOSR/NPG
ATTN: Director
Bldg 410, Room C22
Bolling AFB, Wash D.C. 20332

AFTAC/CA (STINFO)
Patrick AFB, FL 32925-6001

U.S. Geological Survey
ATTN: Dr. T. Hanks
Nat'l Earthquake Resch Center
345 Middlefield Road
Menlo Park, CA 94025

SRI International
333 Ravensworth Avenue
Menlo Park, CA 94025

Center for Seismic Studies
ATTN: Dr. C. Romney
1300 North 17th St., Suite 1450
Arlington, VA 22209 (3 copies)

Science Horizons, Inc.
ATTN: Dr. Bernard Minster
Dr. Theodore Cherry
710 Encinitas Blvd., Suite 101
Encinitas, CA 92024 (2 copies)

Dr. G. A. Bollinger
Department of Geological Sciences
Virginia Polytechnical Institute
21044 Derring Hall
Blacksburg, VA 24061

Dr. L. Sykes
Lamont Doherty Geological Observ.
Columbia University
Palisades, NY 10964

Dr. S. W. Smith
Geophysics Program
University of Washington
Seattle, WA 98195

Dr. L. Timothy Long
School of Geophysical Sciences
Georgia Institute of Technology
Atlanta, GA 30332

Dr. N. Biswas
Geophysical Institute
University of Alaska
Fairbanks, AK 99701

Dr. Freeman Gilbert - Institute of
Geophysics & Planetary Physics
Univ. of California at San Diego
P.O. Box 109
La Jolla, CA 92037

Dr. Pradeep Talwani
Department of Geological Sciences
University of South Carolina
Columbia, SC 29208

Dr. Donald Forsyth
Dept. of Geological Sciences
Brown University
Providence, RI 02912

Dr. Jack Oliver
Department of Geology
Cornell University
Ithaca, NY 14850

Dr. Muawia Barazangi
Geological Sciences
Cornell University
Ithaca, NY 14853

Rondout Associates
ATTN: Dr. George Sutton,
Dr. Jerry Carter, Dr. Paul Pomeroy
P.O. Box 224
Stone Ridge, NY 12484 (3 copies)

Dr. Bob Smith
Department of Geophysics
University of Utah
1400 East 2nd South
Salt Lake City, UT 84112

Dr. Anthony Gangi
Texas A&M University
Department of Geophysics
College Station, TX 77843

Dr. Gregory B. Young
ENSQ, Inc.
5400 Port Royal Road
Springfield, CA 22151

Weidlinger Associates
ATTN: Dr. Gregory Wojcik
620 Hansen Way, Suite 100
Palo Alto, CA 94304

Dr. Leon Knopoff
University of California
Institute of Geophysics
& Planetary Physics
Los Angeles, CA 90024

Dr. Kenneth H. Olsen
Los Alamos Scientific Lab.
Post Office Box 1663
Los Alamos, NM 87545

Professor Jon F. Claerbout
Professor Amos Nur
Dept. of Geophysics
Stanford University
Stanford, CA 94305 (2 copies)

Dr. Robert Burridge
Schlumberger-Doll Resch Cr.
Old Quarry Road
Ridgefield, CT 06877

Dr. Robert Phinney/Dr. F.A. Dahlen
Dept of Geological
Geophysical Sci. University
Princeton University
Princeton, NJ 08540 (2 copies)

New England Research, Inc.
ATTN: Dr. Randolph Martin III
P.O. Box 857
Norwich, VT 05055

Sandia National Laboratory
ATTN: Dr. H. B. Durham
Albuquerque, NM 87185

AFGL/XO
Hanscom AFB, MA 01731-5000

AFGL/LW
Hanscom AFB, MA 01731-5000

AFGL/SULL
Research Library
Hanscom AFB, MA 01731-5000 (2 copies)

Secretary of the Air Force (SAFRD)
Washington, DC 20330

Office of the Secretary Defense
DDR & E
Washington, DC 20330

HQ DNA
ATTN: Technical Library
Washington, DC 20305

Director, Technical Information
DARPA
1400 Wilson Blvd.
Arlington, VA 22209

Los Alamos Scientific Laboratory
ATTN: Report Library
Post Office Box 1663
Los Alamos, NM 87544

Dr. Thomas Weaver
Los Alamos Scientific Laboratory
Los Alamos, NM 97544

Dr. Gary McQuarrie
Mission Research Corp.
735 State Street
P.O. Drawer 719
Santa Barbara, CA 93102

Dr. Al Florence
SRI International
333 Ravenwood Avenue
Menlo Park, CA 94025-3493

Dr. W. H. K. Lee
USGS
Office of Earthquakes, Volcanoes,
& Engineering
Branch of Seismology
345 Middlefield Rd
Menlo Park, CA 94025

Dr. Peter Basham/Earth Physics Branch
Department of Energy and Mines
1 Observatory Crescent
Ottawa, Ontario
CANADA K1A 0Y3

Dr. Eduard Berg
Institute of Geophysics
University of Hawaii
Honolulu, HI 96822

Dr. Michel Bouchon - Universite
Scientifique et Medicale de Grenob
Lab de Geophysique - Interne et
Tectonophysique - I.R.I.G.M-B.P.
38402 St. Martin D'Herès
Cedex FRANCE

Dr. Hilmar Bungum/NTNF/NORSAR
P.O. Box 51
Norwegian Council of Science,
Industry and Research, NORSAR
N-2007 Kjeller, NORWAY

Dr. Kin-Yip Chun
Geophysics Division
Physics Department
University of Toronto
Ontario, CANADA M5S 1A7

Dr. Alan Douglas
Ministry of Defense
Blacknest, Brimpton,
Reading RG7-4RS
UNITED KINGDOM

Professor Peter Harjes
Institute for Geophysik
Rhur University/Bochum
P.O. Box 102148, 4630 Bochum 1
FEDERAL REPUBLIC OF GERMANY

Dr. E. Husebye
NTNF/NORSAR
P.O. Box 51
N-2007 Kjeller, NORWAY

Mr. Peter Marshall, Procurement
Executive, Ministry of Defense
Blacknest, Brimpton,
Reading RG7-4RS
UNITED KINGDOM

Dr. B. Massinon
Societe Radiomana
27, Rue Claude Bernard
75005, Paris, FRANCE

END

FEB.

1988

DTic